Ludwig Maximilians Universität München

Faculty of Physics

Master Thesis

Background Estimation and Sensitive Studies for the Search of Scalar Top Quarks with a Single Electron or Muon in the Final State

(Untergrund Abschätzung für die Suche nach skalaren Top Quarks mit einem Lepton im Endzustand)

Paola Arrubarrena Tame

Munich, December 15, 2017

Supervisor: Prof. Dr. Dorothee Schaile

Abstract

Supersymmetry (SUSY) is an extension of the standard model of particle physics which predicts a supersymmetric partner for each particle in the standard model. If R-parity is conserved, then the lightest supersummetric particle (LSP) is stable and a good dark matter candidate. In many models the LSP is favored to be the lightest neutralino ($\tilde{\chi}_1^0$), and the SUSY partner of the top quark, stop ($\tilde{t}_1$), is usually assumed to be light and in the reach of the LHC.

A search for stop pair production in a simplified model of the stop decay scenario, targeting two different phase space regions is presented. This scenario contains final states with exactly one isolated electron or muon, missing transverse energy (MET) and several jets. The analysis uses 36.1 fb^{-1} of proton-proton collision data at a center of mass energy of $\sqrt{s}$= 13 TeV, recorded with the ATLAS detector at the LHC in 2015 and 2016.

The first model targets the phase space where $m_{\tilde{t}_1} - m_{\tilde{\chi}_1^0} < m_t$ and both $\tilde{t}_1$ undergo a three-body decay to a bottom quark, a W boson and the LSP. The dominant background arises from top quark ($t\bar{t}$) pair production, which is difficult to model in the extreme kinematic phase space of SUSY events, characterized by large MET and large transverse mass of the reconstructed W boson (m_T) decaying leptonically. A strategy to determine the normalization of the leading background (as well for the sub-leading backgrounds e.g. $t\bar{t}$ semileptonic, single top, W+jets) in a data-driven way, using control regions, is described. By defining dedicated control regions also for the sub-leading backgrounds, the background uncertainty in the signal region is better constrained, compared to the case with one single control region for the leading background. This results in a gain in sensitivity in this phase space compared with the current status.

In a second part a more compressed scenario where $m_{\tilde{t}_1} - m_{\tilde{\chi}_1^0} < m_W$, and both $\tilde{t}_1$ decay via a four-body channel into a bottom quark, two different light fermions and the LSP, has been studied . Preliminary optimization searches to obtain a dedicated signal region in this phase space are performed.

Contents

Chapter 1

Introduction

With the discovery of the Higgs boson in 2012 [1][2] the successful history of finding experimental evidence for the fundamental building blocks of nature continued. It was the last undiscovered particle of the Standard Model (SM) of particle physics, a theory developed throughout the second half of the 20th century that has become one of the most successful theories to date. Apart from the particle content, also its predictions for the particle interactions were found to match with experimental results with an unprecedented precision at different experiments, by this building strong confidence in it.

However, despite of its success, the Standard Model is not a complete theory. There are several phenomena which it cannot explain and it leaves open questions like: Why is the Higgs mass stable, although it should suffer from enormous loop corrections? What is dark matter observed in astrophysics measurements? What is it made of? Why does the SM require an unnaturally precise fine-tunning of parameters? Why is gravity so weak compared to the other three fundamental forces? How can gravity be introduced in a more general quantum theory?

To answer these and some more questions a theory beyond the Standard Model is required. Supersymmetry (SUSY) is one of the main candidates for a unified theory beyond the SM which introduces a symmetry between fermions and bosons, so the number of elementary particles will be roughly doubled. Since supersymmetric particles have not been observed yet, supersymmetry must be broken and thus supersymmetric particles must be heavier than Standard Model particles. The search for SUSY is intensively performed at the European Organization for Nuclear Research (CERN) where the Large Hadron Collider (LHC) is located and collides protons with a center of mass energy of 13 TeV. In these high energetic reactions many other particles can be created, possibly also supersymmetric particles. If, however, the lightest supersymmetric particle is neutral and stable[1] it becomes a perfect candidate for dark matter. The top squark, the supersymmetric partner of the top quark, might nonetheless be sufficiently light to be within the grasp of the LHC motivated by the strong coupling of the top/stop to the Higgs field. As SUSY is a theory with many free parameters, there are plenty of different signatures that can be studied in the collisions.

This thesis is dedicated to the search of supersymmety through the top squark with one isolated lepton (electron or muon), jets and large missing transverse energy in the final state using $36.\text{fb}^{-1}$ of data taken with the ATLAS detector throughout 2015 and 2016 at a center of mass energy $\sqrt{s}=13$ TeV.

---

[1]As in R-parity conserving SUSY models.

This thesis does specifically focus on two different regions in the supersymmetric parameter space, which exhibit a small mass difference between the stop and the neutralino $\Delta m = m_{\tilde{t}_1} - m_{\tilde{\chi}_1^0}$. The first is the three-body region, where $\Delta m < m_{top}$ and the stop $\tilde{t}_1$ decays via a b quark, a W boson and a neutralino $\tilde{\chi}_1^0$. In this region, inclusive studies for the background estimation are performed and new expected exclusion limits obtained with the systematic estimation. The second region is the four-body region, where $\Delta m < m_W$ and the stop $\tilde{t}_1$ decays via b quark, two different fermions f and a neutralino $\tilde{\chi}_1^0$. In this region a preliminary sensitivity cut-based study to improve the sensitivity in the signal region is shown.

Chapter 2

Theory

In the following sections a brief overview of the theoretical framework used in particle physics is given. After a short introduction to the Standard Model (SM), the concepts and motivations of Supersymmetry (SUSY) are illustrated and finally the process under consideration for this analysis is presented.

2.1 Standard Model of Particle Physics

Since the discovery of the electron in 1897 by J. J. Thomson [3], elementary particle physics has made extraordinary progress in understanding the fundamental processes in our universe. The Standard Model (SM) of particle physics is arguably one of the most successful physics theories to date. It is a theoretical framework which describes the fundamental particles and their electromagnetic, weak and strong interactions with great precision. Nearly all experimental results in the field of particle physics obtained in laboratory experiments can be accurately described by the Standard Model. It has been developed throughout the second half of the 20th century. Its two most important achievements in its history, from a theoretical point of view, were the unification of the electromagnetic and the weak force and the successful inclusion of the strong force into the theory. As a consequence, it lead to its current formulation as described in more detail in [4].

2.1.1 Particle content

The SM particles include 12 particles with half-integer spin number[1] that follow the Dirac-Fermi statistics and therefore are called fermions. Also four particles with an integer spin number that follows the Bose-Einstein statistics and are called gauge bosons, and a Higgs boson with a spin 0.

Gauge Bosons

Gauge bosons mediate interactions of all particles so they can be considered as the force carriers which have a spin 1. They are shown in Table 2.1 composed by the gluon (g), the photon (γ), the W boson and the Z boson. The photons are massless and electrically neutral particles, which mediate the electromagnetic force. The W and Z bosons are massive[2] and mediate the weak nuclear force, they are carriers of the weak charge so they can self-interact. The W boson is electrically charged and exists in two variants, the positive

---

[1]Using the common convention in high energy physics $c = \hbar = 1$

[2]By this having a short lifetime.

spin	0	1			
particle (mediators)	H^0	γ	g	$W^\pm$	Z
mass [GeV]	125.09±0.24	0	0	80.38±0.01	91.18±18
electric charge	0	0	0	$\pm e$	0

Table 2.1:Bosonic content of the SM and gravity [9], photon, gluon and graviton mass are set to their theoretically expected value 0 eV.

(W^+) and the negative (W^-) charge. The Z boson is electrically neutral. The gluons mediate the strong nuclear interaction. They are color charged[3]. The color-charge can take three values: red, blue and green. They can interact with themselves as the weak bosons, as explained in more detail in [5] and in the next section describing the strong interaction.

Higgs Boson

Unlike the gauge bosons, the Higgs boson is a massive spinless particle which is the only elementary scalar particle discovered in nature. Its main characteristics are shown in table 2.1. The Higgs boson is essential to formulate a theory explaining the mass of the gauge bosons, known as the Higgs mechanism [27] (explained in section 2.1.2). The Higgs boson is the excited state[4] of the Higgs field from this mechanism.

Fermions

When the particles have a half integer spin they are named fermions. In simple terms they are the building blocks of the ordinary matter. They exist in two groups depending on whether they carry color charge or not, with three generations each, having the same properties but different masses.

- *leptons* do not take part in the strong interaction. They can be subdivided in two classes: charged leptons and neutral leptons. The electron (e), muon (μ) and tau (τ) have an electric charge of $-e$ [5], and interact via both electromagnetic and weak interactions whereas the neutrinos $(\nu_e, \nu_\mu, \nu_\tau)$ are electrically neutral and therefore only interact via the weak interaction. By this, the W boson is the mediator in the conversion from a charged lepton to its neutrino and vice versa. The electron, muon and tau are massisve particles. The muon and tau have the same properties as the electron except for their masses. The neutrinos are taken to be massles in the SM[6]. The leptons are listed in the top part of Table 2.2 with their properties.

- *quarks*, the six quarks up (u), down (d), charm (c), strange (s), top (t) and bottom (b) are all massive fermions. Up, charm and top quarks (named up-type quarks) carry electric charge of $\frac{2}{3}e$, while down, strange and bottom quarks (down-type quarks) carry electric charge of $\frac{1}{3}e$. Unlike leptons, quarks also carry an additional quantum number: the color charge [5]. Quarks participate in the electromagnetic, weak and strong interactions. An isolated quark has never been observed in nature because of color confinement. It is a phenomenon implying that color charged particles cannot be isolated. Naturally they can be found in bound systems called hadrons

---

[3]Gluons are a mixture of a color and an anti-color charge [5].

[4]In quantum mechanics, an excited state of a system is any quantum state of the system that has a higher energy than the ground state (i.e. more energy than the absolute minimum)[6].

[5]1.602×10^{-19}C [7].

[6]The observation of neutrino oscillations shows that the neutrinos should have a small mass[8].

	Generation	Particle	Mass[MeV]	Electric charge $[e]$
	1	e	0.511	-1
		ν_e	0	0
Leptons	2	μ	105.66	-1
		ν_μ	0	0
	3	τ	1776.86	-1
		ν_τ	0	0
	1	u	2.2	$+\frac{2}{3}$
		d	4.7	$-\frac{1}{3}$
Quarks	2	c	$1.28 \cdot 10^3$	$+\frac{2}{3}$
		s	96	$-\frac{1}{3}$
	3	t	$173.1 \cdot 10^3$	$+\frac{2}{3}$
		b	$4.18 \cdot 10^3$	$-\frac{1}{3}$

Table 2.2:Fermionic content of the SM [10][11], neutrino mases are set to 0 eV.

which are color-neutral, either as a meson which consists of a quark-antiquark system, or as a baryon which consists of three quarks. Anti-quarks have the same mass and spin as their corresponding quarks but have opposite electric and color charges. The process of the formation of this hadrons out of quarks and gluons is called hadronization, which can give rise to cones of hadrons and other particles named jets.

In Table 2.2 the fermion description is shown with their electric charge and masses.

2.1.2 Mathematical Description

For a proper description of the SM particles and interactions, we need a mathematical framework which combines quantum mechanics and relativistic effects named Quantum Field Theory [12][13].

Quantum Field Theory (QFT)

In this framework particles are not treated as a discrete mass point but as a continuous system represented by a field $\phi(\vec{x}, t)$. The main idea is taken from classical mechanics were a Lagrangian $L(q, \dot{q}, t)$ is describing a system in motion and dependent on the generalized coordinates q_i with their time derivatives (velocities) $\dot{q}_i$. Analogously for a field theory a Lagrangian with density $\mathcal{L}(\phi, \partial_\mu \phi)$ is taken which is a function of the fields ϕ_i, and its time derivatives with respect to the space-time coordinates $x^\mu = (t, x^1, x^2, x^3)$. By incorporating the fields ϕ with the action S we get:

$$S = \int L dt = \int \mathcal{L}(\phi, \partial_\mu \phi) d^4 x \tag{2.1}$$

By the principle of least interaction δS we obtain the Euler-Lagrange equations which describe the dynamics of a system, and if $\mathcal{L}$ has more than one field ϕ, the Euler-Lagrange equation acts separately on each field ϕ_i, leading to [12]:

$$\partial_\mu \left(\frac{\partial \mathcal{L}}{\partial(\partial_\mu \phi_i)} \right) - \frac{\partial \mathcal{L}}{\partial \phi_i} = 0 \tag{2.2}$$

Gauge Symmetries

The SM is based on three gauge symmetries which are internal symmetries of the Lagrangian and they give rise to the forces, mediators and gauge bosons. They underline elementary particle interactions.

- Electromagnetic and Weak Interactions
  In the SM, both electromagnetic and the weak interaction, though their separately appearance, they can represent a single interaction described by the electroweak theory (EW). With the special unitary symmetry group $SU(N)$, which comprises all unitary matrices $n \times n$ with determinant 1, a $SU(2)$ symmetry subgroup can be introduced and motivated by:

  1. Only modeling the weak interaction (leaving aside the electromagnetic) a charged lepton l could transform into its corresponding neutrino ν_l and vice versa through the weak interaction freely because they look like two states of a single particle. With the quarks would be the same: $u, c, t \rightarrow dʹ, sʹ, bʹ$[7].

  This introduces a quantum number named the *weak isospin* to characterize between the two states of a lepton (if is charged or a neutrino) and between quarks, expressed as a doublet for each state. Considering the three pauli matrices σ_i[8][9] a linearly independent choice for the generator transformations [16], the isospin can be represented as $I = \sigma_i/2$ [16]. Conventionally τ_i is used insted of σ_i in order to avoid confusions with the ordinary spin. This gives three non-conmuting operators I_1, I_2, I_3. The states are labeled in terms of the total isospin I and its third component I_3, and by this, we can have an isospin symmetry [14]. Each doublet has a weak total isospin of $I = 1/2$, and individually, the upper components of the doublet with $I_3 = +1/2$ and the down components with $I_3 = -1/2$. The weak isospin doublets are in the form:

  $$\begin{pmatrix} \nu_e \\ e^- \end{pmatrix}, \begin{pmatrix} \nu_\mu \\ \mu^- \end{pmatrix}, \begin{pmatrix} \nu_\tau \\ \tau^- \end{pmatrix}, \begin{pmatrix} u \\ dʹ \end{pmatrix}, \begin{pmatrix} s \\ cʹ \end{pmatrix}, \begin{pmatrix} t \\ bʹ \end{pmatrix}$$

  2. The $SU(2)$ group should remain gauge invariant under local rotations in the weak isospin space. The rotation happen as [15]:

  $$\phi \equiv \begin{pmatrix} \nu_l \\ l^- \end{pmatrix} \rightarrow \phiʹ = U\phi \quad \text{with} \quad U = exp\left\{ -\frac{i}{2}\vec{\alpha}\vec{\tau} \right\} \tag{2.3}$$

  Where U is a unitary transformation ($U^\dagger U = UU^\dagger = 1$) and as it is under $SU(2)$, $\vec{\tau}$ is a vector with the 3 Pauli matrices and τ_i only acts in the isospin part. $\vec{\alpha}$ describes a vector with the rotational angles of the 3 isospin axes. An isospin part will be introduced to the dirac spinor $\psi(x)$ [17] so that a rotation in the isospin space only will act in the isospin part. For each generator $\frac{1}{2}\tau_i$ a gauge field is needed

---

[7]The ʹ denotes the weak eigenstates in the Cabibbo-GIM scheme [14].

[8]Where $i=1,2,3$ and $\sigma_1 = \begin{pmatrix} 0 & 1 \\ 1 & 0 \end{pmatrix}, \sigma_2 = \begin{pmatrix} 0 & -i \\ i & 0 \end{pmatrix}, \sigma_3 = \begin{pmatrix} 1 & 0 \\ 0 & -1 \end{pmatrix}$

[9]The Pauli matrices are self-adjoint($\sigma_i^\dagger = \sigma_i$) and they describe observables in any $SU(2)$ system.

to compensate the transformation. A triplet of three bosons to mediate the weak interaction is introduced as:

$$\vec{W}_\mu = \begin{pmatrix} W_\mu^1 \\ W_\mu^2 \\ W_\mu^3 \end{pmatrix}$$

Where the charged bosons are defined as the superposition of the first two components $W_\mu^\pm = \frac{1}{\sqrt{2}}(W_\mu^1 + iW_\mu^2)$, and the neutral boson defined as the third component $W_\mu^3 = W_\mu^0$.

3. It was shown by the Wu experiment [18] and by polarization studies [19] that fermions produced in weak interactions are polarized[10]. Particles can be left handed[11] or right handed[12], nevertheless the weak force does not conserve parity, this means that fermions that participate in weak interactions are only left handed[13] in the limit when $m_f \to 0$.

To identify the gauge fields $W_\mu^\pm$ to the $W^\pm$ exchange bosons, $W_\mu^\pm$ can only interact with left-handed fermions. A concept named chirality is introduced to distinguish fermions which left and right-handed pieces are differently transformed under a gauge group. Chirality for a dirac fermion is defined thorugh the operator γ^5 [14] with eigenvalies ± 1. Any Dirac field can thus be projected into its left- or right-handed component by acting with the projection operators P_L and P_R [15]. For this the U operator defined in equation 2.1, needs to have a projection operator of left-handed particles P_L included, because U describes the rotations in the isospin space, leading to a $SU(2)_L$ [16] symmetry and the associated bosons are taken to be massless for now.

The introduction of a local $U(1)$ symmetry, where $U(N)$ is the unitary group of all $N \times N$ matrices satisfying $U^\dagger U = 1$, gives rise to a gauge boson interacting with particles. The gauge boson can be interpreted as the photon, as $U(1)$ has a single generator, this $U(1)$ symmetry is used to describe electromagnetic interactions known as quantum electrodynamics (QED).

The weak force and the electromagnetic force can be combined in the electroweak interaction. For the $U(1)$ group the charge operator needs to produce the same eigenvalues for the members of each left-handed fermion doublet. Such charge should be related to the electric charge Q and the third component of the isospin I_3 in the form called *hypercharge* (Y):

$$Q = I_3 + \tfrac{1}{2}Y$$

---

[10]Depending on their velocity and degree of polarization $\beta = v/c$ [20].

[11]When the particle spin points in opposite direction of their momentum vector.

[12]When the spin of the particle points in the same direction as the momentum vector.

[13]And right-handed antifermions.

[14]With the Dirac matrices $\gamma^5 = i\gamma^0\gamma^1\gamma^2\gamma^3 = \begin{pmatrix} 0 & I \\ I & 0 \end{pmatrix}$ with I the identity matrix.

[15]$P_L = \frac{1}{2}(1 - \gamma_5)$ and $P_R = \frac{1}{2}(1 + \gamma_5)$

[16]L for left-handed

This term introduces a weak hypercharge invariant under the isospin construction because: left-handed fermions are doublets of the weak interactions and therefore have weak isospin of 1/2. Right-handed fermions are singlets and do not participate in the weak interactions, so they have isospin of 0. As a consequence we have a unitary group denoted by $U(1)_Y$. The bosons coupling to this hypercharge are not simply the W_μ^0 and the photon. Instead QED gauge theory has to be redefined to give rise to a neutral boson B_μ which is not identical to the photon A_μ. When the $\vec{W}_\mu$ and the B_μ bosons combine to two different mass eigenstates, the photon A_μ and the Z boson Z_μ, defined by the mixing angle θ_W[17]:

$$A_\mu = B_\mu \cdot \cos\theta_W + W_\mu^3 \cdot \sin\theta_W \qquad (2.4)$$

$$Z_\mu = -B_\mu \cdot \sin\theta_W + W_\mu^3 \cdot \cos\theta_W \qquad (2.5)$$

The gauge boson triplet $\vec{W}_\mu$ couples with a coupling constant of g of the $SU(2)_L$. The neutral gauge field B_μ couples with a couple strength of $g\prime$ of the $U(1)_Y$ with different strength to left- and right- handed fermions proportional to the hypercharge Y, as described in more detail in [22].

By this the gauge group of electroweak interaction is defined as $SU(2)_L \otimes U(1)_Y$. The invariance under local $SU(2)_L \otimes U(1)_Y$ transformations leads to the existence of the $W^\pm, Z^0$ and γ[18].

- Strong Interaction
  The strong nuclear force acts between colored particles. It is described by Quantum Chromodynamics (QCD) [23][24]. Instead of a positive and a negative charge like in QED, the strong interaction couples to the color-charge which is only carried by quarks and gluons. The gluons, unlike the photons, carry one color and one anti-color each. This leads to a *color-octet*. There are eight gluon states that correspond to each combination of color and anti-color, and as they carry color charge, they can interact with each other. The corresponding gluon singlet[19] is not realized in nature because it would be a color-neutral particle freely propagating alowing for long-range strong interactions, which have been not observed [25]. Mathematically the strong interaction is equal to a $SU(3)$ gauge group with eight generators, due to the eight type of gluons. It is referred as a $SU(3)_C$ gauge group due to the color charge interaction.

This leads us to the description of the SM by a combination of the mentioned locally symmetry groups in the form:

$$SU(3)_C \otimes SU(2)_L \otimes U(1)_Y \qquad (2.6)$$

- Higgs Mechanism
  The photon and the gluon have been found to be massless. In contrast the $W^\pm$ and the Z^0 bosons, have masses about 80 GeV and 91 GeV [29] respectively. An explanation to this problem is the so called Higgs mechanism. It introduces a Higgs

---

[17]Also named the Weinberg angle.

[18]While the W boson only couples to left-handed fermions, the coupling of the photon is the same for any handness.

[19]$|r\bar{r}\rangle + |b\bar{b}\rangle + |g\bar{g}\rangle$

field as a complex scalar doublet as [27][28]:

$$\Phi(x) = \frac{1}{\sqrt{2}} \begin{pmatrix} \phi_1^+(x) + i\phi_2^+(x) \\ \phi_1^0(x) + i\phi_2^0(x) \end{pmatrix} \tag{2.7}$$

and is essential to formulate a theory involving massive gauge bosons. It is based on spontaneous symmetry breaking[20] by finding a potential which ground state obeys different symmetry than the system as:

$$V(\Phi) = -\mu^2 \Phi^\dagger \Phi + \frac{\lambda}{2}(\Phi^\dagger \Phi)^2 \tag{2.8}$$

Where λ and μ are two free parameters. This potential is Mexican-hat shaped therefore has a global[21] minimum at x different to 0, whereat at 0 is a local maximum. This shape of the potential results in a non vanishing vacuum expectation value of the scalar field:

$$\phi_0(x) = \frac{1}{\sqrt{2}}(\phi_1(x) + i\phi_2(x)) \tag{2.9}$$

where ϕ_0 denotes the ground state of the field. This gives two possibilities of fluctuations around the ground state: around the azimuthal angle and the radius as shown in Figure 2.1.
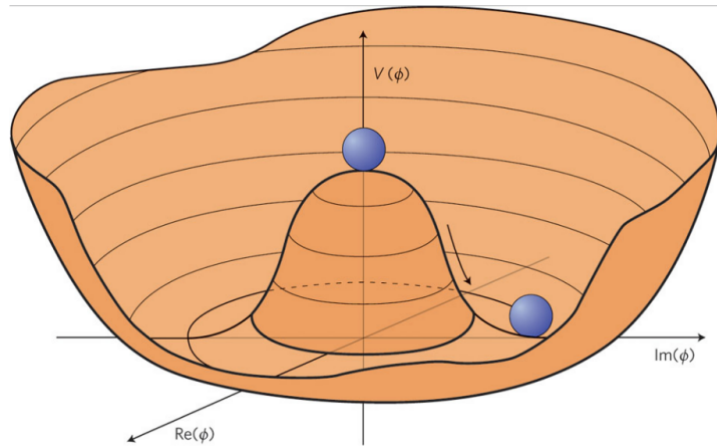
Figure 2.1 Illustration of the Mexican hat shaped Higgs potential $V(\Phi)$ with $\mu^2 < 0$. The blue spheres represent the state of the system at the point of spontaneous symmetry breaking in the ground state ϕ_0 [30].

Angular fluctuations do not need additional energy, but radial fluctuations do need additional energy. The full symmetry of the potential can be explored at high energies, while at low energies the symmetry of the potential is broken. The non-zero vacuum energy of the scalar field causes spontaneous symmetry breaking of the theory. Three of the four degrees of freedom introduced with the doublet are absorbed by the weak gauge fields, giving masses to the W and Z bosons. The remaining degree of freedom corresponds to the Higgs field for which the quanta are the Higgs bosons.

---

[20]Symmetry breaking is referred when a minimal energy state has less symmetry than the physical system itself [26].
[21]Only one.

2.1.3 Limitations of the SM

The SM is a very successful theory and provides with accurate precision the known phe-nomena in high energy physics. However it is still not complete and it leaves some open questions. Because of some of the SM limitations presented in this subsection, one of the most pressing issue in particle physics today is to find the correct extension of the SM.

Hierarchy and Fine-Tunning Problem

In the SM the particles gain their masses through the interaction with the Higgs field as described in the previous section. In 2012 a particle was found in that fullfill all the theoretical requirements of the Higgs boson [1][2].

At the energy scale used by the colliders experimets nowadays, gravity does not play an important role, nevertheless if we go to a reduced Planck scale $M_P = (8\pi G_{Newton})^{-1/2} = 2.4 \times 10^{18}$GeV [32] quantum gravitational effects become important and other forces are expected to become alike. The electromagnetic and weak forces become unified at the electroweak energy scale M_W defined by the vacuum expectation value of the Higgs field which is of the order of 10^2GeV and it differs from the M_P scale by 16 orders of magnitude in energy. The fact that he ratio M_P/M_W is so big is actually a good motivation to search for new physics beyond the SM. This big discrepancy between the two energies scales is the *hierarchy problem*.

Taking into account higher orders in Feynman diagrams, the parameters μ^2 and λ[22] from the higgs potential are corrected by loop diagrams from each particle that couples to the Higgs field. This corrections are proportional to the coupling λ_f^2 to a fermion f and therefore porportional to the mass of the fermion m_f^2 as shown in Figure 2.2(a). This leads to a correction to the squared Higgs mass m_H^2. To get a Higgs mass of about 125 GeV there must be a cancellation between such a huge correction and the bare Higgs squared mass. This cancellation requires incredible *fine-tuning* of the bare Higgs squared mass which violates the naturalness [31] principle. The mass of the Higgs boson should be modified by quantum corrections caused by virtual loop diagrams by [32]:

$$\Delta m_H^2 = -\frac{|\lambda_f|^2}{8\pi^2}\Lambda_{UV}^2 + ... \tag{2.10}$$

where λ_f is the coupling strength of the fermion to the Higgs boson and Λ_{UV}^2 is an ultraviolet momentum cutoff. It should be interpreted as the least energy scale were new physics phenomena could alter the high-energy behavior of the theory. For example, if Λ_{UV}^2 is taken to be in the order of M_P the Higgs squared mass parameter μ^2 is about 30 orders of magnitude in energy higher than the measured. That is why a scalar boson S can be introduced as shown in Figure 2.2 (b), as a solution to this problem because they also couples to the Higgs field. These new particles whose quantum corrections cancel out the loop integrals induced by the known SM particles. As fermionic loop diagrams add positive contributions and complex scalar particles lead to negative contributions, the fermionic loop diagrams could be cancelled out by scalar particles and vice versa. The correction will result as:

$$\Delta m_H^2 = \frac{\lambda_S}{16\pi^2}\Lambda_{UV}^2 + ... \tag{2.11}$$

---

[22]With a 125 GeV higgs mass, the parameters are taken to be $\mu = -(92.9 GeV)$ and $\lambda = 0.126$ [32].

By these two equations 2.8 and 2.9 we can appreciate that the quantum corrections would compensate each other if each of the quarks and leptons of the SM are accompanied with two complex scalars in the way $|\lambda_f|^2 = \lambda_S$, then the Λ_{UV}^2 contributions will be nicely canceled. This is an elegant solution independent on the cutoff scale giving us a stable Higgs mass, giving rise to a symmetry between bosons and fermions.
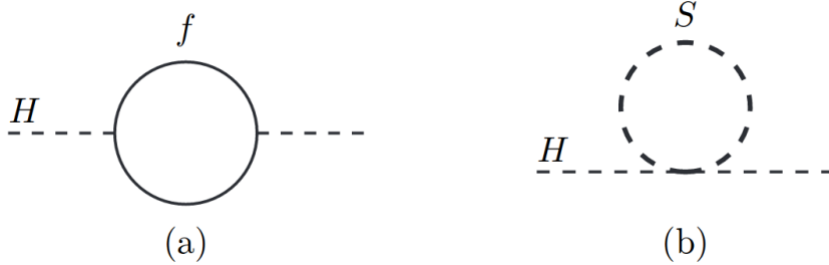
Figure 2.2. Loop corrections to the Higgs squared parameter m_H^2 due to a (a) fermion f and (b) a scalar boson S. [32]

Dark Matter

By astronomical observations and cosmological calculations scientist noticed that something is missing. Fritz Zwicky, a swiss physicist, in his studies in 1933 on the explorations of extragalactic nebulae [33][23], he found that the average density in the Coma system would have to be at least 400 times larger than what was derived from observations with luminous matter. Leading to the conclusion that dark matter should be present in greater amount than luminous matter and most of the cluster's mass is not visible. The clusters appear to be gravitationally bound, but all the luminous material inside them does not add up to the sufficient mass to retain the fast-moving galaxies. Throughout the years other observations [34] and calculations were carried out with the rotation of galaxies, were its tangential velocity seems to take a constant value after a certain distance from the galaxy's center, and the rotations do not follow the shape of the luminous contributions, indicating that there is more matter than expected [35].

Another proof of the existence of dark matter was given by gravitational lensing effects [34]. According to the general relativity theory the space is bended by gravity. By this principle if light emitted by a distant source would pass by a very massive object it should deviate from its straight path. Consequently the massive object will act like an optical lens and it will bend light proportional to the mass of this massive object. This effect was first observed in 1919 during the solar eclipse in front of Hyades star cluster, whose stars appeared to be displaced as they passed close the mass of the sun [36] giving experimental verification of general relativity. It was observed that the mass of the luminous visible matter of the massive object acting like a lens, cannot alone account for the lensing effects [37]. The observed lensing effect presented results required concentrations of unseen matter more massive than the expected from the plasma.

It seems that dark matter does not emit nor interact with electromagnetic radiation and also does not couple via strong interaction, so it cannot be explained as SM matter. It is pointed out that we have only observed approximately 5% of the total amount of

---

[23]Specifically in the dispersion of velocities in the Coma nebular cluster using the Doppler shift of their atomic spectra.

luminous matter in the universe [39], leaving us with an open question: What is dark matter made of? Why is there so much? There is no suitable candidate in the description of the SM for it, so a good extention of the SM proposing a weak interacting and massive particle (WIMP) is described in some BSM formulations [40].

Unification of Forces

The coupling constants of the known forces are very different, one naively would not think that unifying them is possible. However the couplings are not a fixed value but dependent on the energy scale. The unified description of the electromagnetic and the weak forces arose the question if any theory of unified forces possible. If we extrapolate the coupling constants of the electromagnetic, weak and strong interaction at high energies and high scales as shown in Figure 2.3 left, one could check if the unification is possible. In the SM description we can see that the coupling constants run into each other but do not reach the same value at the same energy. While it is necessary in the SM description to unify the electromagnetic and the weak forces, it is not possible to unify the electroweak ad the strong force, for example, without the idea of new physics playing a role beyond the electroweak scale [12]. As an empirical case and running the coupling constants at high energies were new physics would happen, we could have new particles at this point. In Figure 2.3 right new particles at a TeV scale have been introduced making the unification of the three forces possible, as a consequence the need of new physics model.
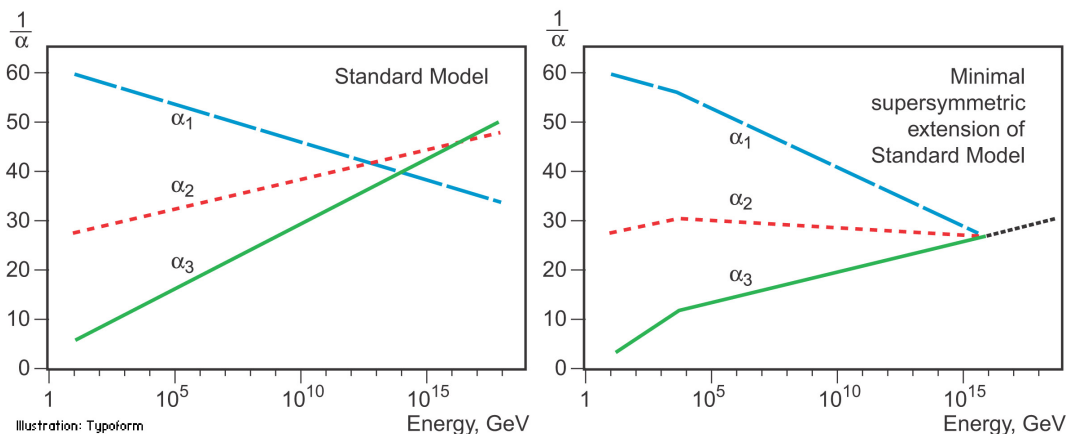
Figure 2.3 Running of the coupling constants $(\frac{1}{\alpha})$ (left) electromagnetic (α_1), weak (α_2) and strong (α_3) interactions as the gauge couplings in the SM. On the right the illustration of running the coupling constants in a minimal supersymmetric extension of the SM chosen to meet at some point near the Planck scale assuming that these new particles are not heavier than about 1 TeV [41].

2.2 Supersymmetry (SUSY)

A solution to the problems in the SM presented before is required. Implementing a symmetry between fermions and bosons as a solution will be described in the following part, which is best known as Supersymmetry (SUSY).

The particle content of the SM is roughly doubled because each known SM particle is then associated to a supersymmetrical one which defers by 1/2 in their spin but is equal in all the other quantum numbers. Fermionic superpartners are comonly denoted by the same name of the SM only adding a *s* in the front (i.e., the electron superpartner

is the *selectron*) and with the letters only adding a tilde (i.e., e becomes $\tilde{e}$). On the contrary the bosonic superpartners have the suffix -ino to the name (i.e., W bosons becomes *wino*). Simply speaking, a supersymmetric transformation turns a bosonic state into a fermionic state and vice versa. In terms of operators, the operator Q that generates such transformation must be an anti-commuting spinor as [32]:

$$Q|\text{Boson}\rangle = |\text{Fermion}\rangle, \qquad Q|\text{Fermion}\rangle = |\text{Boson}\rangle$$

Spinors are complex objects so the hermitian conjugate of the operator Q is $Q^\dagger$ and also a symmetry generator in the Weyl representation[24]. Q and $Q^\dagger$ are fermionic operators so they carry spin angular momentum of $1/2$. As the SM has chiral fermions, a parity violating interaction is possible, implying this, the generators Q and $Q^\dagger$ must follow the commutation and anti-commutation relations:

$$\{Q, Q^\dagger\} = P^\mu \tag{2.12}$$

$$\{Q, Q\} = \{Q^\dagger, Q^\dagger\} = 0 \tag{2.13}$$

$$[P^\mu, Q] = [P^\mu, Q^\dagger] = 0 \tag{2.14}$$

As SUSY generators are spinors, they naturally anticommute rather than commute [42]. P^μ is the four momentum generator in the space-time translations. Equation 2.12 introduces a connection between SUSY and the space-time[25] translations, and equation 2.14 points that supersymmetric transformations are independent of the space-time positions. All quantum numbers, with the exception of the spin, should match their SM partners. Schematically as shown in equation 2.14, P^μ commutes with the generators of SUSY and the squared invariant mass operator $P^2 = P^\mu P_\mu$. Meaning that particle states of a supersymmetric irreducible representation (multiplets denoted *supermultiplets*), containing both boson and fermion states, should have equivalent eigenvalues of P^2, and therefore equal masses [32].

From observations we can deduce that this is not the case and SUSY is not realized with equal masses, otherwise some sparticles would have been easily detected (like the *selectron*). Up to the submission of this thesis, no supersymmetric particle has been found. This can lead to the conclusion that supersymmetry must be a broken symmetry. The way this happens is by introducing soft breaking terms into the supersymmetry Lagrangian [44]. By this soft breaking, the superpartners should acquire more mass than the SM particles but the masses of the supersymmetric particles should not be much larger. For this reason there is still a good motivation to discover supersymmetry at the Large Hadron Collider (LHC) at CERN [32].

Particle Content of the Minimal Supersymmetric Standard Model (MSSM)

The minimal supersymmetris standard model (MSSM) represents a supersymmetric extension of the SM with a minimal addition of particles [51]. Table 2.3 lists for every SM particle, the name, spin and notation for its assigned super-partner. A representation of

---

[24]Weyl spinors describe particles with $1/2$ of spin and a given chirality. Each left and right handed spinors has two components. The component with left (right) chirality is denoted by $\psi_\alpha = \psi_L$ ($\bar{\psi}^\alpha = \psi_R$). The matrices $\epsilon_{\alpha\beta} = i\sigma_2$ and $\epsilon^{\alpha\beta} = -i\sigma_2$ are used to rise and lower the spinoral indices α and β. σ_2 denotes the Pauli matrix [43].

[25]Noether's Theorem relates conservation laws to dynamical symmetries. An invariance of physics laws under continuous symmetry transformations is associated with a conservation law. In space-time symmetries: translation in time conserves energy and translation in space conserves momentum.

Particle		SPartner		Spin
quarks	q	**squarks**	$\tilde{q}$	**0**
top	t	stop	$\tilde{t}$	
...	...			
leptons	l	**sleptons**	$\tilde{l}$	**0**
electron	e	selectron	$\tilde{e}$	
muon	μ	smuon	$\tilde{\mu}$	
tau	τ	stuau	$\tilde{\tau}$	
neutrino	ν_l	sneutrino	$\tilde{\nu}_l$	
gauge bosons		**gauginos**		**1/2**
photon	γ	photino	$\tilde{\gamma}$	
boson	Z	Zino	$\tilde{Z}$	
boson	W	Wino	$\tilde{W}$	
gluon	g	gluino	$\tilde{g}$	
Higgs boson	$H_i^{\pm,0}$	higgsino	$\tilde{H}_i^{\pm,0}$	**1/2**

Table 2.3: Particle content of the MSSM [43].

the SUSY algebra is given by the construction of *supermultiplet* states. They are defined as an irreducible representation combining fermion and boson states with the same quantum number except the spin. A particle and a superpartner are put together to form a supermultiplet. A supermultiplet has the same number of fermionic and bosonic degrees of freedom $n_F = n_B$ and by this we can construct two different supermultiplets:

- The first one is the most fundamental one and it is called *chiral* supermultiplet. It contains a Weyl fermion of spin 1/2 and its superpartner (a sfermion) represented by a complex scalar field of spin 0, this Weyl fermion has two helicity states $n_F = 2$ while the complex scalar field has its real and imaginary part, containing two scalar fields described in a single complex scalar field (the sfermion) [43] each yield $n_B=1$.

- The second representation is the gauge (or vector) supermultiplet. They consists of gluons and their fermionic superpartner the *gluino*. The field is obtained by a massless gauge boson with spin 1 together with a spin 1/2 fermionic superpartner called *gaugino* [53]. Both have two possible helicity states therefore $n_F = n_B = 2$.

The particles in the supermultiplets are massless at least until the gauge symmetry is spontaneously broken.

Recalling the SM fermions, which have different interactions depending if they are left- (L) or right- (R) handed [53]. In SUSY the left- and right- handed should belong to different supermultiplets and have distinct spartners. The $\tilde{f}_R$ and $\tilde{f}_L$ are different, even though the concept of handedness does not have any meaning for a scalar particle with helicity $\lambda = 0$, the L and R indices only refer to the fermion helicity and not to the one of its superpartner.

In the particle content of the MSSM the quarks and leptons are put together. In the

SM the Higgs field h is used to give mass to quarks of the down type via Yukawa[26] couplings $q\bar{d}h$ and taking the complex conjugate to give mass to the up type quarks via $q\bar{u}h^*$. Taking into account the scalar Higgs field, it has to be included in a chiral supermultiplet due to its spin 0 value. To let all the particles, except the Higgs bosons, the possibility to gain mass, avoid gauge anomalies and supply the necesary Yukawa couplings, at least two chiral Higgs doublets are required [32]:

$$H_u = \begin{pmatrix} H_u^+ \\ H_u^0 \end{pmatrix}, \qquad H_d = \begin{pmatrix} H_d^0 \\ H_d^- \end{pmatrix}$$

with weak hypercharge $Y = +1/2$ and $-1/2$ respectively. So, how does the superpartners of the SM gauge eigenstates mix to form the mass eigenstates of the MSSM [32]?

- In the doublets just shown, H_u can only couple to an up type quark and the H_d to all down type quark. This complex Higgs doublets have in total 8 degrees of freedom, the mechanism uses 3 degrees of freedom to give masses to the two W bosons ($\pm$) and to the Z boson. This leaves us with 5 degrees of freedom which [45][46]:

  - h^0, H^0: one light and one heavy neutral Higgs, even under CP[27] transformations.

  - A^0: neutral CP-odd Higgs

  - H^+, H^-: Two charged Higgs

- The higgsinos and electroweak gauginos mix with each other due to the electroweak symmetry breaking. The neutral higgsinos ($\tilde{H}_u^0$ and $\tilde{H}_d^0$) and the neutral gauginos ($\tilde{B}, \tilde{W}^0$) combine to form four masses eigenstates called *neutralinos* $\tilde{\chi}_i^0$ with $i \in \{1, 2, 3, 4\}$. The charged higgsinos ($\tilde{H}_u^+$ and $\tilde{H}_d^-$) and winos ($\tilde{W}^+$ and $\tilde{W}^-$) mix to form two mass eigenstates with charge ± 1 called *charginos* $\tilde{\chi}_j^\pm$ with $j \in \{1, 2\}$ to differentiate between them according to their masses from lighter to heavier [32].

- In the SM the electroweak gauge symmetry $SU(2)_L \times U(1)_Y$ is associated with spin-1 bosons ($W^{\pm,0}$ and B^0), and with spin-1/2 to superpartners *winos* and *binos* ($\tilde{W}^{\pm,0}$ and $\tilde{B}^0$). After electroweak symmetry breaking, the W^0 and B^0 gauge eigenstates mix to give mass eigenstates Z^0 and γ. The corresponding mixtures of $\tilde{W}^0$ and $\tilde{B}^0$ are the zino $\tilde{Z}^0$ and photino $\tilde{\gamma}$. If SUSY were unbroken, they would be mass eigenstates with masses m_Z and 0 [32][54].

- The SM left- and right-handed fermions have different scalar superpartners. To associate this, the interaction of the gauge bosons with the sfermions must be the same as in the SM fermions. The $\tilde{u}_L$ couples to the W boson, while $\tilde{u}_R$ does not.

- Color conservation prevents gluinos mixing with higgsinos and other gauginos.

- Many SUSY models predict that third-generation squarks and sleptons have substancial mixing angles with the supertpartner of their chiral counterpart [32]. As the top quark gives a dominant contribution to the radiative corrections to the Higgs squared mass, the supersymmetric partner of the top quark, the stop, needs to be relatively light ($\leq$1TeV [47]).
  The superpartners of the left-and right-handed top quarks (referred to as $\tilde{t}_L$ and $\tilde{t}_R$

---

[26]The notion of a superpotential is that it governs all the possible Yukawa interactions of the matter particles with the Higgs field [43].

[27]Charge conjugation and Parity symmetry

left-and right-handed stops) mix into the light and heavy stops [48] ($\tilde{t}_1$ and $\tilde{t}_2$) as:

$$\begin{pmatrix} \tilde{t}_1 \\ \tilde{t}_2 \end{pmatrix} = R(2 \times 2) \begin{pmatrix} \tilde{t}_L \\ \tilde{t}_R \end{pmatrix} \tag{2.15}$$

There is a convention that $m_{\tilde{t}_1} < m_{\tilde{t}_2}$ therefore $\tilde{t}_1$ always denotes the lightest of the two mass eigenstates. The stop mixing matrix R(2×2) is a unitary matrix and the square of its matrix elements gives the left- or right-handed fraction of the stop mass eigenstates. i.e. the square of R_{11} gives the $\tilde{t}_L$ fraction of the $\tilde{t}_1$ and the square of R_{12} gives $\tilde{t}_R$ fraction of the $\tilde{t}_1$. If R_{11} is equal to 1, the light stop is purely the partner of the left-handed top quark. These mass parameters are favorable and suitable for the LHC experiment [48].

$R-$parity and the proton

As a consequence of the invariance between the SM baryon and lepton quantum numbers, the need of a new multiplicative quantum number is introduced in SUSY to avoid the possibility of the proton decay. The decay time of the proton into lepton+meson final states is known experimentaly to take approximatly a minimum of 10^{32} years [32]. In the decay channel $p^+ \to e^+ \pi^0$ in Figure 2.4 a possible proton decay is shown.
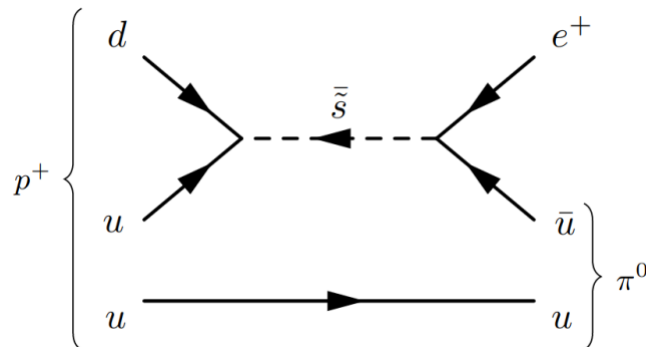
Figure 2.4 Diagram of the proton decay mediated by a strange squark. Both vertices are $R-$parity violating [50].

Going through some of the SM quantum numbers that must be conserved, quarks have the baryon number B assigned to be $\frac{1}{3}$[28] and leptons a lepton number L of 1[29], where the process shown in Figure 2.4 violates leptonic and baryonic number conservation by $\Delta B = 1$, $\Delta L = -1$. The conservation of leptonic and baryonic number is defined as $R-$parity:

$$P_R = (-1)^{3(B-L)+2s} \tag{2.16}$$

The value of P_R is +1 for SM particles and -1 for SUSY particles. By this it is similar to conventional parity.

---

[28] $B = \frac{1}{3}(N_q - N_{\bar{q}})$, with $N_q(N_{\bar{q}})$ number of (anti-)quarks or (anti-)squarks.
[29] $L = N_l - N_{\bar{l}}$ with $N_l(N_{\bar{l}})$ the number of (anti-)leptons or (anti-)sleptons.

Taking the example from before of Figure 2.4, $R-$parity is not conserved and therefore the decay is not allowed. The introduction of this new multiplicative quantum number in SUSY theory, which has to be conserved at every vertex of a Feynman diagram, has several implications, for example [54]:

- There should be a lightest supersymmetric particle (LSP) which needs to be stable, otherwise having a $R-$parity of -1 would decay to a SM particle with $R-$parity of +1. If this LSP is electrically neutral it would be the perfect candidate for dark matter.

- SUSY particles, except the LSP, would decay directly or via intermediate steps to an odd number of LSPs.

- SUSY particles coming from SM processes are produced in pairs assuring to have $R-$parity of +1 in the final state.

SUSY Breaking

Theoretically the selectron weights more than the electron, squarks weight more than quarks and so on. No superpartners have been observed so far. If SUSY is manifested in nature it should be a broken symmetry, and in order to guarantee the solution to the hierarchy problem, it rather be soft as mentioned before [44].

2.3 Benchmark Model

Simplified models are built with the minimum number of particles required to produce a final state of interest. In these models, all SUSY particles except those directly involved in the particular decay mode studied, are put at a very high mass scale. In this way, the free parameters of the model can be greatly reduced. In the simplified models approach, one considers the production of a pair of specific superpartners and follows their decay chain under the assuption that a limited number of decay modes dominate [52].

In this section, four simplified models describing direct stop pair production, used in the stop searches are described. In this thesis only the pure bino LSP model is used. The free parameters in this model are the stop and neutralino masses. The neutralino $\tilde{\chi}_1^0$ is considered to be the LSP, and it also stable due to the assumed R-parity conservation.

LSP Scenarios

There are various LSP scenarios allowed in the MSSM model.

- Pure Bino LSP: this scenario only involves the stop quark $\tilde{t}_1$ and the lightest neutralino $\tilde{\chi}_1^0$ (LSP), as shown in Figure 2.5 a). Looking at the Feynman diagram in figure 2.6 left, the stop quark decays into a SM top quark and the LSP which is kinematically allowed.

- Wino NLSP: in this model (simplified), the wino (chargino) mass is assumed to be twice as large as the bino (lightest neutralino) mass involving as well the second lightest neutralino in the process, as sketched in Figure 2.5 b).

- Higgsino LSP: is a scenario where the mass spectrum of the higgsinos (neutralinos and a chargino) are compressed. The stop decay mode and its branching ratio strongly depends on the chirality (handedness) of the stop [59]. The right-handed stop has a large branching ratio to a bottom quark and a chargino called the bC1 mode (as Feynman diagram 2.6 right), and the left-handed stop decays mostly to a top quark and the neutralino named the tN mode (as Feynman diagram 2.6 left).

- Bino/Higgsino mix: it is not necessary that the LSP is a pure state of either a bino, Bino o a higgsino. This scenario targets a called "Well-tempered Neutralino" as a mix of the bino and wino scenario [56]. The mass spectrum of the gauginos (higgsinos and bino) is expected to be compressed, typically 20-50GeV mass splitting, having a soft lepton as a signature [89].

These main scenarios are shown in Figure 2.5 where it represents less massive sparticles (bottom), and more massive sparticles (top).
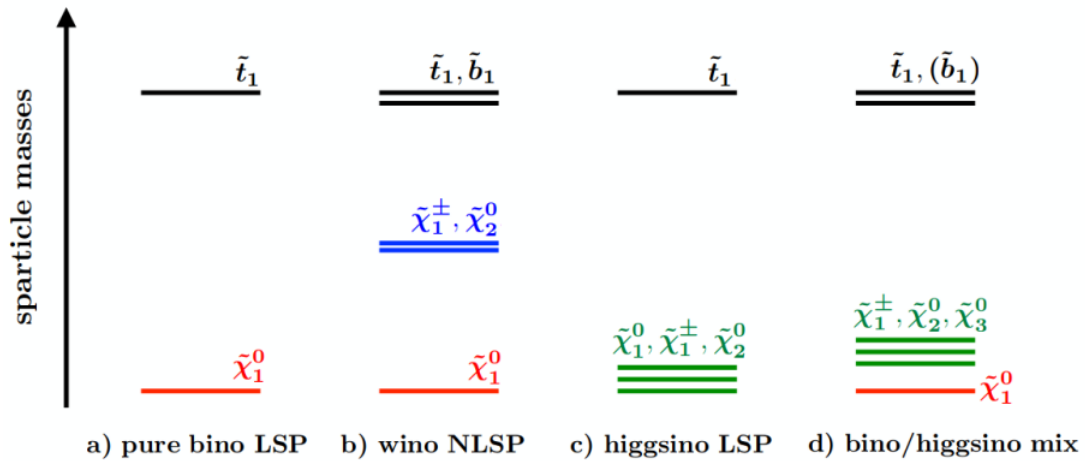
Figure 2.5 Illustration of the sparticle mass spectrum for various LSP scenarios a) Pure bino LSP, b) wino NLSP, c) higgsino LSP, d) bino/higgsino mix. The black lines, as a representation of $\tilde{t}_1$ and $\tilde{b}_1$, decays into various electroweakino states: the bino state (red lines), wino state (blue lines) or higgsino state (green lines). The sparticle masses are greater at the top as the y-axis indicates [89].
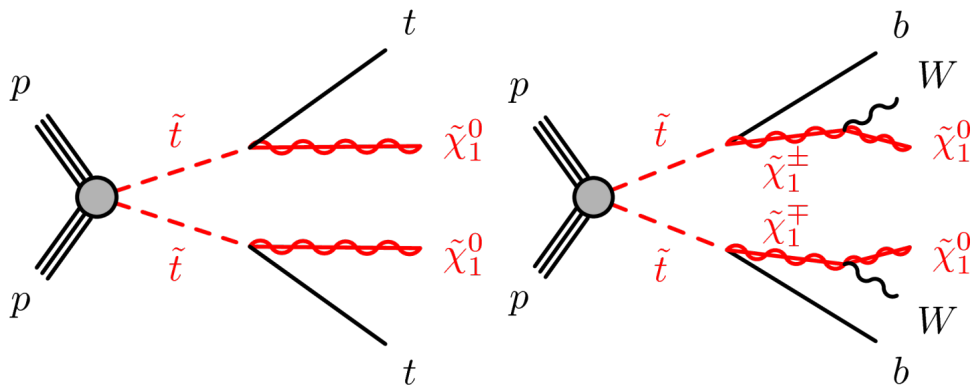

Figure 2.6 Feynman diagram illustrating the scenario where the stop decays into a top quark and the lightest neutralino (right) [57], and the stop decays to a bottom quark and a chargino (left) [58].

Main stop Decay Scenario

The stop can decay in a variety of final states, depending on the mass spectra of SUSY parices. In this analysis we are going to focus in the spectrum of the stop quark and the neutralino in a pure bino LSP model. The mass phase space is presented in Figure 2.7 with the possible decays depending in the mass splitting $\Delta m = m_{\tilde{t}_1} - m_{\tilde{\chi}_1^0}$.
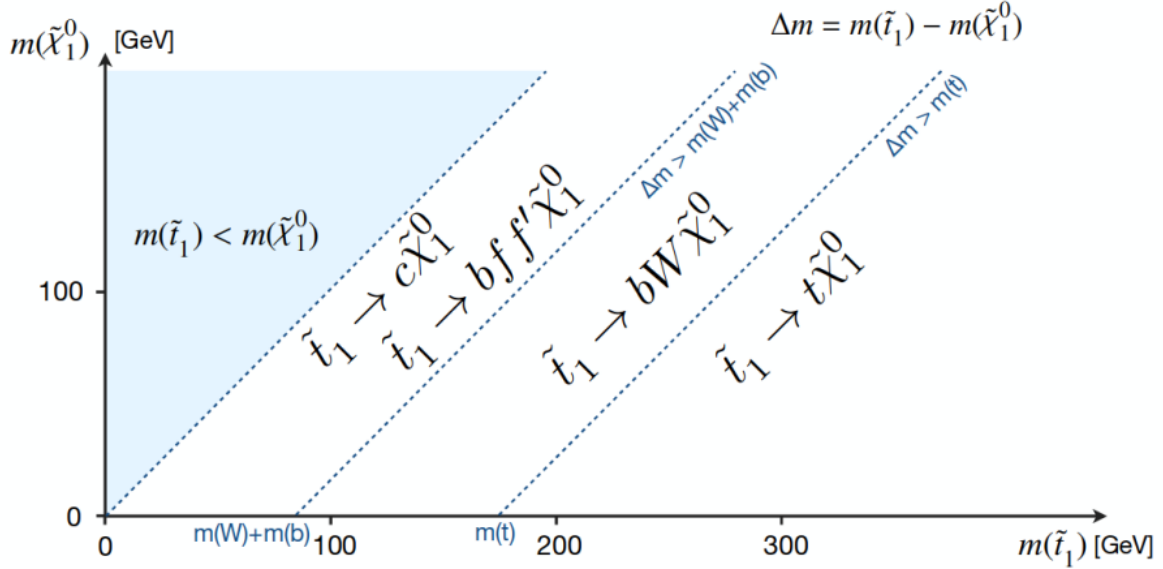
Figure 2.7 Preferred stop decay modes in the plane spanned by the masses of the stop $(\tilde{t}_1)$ and the lightest neutralino $(\tilde{\chi}_1^0)$ taken to be the LSP, in a pure bino LSP scenario. Stop decays to supersymmetric particles other than the lightest neutralino are not taken into account [55].

When the mass difference Δm is bigger than the mass of the top quark ($\sim 173 \text{GeV}$ [11]), the stop decay to a top quark and a neutralino. On the following section I will describe in more detail the three-body decay $(\tilde{t}_1 \rightarrow bW\tilde{\chi}_1^0)$ and the four-body decay $(\tilde{t}_1 \rightarrow bff'\tilde{\chi}_1^0)$; but just to mention that the forbidden region is when the mass of the stop is less than the mass of the neutralino.

3-body decay

In a pure bino LSP scenario the decay through a 3-body decay bWN $(\tilde{t}_1 \rightarrow bW\tilde{\chi}_1^0)$ is possible. The signature that we are looking at the final states is an isolated muon or electron (commonly only denoted as charged lepton) coming from the on-shell W boson leptonic decay, the other W boson would decay hadronically originating two jets, and the undetected neutrino and the two LSPs will give a significant amount of undetected energy, as we can appreciate in Feynman diagram of Figure 2.8 left.

4-body decay

For the four body decay, also in a pure bino LSP scenario, but the difference in the mass Δm is even smaller than in the 3-body case. The leptons in the final state originating from the off-shell[30] W boson decay are expected to have very low momentum.

---

[30]Particles off-shell describe fields that don't have to obey to the equations of motions and also describe virtual particles [60].
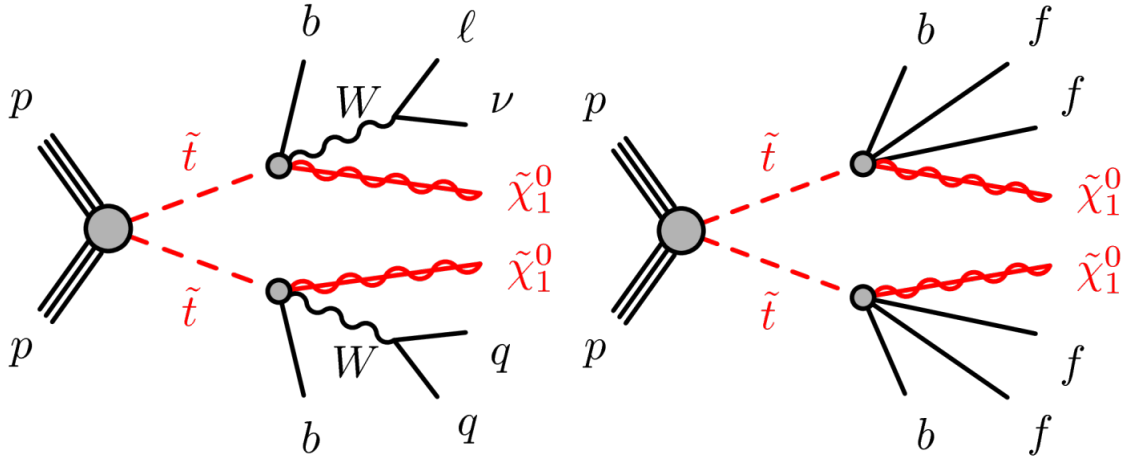
Figure 2.8 Diagrams illustrating the considering signal scenarios. The three-body decay bWN ($\tilde{t}_1 \rightarrow bW\tilde{\chi}_1^0$) on the right. The four-body decay bff'N ($\tilde{t}_1 \rightarrow bff'\tilde{\chi}_1^0$) on the left.

The stop quark can decay to a bottom quark, two different and light fermions and the LSP. This decay yields final states containing a lepton plus jets accompanied with a huge amount of undetected energy.

Chapter 3

Experimental Setup

At the European Organization for Nuclear Search (CERN) physicists and engineers probe the fundamental structure of the universe. The main aim was to establish a world-class fundamental physics research center and it has being doing it so since more than 60 years. It is located at the boarder of France and Switzerland, near the city of Geneva [63]. At CERN the discovery of various fundamental particles took place, contributing to a better understanding of the SM by measuring their properties accurately. Since the discovery of the Higgs boson in 2012 [1][2], the Large Hadron Collider (LHC) is now one of the best tools to search for new physics phenomena beyond the SM.

The contribution of CERN is not only limited to particle physics, but also in fields of medical physics, computer science and engineering. There are different experiments carried out at CERN. Just to mention two of the most notables: The Super Proton Synchroton (SPPS) which lead to the experimentally discover of the Z and W bosons in 1983 and the Large Electron Positron Collider (LEP), providing great precision in the studies of electroweak interactions [65].

3.1 The Large Hadron Collider (LHC) and the Acceleration Chain

CERN decided to give a use to the originally build LEP tunnels [66] after it was out of service. It was decided to install a hadron collider that could operate at very high energies to become the most powerful particle accelerator. The whole tunnel has 27 kilometers in circumference about 100 meter underground and consists of superconducting magnets[1] with a number of accelerating structures to boost the energy of the particles. To collide two beams of equally charged particles, it requires opposite magnet dipole fields, in both beams. In 2010 the LHC started with proton-proton collisions at a center of mass energy of $\sqrt{s}$=7 TeV until 2011 and in 2012 with 8 TeV. The data was taken in these period of time (Run I). Then a shut down came and Run II started in 2015 with $\sqrt{s}$=13 TeV.

To carry out the proton-proton collisions, denoted as pp, several steps are processed, the storage ring cannot accelerate particles from rest. Instead it relies on a chain of pre-accelerators raising the kinetic energy of the particle beams before are injected in the LHC. First protons need to be produced, so with use of an electric field in a hydrogen chamber, the electrons are stripped off the atoms and the hydrogen atoms are ionized yielding protons. Then these protons are accelerated starting at LINAC as shown in Figure 3.1. Then these accelerated protons are transferred to the Proton Synchrotron

---

[1]The main dipoles generate 8.3 T magnetic fields [64].

Booster (PSB) and the energy there is increased up to 1.4 GeV [67]. The next stage in the protons acceleration happens at the Proton Synchrotron (PS) up to 25 GeV proton energy. The Super Proton Synchrotron (SPS) finally takes the protons increasing their energy to 450 GeV, with this amount reached the protons can now be injected to the LHC.
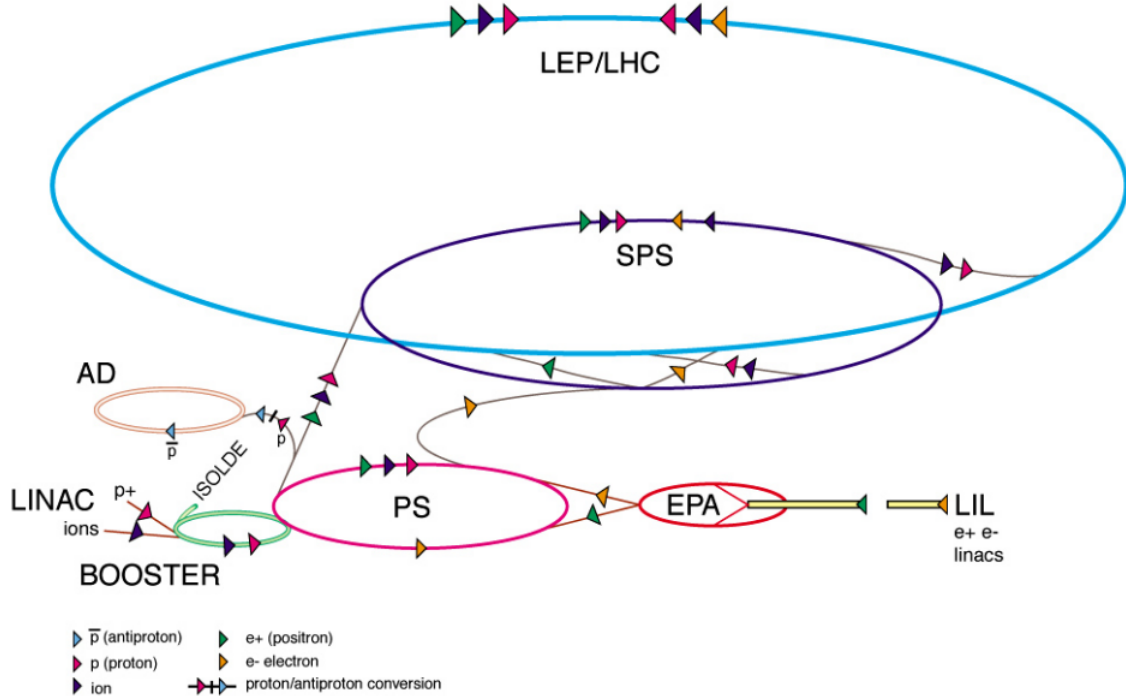
Figure 3.1 CERN Acceleratior Complex [68]. Schematic overview of the accelerators at LEP and LHC and description of the accelerations of protons and their stages. Starting at LINAC through the Proton Synchrotron Booster (PSB), Proton Synchroton (PS), Super Proton Synchroton (SPS) and finally injected to the LHC.

After the acceleration process, the proton beams are brought to collision in four different points where different experiments are settled. There are two general purpose detectors, ATLAS (A Toroidal LHC ApparatuS) [70] and CMS (Compact Muon Selenoid) [71], designed to search for several processes. In particular measuring the Higgs boson and searching for supersymmetric particles. The other two are specialized experiments named ALICE (An Large Ion Collider Experiment) [72] and LHCb (Large Hadron Collider beauty) [73]. At ALICE the investigation with heavy ions collisions takes place to have a better understanding of QCD. Finally LHCb is focused in $B-$physics (decay of hadrons containing bottom quarks) studying the relations and asymmetry between matter-antimatter. An schematic overview of the four experiments near Geneva is appreciated in Figure 3.2.

3.1.1 LHC Parameters

The *center of mass energy* $\sqrt{s}$ is a critical parameter at the LHC for new physics searches. It is defined by an equation describing the momentum of the two beams about to collide by $s = (p_1 + p_2)^2$ with p_1 and p_2 the 4-momenta vectors of each colliding particle. At the LHC each particle have the same energy and momentum, explicitly $p_1 = (E_p, \vec{p})$ and $p_2 = (E_p, -\vec{p})$. The maximal value achieved of the center of mass energy at LHC is 13
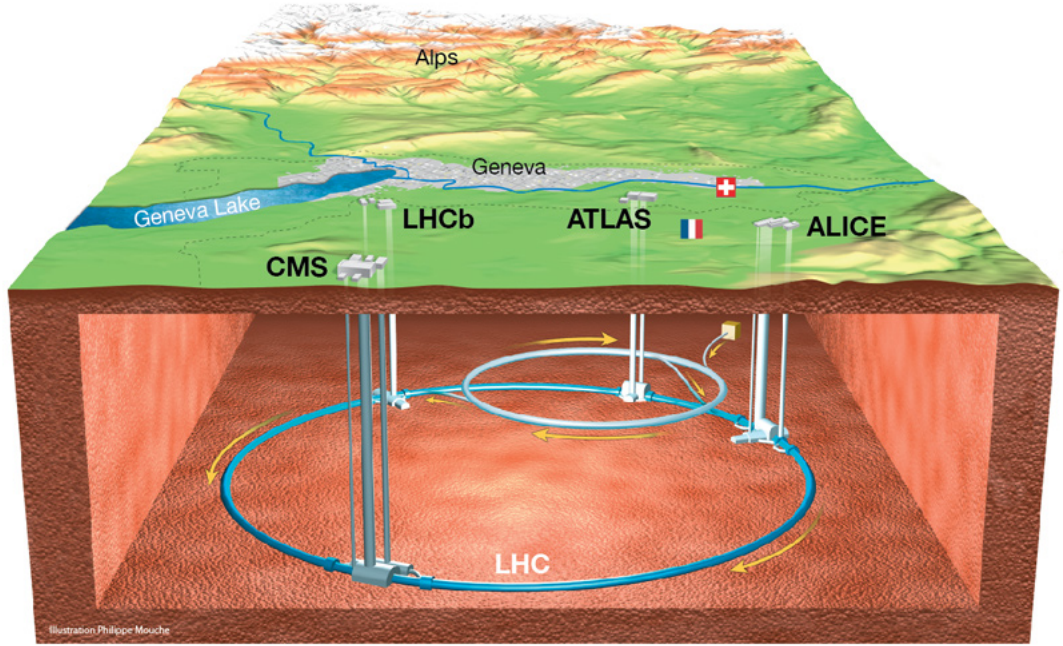
Figure 3.2 Overal view of the LHC. View of the four detectors: ATLAS, CMS, ALICE and LHCb [69].

TeV which is a good scenario to look into BSM physics. With such high energy collisions, massive particles at the TeV scale can be produced, if they exists at such scale.

To measure the performance of the particle collider another important parameter referred as *luminosity* is introduced. The higher the luminosity, the larger accumulated data set, and a large amount of data is needed and essential to perform high precision measurements and study new physics models [74]. Instantaneous luminosity $\mathcal{L}$ is the measure of the number of collisions that can be produced per cm^2 and second. The $\mathcal{L}$ decreases with the run time and it is constrained to machine parameters. After a certain amount of time the circulating beams will be dumped and new ones will be injected in the LHC. The *integrated luminosity* is then the integral of $\mathcal{L}$ over a certain amount of time, generally corresponding at LHC to entire run periods (one or two years of data taking). We can calculate the *number of events* (N_{events}) produced via certain physics processes with a production corss section σ from the integrated luminosity $\int \mathcal{L}dt$ by [75]:

$$N_{events} = \sigma \int \mathcal{L}dt \tag{3.1}$$

The unit of the integrated luminosity is usually inverse barn (b^{-1}), where 1b $= 10^{-24}$cm^2 and σ is analogously in units of barn (b).

3.2 ATLAS Detector

With the LHC delivering proton-proton collisions at very high luminosities, specialized detectors are needed. The ATLAS is a complex particle detector and one of the main four located at LHC. The principle in optimizing the ATLAS experiment is to maximize the discovery potential for new physics such as the Higgs boson and supersymmetric particles, while keeping the capability of highly accurate measurements of heavy quarks and gauge bosons [76]. Particles that escape undetected like neutrinos or not yet discovered particles, carry away a certain amount of energy, which it will be referred and measured

as missing transverse energy (E_T^{miss}, explained in more detail in section 4.2.8).
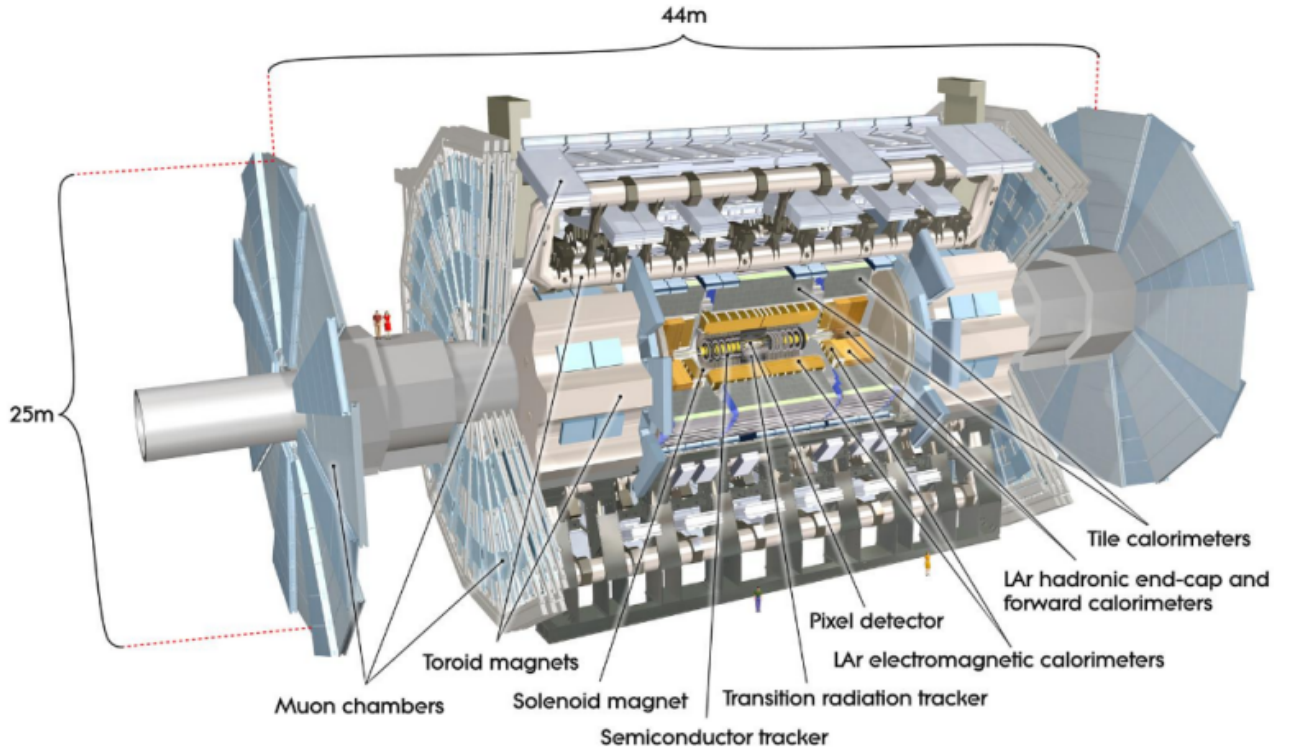
Figure 3.3 The ATLAS detector subsystems [77].

ATLAS is a huge detector, it is 44 meters long and 25 meters high as shown in Figure 3.3. The overall weight is about 7000 tons. The experiment covers broad SM and BSM studies with a collaboration including over 175 institutes from 38 countries with more than 3000 physicist. As seen in Figure 3.3, ATLAS is composed by several sub-detector systems. In Figure 3.4 the purpose of each sub-detector is illustrated.

Combining the information of the different sections in ATLAS, different types of particles can be identified. Figure 3.4 shows how each sud-detector reacts to different types of particles with the following description. When particles do not interact with the detector material being like invisibles in all the sub-detector systems, like the neutrinos, we have a rise to the missing momentum in the transverse plane.

3.2.1 ATLAS Coordinate System

ATLAS has a cylindrically symmetric geometry. It uses a right-handed Cartesian coordinate system, where the $z-$axis is oriented along the beam pipe and it is pointing in anti-clockwise beam direction, the $x-$axis is defined to point to the center of the LHC ring, while the $y-$axis is pointing upwards as shown in Figure 3.5 (left). The reference point is set where a *pp* interaction point takes place, and if not, to the center of the detector. In spherical coordinates system, r is the radial distance to the reference point, the polar angle θ is measured in the $y-z$ plane, and the azimuthal angle ϕ is measured from the $x-$axis in the transverse plane [79]. When the geometry of the detector and the interaction with Lorentz vector particles is described, pseudorapidity η is often used instead of θ and it is defined as:

$$\eta = -\ln(\tan\frac{\theta}{2}) \tag{3.2}$$
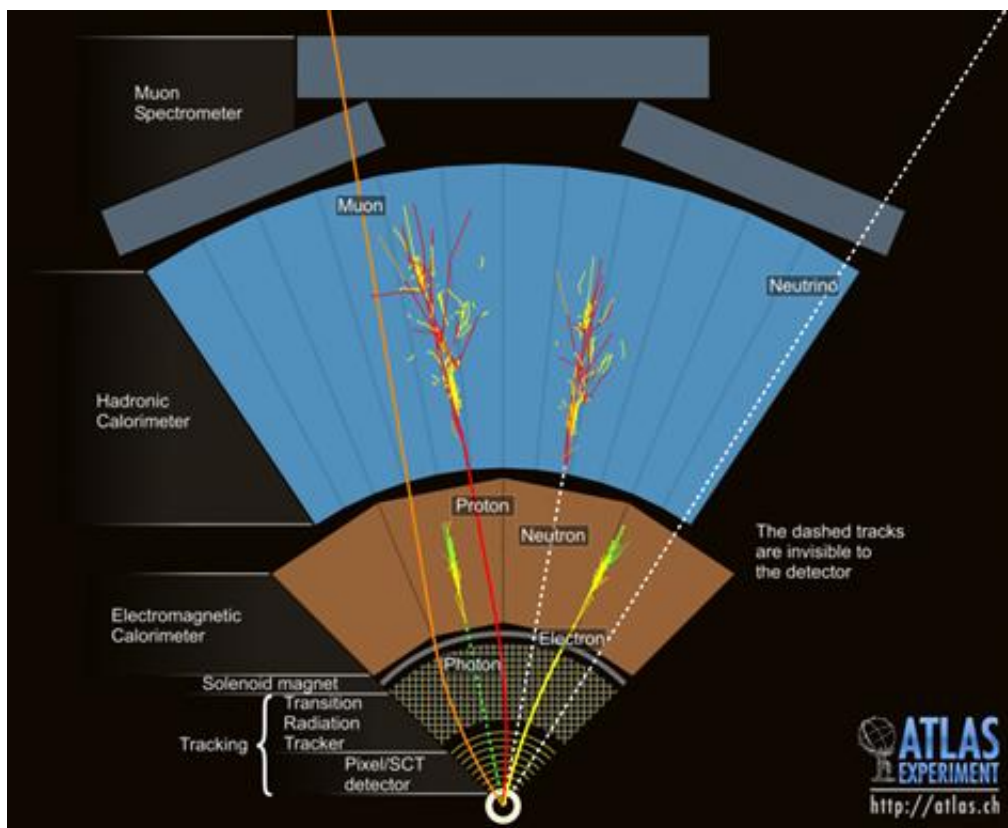
Figure 3.4 Transverse overview of ATLAS sub-detector system [78].

In Figure 3.5 (right) the pseudorapidity is zero along the $y-$axis and along the $z-$axis it approaches to infinity. It is used to give a description of the trajectories of massless objects. For massive objects the rapidity difference is an invariant under a boost along the $z-$axis and is defined as [80]:

$$y = \frac{1}{2}\ln(\frac{E + p_z}{E - p_z}) \qquad (3.3)$$
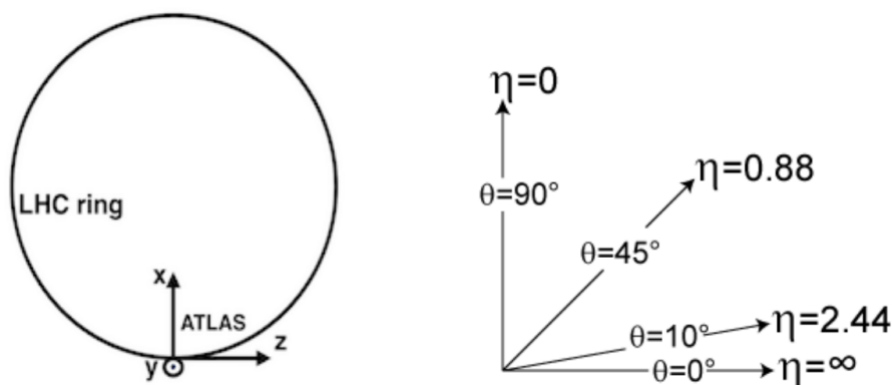
Fugure 3.5 The ATLAS Cartesian coordinate system (left). Values of pseudorapidity η for different polar angles θ [81].

In the collisions quantities as energy and momentum are conserved effectively in the $x - y$ plane transverse to the beam axis, by this some kinematic variables are defined in the transverse plane, such like transverse momentum p_T and transverse energy $E_T = \sqrt{m^2 + p_t^2}$ of a particle with mass m are naturally of particularly interest in the hadron collision experiments. Another useful parameter is the angular distance of two

objects in the azimuthal-pseudorapidity angle as $\Delta R = \sqrt{\Delta \eta^2 + \Delta \phi^2}$.

3.2.1 Inner Detector

The detector system closest to the beam line is the inner detector (ID). It is 6.2 m long and 2.1 m in diameter placed in a 2 T magnetic field generated by the superconducting solenoid and it is the part responsible on tracking charged particles. By the Lorentz force a charged particle travels through the ID in curved tracks, so the charge of the particle and its momentum can be inferred by the strength and direction of the curvature of the track.

Is composed of three tracking sub-detectors which are independent but complementary to each other. The innermost is the pixel sub-detector offering a full coverage in ϕ and providing a high spatial resolution. One additional layer is the Insertable B-Layer (IBL), being the fourth layer of the pixel detector and the closest to the interaction point, improving the tracking, vertexing the identification of hadrons containing $b-$quarks ($b-$tagging).

Outside the pixel detector the semiconductor tracker (SCT) [82] is placed, using long and narrow silicon microchips arranged in parallel to the beam axis allowing a precise tracking along the transverse plane to the beam axis.

Finally, the transition radiation tracker (TRT) in the most outer part, complements these two high-precision tracker detectors and it consists of a barrel and two end-caps. It is a straw tube detector which is made of transition radiation material. Each straw tube is filled with gas mixture which charged particles ionized. The wall of the straw tube is made of polyamide which enhances the photon emission of the passing charged particles. The amount of radiation depends on the particle mass. Therefore in addition the TRT provides information to identify electrons and charged pions in the $r - \phi$ plane.

3.2.3 Calorimeter

The ID is surrounded by the calorimeter structure consisting of an electromagnetic calorimeter (ECAL) and a hadronic calorimeter (HCAL). The calorimeters measure the energy of particles by stopping them in the calorimeter material, this requires the calorimeter to be sufficient large, so the particles after passing the ID, the particles are stopped in the calorimeter, giving rise to a shower of other particles [83]. The ATLAS detector uses sampling calorimeters which are composed of passive and active materials placed in a like sandwich structure.

Electrons and photons are detected in the ECAL, which uses lead plates as the passive material and liquid argon (LAr) as the active one, measuring the electromagnetic showers. ECAL is enclosed by the HCAL detecting strong interacting particles. HCAL is composed of a tile calorimeter in the central region using steel as an absorber and some others scintillating tiles as the active material. The tile calorimeter is subdivided itself in two parts, both parts using LAr as the active material: the hadronic end-cap calorimeter using cooper as the absorbing medium, and the forward calorimeter using cooper and tungsten as absorber.

3.2.4 Muon Spectrometer

Muons can penetrate the ECAL and the HCAL, so a muon spectrometer (MS) is needed and it is the outermost sub-detector system of the ATLAS detector, as appreciated in Figure 3.4. Just like the ID, the MS measures momenta by bending the muons trajectories in a magnetic field. By its three air-core toroids producing a magnetic field configuration, the magnetic field is almost orthogonal to the muons trajectory.

The MS consists in three cylindrical layers in the barrel region, measuring the track bending by monitored drift tubes (MDTs). In the end-cap, the MS has three vertical wheels perpendicular to the beam constitute of high granularity cathode strip chambers (CSC) used for the tracking.

3.2.5 Trigger and Data Acquisition

During the shutdown in the transition period to Run II, the ATLAS trigger system was upgraded [84]. The three-level trigger system of Run I was reduced to two stages, with the previous two high-level triggers merged to one. By reducing the number of levels the data transfer rates are reduced allowing to run improved high-level trigger (HLT) algorithms.

To reduce the large amount of data that is produced with the collisions in ATLAS, triggers have to be used in order to provide a certain selection of events that are to be stored. A two-level trigger system is deployed to filter out events irrelevant for the analysis [85]. The level 1 triggers (L1) search for high- momentum particles based on a subset of the detector information available to reduce the time needed for the decision. Using data from the calorimeters and the muon system the L1 trigger identifies so-called regions of interest (RoIs) in the detector, given by certain coordinates in the $\eta - \phi-$space. This happens within 2.5 μs and reduces the event rate from 40 MHz to 100 kHz [86].

The second trigger step is the HLT and in contrast to the L1 trigger system it is purely based on software and either takes the information on the RoI's from L1 as an input or uses the full-event information for offline-like algorithms. Different combinations (chains) of HLTs and L1 triggers, targeting various signatures, are used simultaneously. The selection criteria of the HLT chains are tuned to reduce the total data rate further to about 1 kHz and the selected events are written to persistent storage.

34

Chapter 4

MC Simulation and Reconstruction of Objects in ATLAS

This chapter summarizes the data sets and Monte Carlo (MC) simulations which are used in the analysis described in this thesis. The reconstructed events using the collected information are presented. Object reconstruction and identification is described in section 4.3.

4.1 Collected Data

As explained in section 3.1.1 and equation 3.1, the amount of collected data by ATLAS is given by the integrated luminosity. The analysis in this thesis used proton-proton collision data recorded in 2015 and 2016 at $\sqrt{s}$=13 TeV corresponding to a integrated luminosity of 36.1fb^{-1}.

4.2 Monte Carlo Simulations

A very important aspect in various physics experiments are Monte Carlo (MC) simulations. They are used to model the distributions of the theoretical expectations. Then we can form predictions directly comparable to real data. We can visualize the real data and simulated data (MC) processes in the following way:

- Real data:

$$\text{Collision} \rightarrow \text{Detector} \rightarrow \text{Trigger} \rightarrow \text{Reconstruction}$$

- Simulated data:

$$\text{Event generator} \rightarrow \text{Simulated Detector} \rightarrow \text{Trigger} \rightarrow \text{Reconstruction}$$

MC events are generated using the so called MC event generators using parameters tuned to ATLAS [95], which are capable on simulating a wide range of the most interesting processes expected at the LHC, SM processes and probably BSM. Event generators are usually required to extract signal of new physics from the background of SM processes. Then the events are processed by a detector simulation. Physics objects in the events processed without the generator detector simulation are called *generator level objects*, while after the detector simulation they are referred to as *reco-level objects*. In Table 4.1 the MC generators used for the analysis are listed which are used to simulate the signal and

background processes.

The generation of specific processes includes different parts like: hard scattering and interaction, parton showers, hadronization and decays [93] as shown in Figure 4.1. Hard scattering constitutes on the process of interest in the collision, it happens at large scale and with large momentum transfer. During hard interaction, heavy objects can be created. Parton showers are the result of initial state radiation (ISR) and final state radiation (FSR) where quarks and gluons can irradiate off gluons, which themselves can split into a quark-antiquark pair or irradiate again gluons and so provoking a "shower". The simulation of these showers starts from the hard processes downwards to lower momentum scales. In the order of 1 GeV, perturbation theory breaks down so that gluons and quarks starts the hadronization process.

At proton-proton collisions more interactions can take place, in which additional, soft particles (low energetic) are produced. These interactions are called underlying events or pile-up. At the last step we have the particle decays. Many particles produced in the collision have unstable resonances. Modeling their decay into particles leads to what is later observed in the detector.
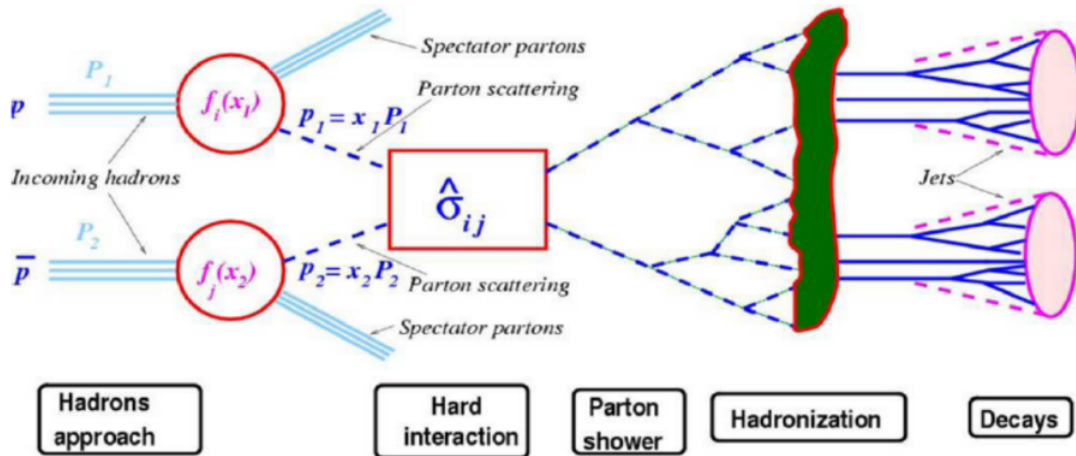
Figure 4.1 Various stages of a typical hadronic reaction in proton-proton collisions [94].

The number of MC events (N_{MC}) must be scaled to the integrated luminosity ($\mathcal{L}$) of the data samples and the predicted cross section of the MC processes (σ_{MC}) in order to compare them to the number of data. Two additional correction factors must be applied. The k-factor (k) describes the effects of the next-to-leading order corrections, and the filter efficiency ϵ_{filter} accounting for the input filters of the generator to choose certain particles. These components lead to the scaling factor f_{MC} defined as:

$$f_{MC} = \frac{k \cdot \epsilon_{filter} \cdot \int \mathcal{L}dt \cdot \sigma_{MC}}{N_{MC}} \qquad (4.1)$$

4.2.1 Monte Carlo Standard Model Samples (Background)

The SM processes which are more relevant for this thesis are the top quark pair production ($t\bar{t}$), W boson production in association with jets and single top.

Process	Generator(s)	PS and Hadr.	Corss-section Calculation
$t\bar{t}$	POWHEG-BOX v2 [96]	PYTHIA 6 [97]	NNLO+NNLL [98]-[103]
Single-top (Wt)	POWHEG-BOX v2	PYTHIA 6	NNLO+NNLL [104]-[106]
W+jets	SHERPA 2.2.0 [107]	SHERPA	NNLO [107]
Diboson	SHERPA 2.2.1	SHERPA	NNLO
$t\bar{t}+V$	MG5_ aMC NLO 2.2.2 [108]	PYTHIA 8 [109]	NLO [108]
SUSY signal	MG5_ aMC NLO 2.2.-2.4	PYTHIA 8	NLO+NLL [111]

Table 4.1 Overview of the nominal simulated samples taken from [89] and used for the analysis. The single top processes includes the $t-, s-$ and Wt channels.

- $t\bar{t}$ • The top-antitop quark processes are produced via the strong interaction and have a signature of two W bosons and two $b-$jets ($t \rightarrow W + b$). The $t\bar{t}$ is also characterized by the number of charged leptons from the W boson decay:

  – Dileptonic decay: $t\bar{t} \rightarrow W^+bW^-\bar{b} \rightarrow l^+\nu_l b l^- \bar{\nu}_l \bar{b}$. The background is low, but also small branching ratio.

 – Semileptonic decay: $t\bar{t} \rightarrow W^+bW^-\bar{b} \rightarrow q_1\bar{q}_2 b l^- \bar{\nu}_l \bar{b}$[1]. Higher branching ratio and a relatively low background.

  – All hadronic decay: $t\bar{t} \rightarrow W^+bW^-\bar{b} \rightarrow q_1\bar{q}_2 b q_3\bar{q}_4\bar{b}$. Very high branching ratio and huge background.
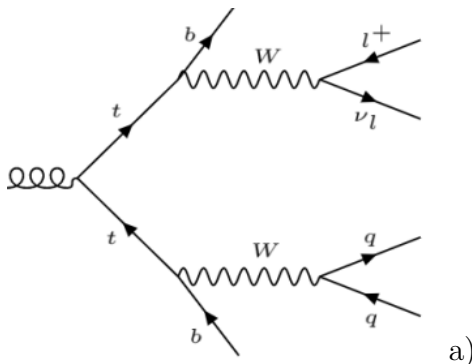
Figure 4.2. $t\bar{t}$ Semileptonic decay example [127].

The semi-leptonic $t\bar{t}$ decay (see. Fig. 4.2), is very similar to the signal 3-body process with the exception of the two missing $\tilde{\chi}_1^0$ (see Fig. 2.8 left). The nominal $t\bar{t}$ MC cross section of the simulated processes are normalized to next-to-next-to-leading order (NNLO) [98] with the gluon emission resummation of soft gluon emission at next-to-next-to-leading logarithmic (NNLL). They are generated with NLO generato POWHEG [96] interfaced to PYTHIA [97] for parton showering and hadronization. Some additional $t\bar{t}$ samples are used for systematic uncertainties evaluation and generated with MG5_ aMC NLO (NLO) interfaced to PYTHIA 8, SHERPA and POWHEG+HERWIG++ [112][113] for evaluation of systematic uncertainties.

- W+**jets** • The combination of W and jets has a large cross section. The samples are generated with SHERPA 2.2.0 [107] and merged with SHERPA parton shower [114] using the ME+PS@NLO prescription [115]. The W+jets events were further normalized to the NNLO cross-sections [89].

---

[1]And charge conjugate processes.

- Wt • The single top samples are calculated just as the $t\bar{t}$ samples. For the simulations of Wt process, the diagram removal (DR) scheme is used [117]. Additional samples for $Wt + b$ are generated with MG5_ aMC NLO (LO) interfaced to `PYTHIA` 8, in order to assess the interference effect between the singly and doubly resonant processes as a part of the Wt theoretical modeling systematic uncertainty. This is explained in more detail in section 6.3.2.

4.2.2 Monte Carlo Signal Samples

Models where the supersymmetric partners of the top quarks are directly produced, are used to interpret the results of the analysis in the following chapters, and referred as signal. Samples for direct stop pair production are generated with `MADGRAPH` [116] interfaced with `PYTHIA 8` [111] for parton showering and hadronization. In the pure bino LSP scenario described in section 2.3, the stop is decayed with `MadSpin` [118] interfaced to `PYTHIA 8`. For the $\tilde{t}_1 \rightarrow bW\tilde{\chi}_1^0$ and $\tilde{t}_1 \rightarrow bff\tilde{\chi}_1^0$ signal samples, the `MadSpin` emulates kinematic distributions such as the mass of the bW system to a good approximation without calculating the whole matrix element (ME). For the `MadSpin` samples the stop is assumed to be composed mainly of $\tilde{t}_R(\sim 70\%)$ [87].

The SUSY signal simulated via MC for different masses of the stop and neutralino are called mass points. The considered mass points for the 3-body decay case are: $m(\tilde{t}_1, \tilde{\chi}_1^0)$ = (350,200), (350,230) and (350,260) GeV are considered. For the 4-body decay case $m(\tilde{t}_1, \tilde{\chi}_1^0)$ = (350,270),(350,300) and (400,350) GeV.

4.3 Object Definitions

As discussed in section 3, the reconstruction of various particles types requires the combined information of different parts of the ATLAS detector, by this assigning energy deposits and tracks to the studied particles. However, this is not always straightforward and miss identifications can happen. To avoid this certain quality criteria are introduced which help to identify the particles as good and correctly as possible.

Not all reconstructed particle candidates are relevant for every analysis, the different signal models under study predict certain object properties in the events so, additional selection criteria are applied on different variables to reject events that are not needed, most likely background. These criteria include e.g. restrictions on the number of certain particles or a minimum value in transverse momentum. As in many analyses, there are several steps, starting with a preselection, so the objects that pass this preselection are named *baseline* objects. Afterwards some more sophisticated criteria are required to obtain the event selection, so the remaining particles are the *signal* objects. Only the signal objects are considered as a potential outcome of supersymmetric processes. Either way we need to include baseline objects for the background estimation. In this thesis the analysis selects final states with exactly one lepton. Therefore events are reconstructed by requiring at least one reconstructed vertex, exactly one electron (e) or muon (μ), several jets and large amount of missing transverse energy (E_T^{miss}).

4.3.1 Event Cleaning

Data corruption given by detector problems, software bugs, noise bursts and other issues can happen. Before using the events for the analysis, events must pass an event cleaning

resumed in some stages [88]:

- **Good Run List** The Good Run List (GRL) is used to remove luminosity blocks affected by detector problems (aprox. 1-2 minutes of data taking).

- **Primary Vertex** The events kept have a reconstructed primary vertex with at least two tracks with $p_T >$[2]400MeV [89]. The primary vertex of an event is defined as the vertex with the highest $\sum p_T^2$ of the associated tracks. Events are rejected if no primary vertex is reconstructed.

- **Cosmic Muons** Cosmic-ray showers produced in the atmosphere can overlap with collision events. Since ATLAS is deep underground, the particles reaching the AT-LAS detector are predominantly muons [90]. To avoid this a veto is applied in cosmic muons candidates. Criteria depending on the longitudinal and transverse parameter of impact in reference to the primary vertex are placed.

- **Jet Cleaning** Jets arising from cosmic rays, beam induced backgrounds or detector noise are suppressed by applying a quality criteron named `VeryLooseBand` described in [90]. It applies certain requirements depending on the signal pulse shape in the LAr calorimeter, track variables and energy ratios.

4.3.2 Object Definitions

Only events that pass the event cleaning can be considered as potential candidates for the analysis. The object selection consists on: preselection, overlap removal (OR) and signal selection. The OR tries to ensure that there is no double counting of objects. The events that pass the OR are submitted to a final process to select the signal objects. Baseline leptons that passes the OR but fail at least one signal criteria, are named loosed leptons.

Electron

Electron candidates are reconstructed from energy clusters formed in the ECAL matched to a track in the inner detector, and identified using the `VeryLooseLH` definition in [91], which is the criteria they must fulfill. These criteria set requirements in the showers widths and energy deposits in the ECAL or the number of hits in the detectors of the ID. Energy calibration is applied to reconstruct the electrons in Monte Carlo to be capable to reproduce the performance of the electron measured in data. The baseline electrons required to have a $p_T >$5 GeV and $|\eta| <$2.47 and they are used for the OR between jets and electrons and the residual baseline electrons are used to veto events with extra leptons.

To suppress electrons from secondary vertices, signal electrons must have a transverse impact parameter with respect to the primary vertex (d_0) satisfying $|d_0|/\sigma_0 <$5 with σ_0 the uncertainty. Also the distance from this point to the primary vertex along the z_0 beam direction, needs to satisy $|z_0 sin\theta| <$0.5mm. Furthermore, they must pass several p_T dependent isolation criteria. This guarantees better discrimination against semileptonic decays of hadrons and miss-identified jets [89].

---

[2]p_T is the transverse momentum.

Muon

Muons are reconstructed from combined tracks formed in the ID and MS. Baseline muons up to $|\eta|$ <2.7 are used and they require to have a p_T >4 GeV and fulfill the "Loose" [92] identification criteria. Signal muons must pass as well the baseline requirements and in addition to have impact parameters of $|d_0|/\sigma_0$ <3 and $|z_0 sin\theta|$ <0.5mm and satisfy the "Medium" [92] identification criteria. Like electrons, muons have a similar isolation criteria but with a fix cut on track-based isolation energy over the muon p_T, furthermore there is no separation between loose or tight muons [89].

Jets

Jets are made of hadrons and other particles which are produced by hadronization of a gluon or a quark and tend to travel approximately the same direction.

Jets are reconstructed from three-dimensional topological clusters in the calorimeters. The cluster starts with a cell with a certain ratio of energy deposit above a threshold. Then, neighboring calorimeter cells that have significant energy deposits compared to the expected noise are grouped into the clusters. Using these clusters, jets are reconstructed by the anti-k_t jet clustering algorithm [119] with a distance parameter of R=0.4. The reconstructed jet candidates are calibrated [120] to account for the effects from i.e. the calorimeter non-compensation and inhomogeneities using calibration factors which depend on the energy and η of the jets. The calorimeters have a different response for electromagnetic and hadronic constituents of the jets. The energy losses in inactive regions and the energy deposits which are below the noise threshold are not used in the jet reconstruction. The longitudinal energy leakage of the shower also causes the energy loss in the calorimeters. In addition, particles from pileup interactions (additional pp collisions) also affect jet energies; these additional particles increase the jet energy response and make it luminosity-dependent.

In the simulation truth jets are formed from truth particles wiath a lifetime $\geq$ 10 ps. produced in the fragmentation model of the MC generator. The calibration factors are so derived from simulation and defined by [120]:

$$R(E, \eta) = \langle \frac{E_{reco}}{E_{truth}} \rangle \qquad (4.2)$$

where E_{reco} is the reconstructed energy and E_{truth} is the truth jet energy. The jet energy calibration also corrects for pileup effects. The calibration is then validated with test-beam and collision data. This p_T and η-dependent jet energy scale (JES) calibration corrects the energy of the jet to be the same as the energy of the corresponding particle level on average. There is also a pile-up correction to the direction of the jet to point to the primary vertex, and a further correction to reduce the quark-gluon composition and topology dependence (GSC). The baseline jets are required to have a p_T >20GeV and are used to perform the overlap removal. Signal jets are required to have p_T >25GeV and $|\eta|$ <2.5. Events containing a jet that does not pass the jet quality requirements ("jet cleaning") are vetoed from the analysis to suppress detector noise and non-collision background [121].

$b-$ Tagging

Jets containing $b-$hadrons are identified as $b-$jets. The $b-$jet identification is based in

general on the measure of the first and secondary vertex. In this analysis a discriminant MV2c10 [122] is used, which is an algorithm based on a boosted decision tree (BDT). It is trained also to discriminate against c jets. By cutting on the output weight of the algorithm, one can discriminate b jets from light jets and c jets. This BDT combines inclusive secondary vertex and $b-$hadrons decay chain properties together with the b-tagging logarithmic likelihood ratios based on the signed impact parameters of associated tracks. Different cut values provide different b-tagging efficiencies and light and c jets rejection rates. These cut values are referred as operating points. The operating point at ϵ_b=76.97% $b-$tag efficiency is used, corresponding to an inclusive efficiency in a simulated $t\bar{t}$ sample. This corresponds to a rejection of ~ 130 for jets originating from gluons ans light-flavor quarks, and ~ 6 for jets induced by charm quarks [89].

Jets passing the pileup cleaning requirement and the $b-$tagging acceptance of $p_T >$20GeV and $\eta <$2.5 are $b-$tagged. Scale factors that take discrepancies between data and MC in tagging efficiencies are applied to the MC events.

Hadronic τ

One of the main backgrounds of this analysis is $t\bar{t}$ decaying into an electron or muon and a hadronic τ. To identify the τ's it is important to build discriminating variables against this background. Hadronically decaying τ leptons are reconstructed as jets but use a separate jet calibration, using the "Loose" identification criteria [123], which has a 60% (50%) efficiency for reconstructing τ decaying into one (three) charged pions. With these tau candidates the energy scale is corrected and these taus require to have one or three associated tracks with the corresponding jet with total electric charge opposite to the selected electron or muon with $p_T >$20GeV and $|\eta| <$2.5 [124].

Photons

Photon candidates are not used in the main event selections of the presented thesis but are used in background estimations and cross checking of $t\bar{t}+\gamma$ regions. Photons are reconstructed the same way as electrons but without the requirement on the ID track match. They are identified using the "Tight" [125] criteria. They are required to have a $p_T > 145$GeV³ and $|\eta| <$2.37 excluding track regions of 1.3$< |\eta| < $1.52.

Missing Transverse Energy

The missing transverse energy E_T^{miss} is defined as the magnitude of the missing transverse momentum vector $\vec{p}_T^{miss}$. The missing transverse momentum vector is measured from the momentum imbalance in the transverse plane of the detector as the negative sum of the transverse momenta of baseline jet candidates, electrons, muons and an extra soft term built from high quality tracks associated to the primary vertex but no to the baseline objects [126]. The photons and the hadronically decaying τ are not considered but enter as jets, electrons or via the soft term allowing E_T^{miss} to be almost independent of pileup effects. In addition tracks that are not associated to reconstructed objects are included in the E_T^{miss} calculation.

---

³In order to be a photon trigger plateau (`HLT_ g140 _ loose`) [87].

Overlap Removal

There are some ambiguities when the reconstruction of objects takes place. It can happen that an electron can also be reconstructed as a jet in the calorimeters. This type of ambiguities needs to be solved in order to avoid double counting of the energy of the calorimeters cells that are shared by the electron and jets candidates. Also the procedure needs to be capable of retaining two different but close objects. A solution for this kind of problems is the overlap removal (OR) optimized using simulation. In the analysis the following overlap removal is used based on an acceptance to real leptons, maximizing the signal acceptance and rejection of dileptonic events, detailed below [87]:

- Electron/Muon OR: If a muon overlaps with any electron within $\Delta R < 0.01$[4] the electron is removed and the muon is kept, unless the muon is calo-tagged, in which case the electron is kept and the muon is removed.

- Electron/Jet OR: When a baseline electron and a baseline jet are found within $\Delta R(e, jet) < 0.2$, and the jet is not $b-$tagged, the object is reconstructed as an electron and the overlapped jet is removed. If the jet is $b-$ tagged then the $b-$jet is kept and the electron is removed.

- Muon/Jet OR: If a baseline muon can be ghost matched [128][5] to a baseline jet within $\Delta R(\mu, jet) < 0.4$ and the jet is also not $b-$tagged, the object is reconstructed as a muon if:

  - The jet has less than 3 tracks or

  - The ratio of the p_T of the muon and the jet is greater than 0.7 ($p_T^{muon}/p_T^{jet} > 0.7$).

- Jet/Lepton OR: If a jet satisfying the previous steps gets to overlap with an electron or muon (l) in a cone with radius $R = 0.04 + \frac{10}{p_T^l GeV}$, up to a maximum radius of 0.4, then the lepton is removed.

- Electron/Tau OR: When an electron satisfies the previous steps and overlaps with a tau candidate in a cone radius of $\Delta R(e, \tau) < 0.1$, then the tau is removed.

- Photons are not used in the nominal analysis but used to cross-check in the $t\bar{t}+\gamma$ region:

  - Electron/Photon OR: When an electron that satisfies all the previous steps overlaps with a photon within a cone of radius $\Delta R(\gamma, e) < 0.1$, the photon is removed.

  - Photon/Jet OR: Jets that overlaps with photons in a cone with radius $\Delta R(\gamma, jet) < 0.2$ are removed. In the rest of the regions photons are not considered and the overlapping of photons/jets are treated as simply jets.

As a reminder all baseline and signal objects are those who have passed the OR procedure.

---

[4]Rapidity ($y = \frac{1}{2}ln(\frac{E+p_z}{E-p_z})$) is used instead of the pseudorapidity (η) when computing ΔR in the overlap removal procedure.

[5]Referred as an infinitely soft particle ("a ghost") with certain rapidity and azimuthal angle added in the jet-finding.

Chapter 5

Discriminating Variables and Preselections for the 3- and 4-Body Stop 1L Analysis

This chapter describes the analysis strategies and methods used in the searches for the supersymmetric top partner at $\sqrt{s}$=13 TeV. This thesis studies the 3-body decay channel and introduces preliminary studies for the 4-body decay. We are looking specifically into final states with only one isolated electron or muon, jets and a big amount of missing transverse energy. The kinematic variables described in this section are used to define a preselection for the 3- and 4-body decay channels.

5.1 Strategy

The analysis described in this thesis considers a simplified model of the stop decay scenario as described in section 2.3. The searches are performed where the final state particles of a signal event require one electron or muon, one neutrino originating from the decay of an on- or off-shell W boson, two b quarks (reconstructed as b jets), two light-flavor quarks and two LSPs. The LSPs are not interacting with the detector material and cause large E_T^{miss} together with the neutrino. Therefore, the event selection in the analysis requires exactly one isolated electron or muon, large E_T^{miss} and at least one b-jet.

The analysis focuses on the pure bino spectra of the mass of the lightest stop quark $\tilde{t}_1$ and the neutralino $\tilde{\chi}_1^0$. In this phase space the 3-body decay channel occurs in a pure bino LSP decay where the mass difference of the stop quark and the lightest neutralino $\Delta m = m_{\tilde{t}_1} - m_{\tilde{\chi}_1^0}$ is less than the mass of the top quark. The 4-body decay channel happens when Δm is less than the mass of the W boson.

The dominant backgrounds originate from $t\bar{t}$2L and the other sub-backgrounds are $t\bar{t}$1L, single top Wt production, where both W bosons decay leptonically and one of the charged leptons is not identified, as well the W+jets production. These dominant backgrounds are normalized in dedicated control regions and extrapolated to the signal regions to estimate the expected number of background events in the signal region. The extrapolation relies on transfer factors (TFs) obtained from the simulation and are explained in chapter 6.

5.2 Baseline Selections

The selection of the objects that have passed the OR procedure are [89]:

- **Trigger.** The trigger is selected for a suited final state in the investigation, as in ours, events with large E_T^{miss} are required, the dataset used in the analysis is recorded using unprescaled E_T^{miss} triggers[1], so called xe triggers [87]. The HLT online E_T^{miss} is constructed using a baseline algorithm with the HLT trigger firing a threshold of 110 GeV. The associated L1 trigger threshold is at 50 GeV. Events are selected based on an applied selection of exactly 1 lepton, at least 4 (or 2) jets and at least one b-tag jet. To reduce the multijet contamination further cuts are applied: $m_T > 30$ GeV and $\Delta\phi(\vec{p}_T^{miss}, \text{jet}_1) > 0.4$ with $i = 1,2$.
  The trigger efficiency[2] is above 98% for $E_T^{miss} > 230$ GeV, which is the minimum in the different regions of the analysis that uses the xe-trigger [87].

- **Electron.** Electrons are required to have $E_T > 5$ GeV and $|\eta^{cluster}| < 2.47$ [89].

- **Muon.** Muon candidates are required to pass $p_T > 4$ GeV and $|\eta| < 2.7$ acceptance cuts.

- **Jets.** At baseline level jets are required to have a $p_T > 20$ GeV, and are used in the OR procedure.

  - **b-tag.** Are required to pass $p_T > 20$ GeV and $\eta < 2.5$.

- E_T^{miss}. The missing transverse momentum is calculated using the default ATLAS tools, namely the METUtilities tool [87]. All baseline electrons, muons, and jets before overlap removal are input to the tool, while no photons or (hadronic) tau objects are provide.

5.3 Discriminating Variables

The variables described are primordially used to separate signal events from the SM background events in the signal, control and validation regions explained in the chapter 6.

- m_T • Requiring one isolated lepton (l), several jets and a big amount of missing transverse energy (E_T^{miss}) selects samples enriched with semileptonic $t\bar{t}$ events and W+jets events. Both backgrounds can be reduced by implementing a transverse mass (m_T) to be above the mass of the W boson mass and defining m_T as:

$$m_T = \sqrt{2 \cdot p_T^l \cdot E_T^{miss}(1 - cos\Delta\phi(\vec{l}, \vec{p}_T^{miss}))} \tag{5.1}$$

  where the lepton p_T is p_T^l and $\Delta\phi(\vec{l}, \vec{p}_T^{miss})$ is the azimuthal angle between the lepton and the $\vec{p}_T^{miss}$ making the assumption that the lepton mass is negligible. After this requirement the dominant background is dileptonic $t\bar{t}$ with one miss-identified lepton. The $t\bar{t}$ products include high m_T values and two or more hight p_T neutrinos resulting in a big amount of E_T^{miss}.

---

[1] `HLT_ xe110_ mht _ L1XE50`
[2] $\epsilon = \frac{N_{passed}}{N_{total}}$ with N the number of events.

- am_{T2} • Decays through the three-body channel are possible if Δm is smaller than the mass of the top quark, as mentioned in section 2. The signature is described by the shape of the bW system, where one of the main discriminative variables is a variant of the stransverse mass (m_{T2}) [129] variable referred as asymmetric m_{T2} (am_{T2}). This variable is a generalization of the transverse mass applied to signatures where two particles are not detected directly. In Figure 5.2 an illustration of the $t\bar{t}$ topology is presented targeted by the am_{T2} variable.

The m_{T2} variable measures masses of particles produced at the hadron colliders, where the longitudinal momentum of the hard scattering process is unmeasured. It may be used when particles are pair produced, with each decaying to one particle that is directly observed and one particle that is not directly observed. It is analogous to the m_T only that it helps to measure a pair particle production and calculate a massive unseen particle. It helps us to describe decay topologies with two branches, a and b (see Fig. 5.1). In both branches there are particles with fully measured momenta and some other particles with their momenta not measured directly. The sum of the four vectors of the measured momenta in a branch i are defined as $p_i = (E_i, \vec{p}_{T_i}, p_{z_i})$ and the sum of the four vectors of the unmeasured momenta are denoted instead of the letter p by the letter q in the same way $q_i = (E_i, \vec{q}_{T_i}, q_{z_i})$. As usual we have $m_{p_i}^2 = E_i^2 - \vec{p}_i^2$ and $m_{q_i}^2 = E_i^2 - \vec{q}_i^2$ respectively. In general the m_{T_i} of the particles in branch i can be given by [89]

$$m_{T_i}^2 = \left(\sqrt{p_{T_i}^2 + m_{p_i}^2} + \sqrt{q_{T_i}^2 + m_{q_i}^2} \right)^2 - (\vec{p}_{T_i} + \vec{q}_{T_i})^2 \qquad (5.2)$$

m_{T2} is defined as a minimization of the allocation of $\vec{p}_T^{miss}$ between $\vec{q}_{T_a}$ and $\vec{q}_{T_b}$ of the maximum of m_{T_a} or m_{T_b}:

$$m_{T2} = \min_{\vec{q}_{T_a} + \vec{q}_{T_b} = \vec{p}_T^{miss}} \{ max(m_{T_a}, m_{T_b}) \} \qquad (5.3)$$

The undetected particle is the W boson for the branch of the lost lepton and the other missed particle is the neutrino associated to the measured charged lepton branch as in Figure 5.2 (Branch a)). The dotted circles suggests the misidentified particles for each branch. For the $t\bar{t}$ events with a lost lepton, the am_{T2} variable is a powerful discriminant between signal and background in a more compressed region of the phase space as it is for the 3-body decay region. Taking into account some important points:

- Measured Particles: In branch a) and b), both $b-$jets are identified based on the highest $b-$tagging weights.

- Unmeasured Particles: For branch a) it is a W boson decaying leptonically with the unidentified lepton as such. Of branch b) the unmeasured particle is the neutrino associated to the charged identified lepton.

- Input Masses: In equations 5.1 and 5.2, the input masses would be $m_{q_a} = m_W = 80 GeV$ and $m_{q_b} = m_\nu = 0 GeV$

This variable is a main discriminant in the 3-body decay due to the mass difference of the stop quark and the neutralino is below the top quark mass for signal. Consequently this am_{T2} variable is bounded from above by the mass of the top quark

meaning that am_{T2} signal peaks at low values ($\approx$90 GeV), while dileptonic $t\bar{t}$ decays typically have a peak at values nearer the top quark mass.
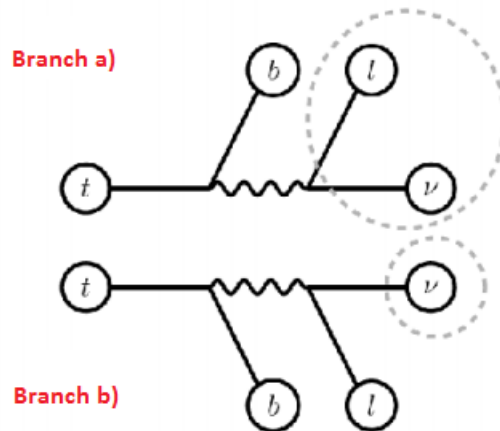
Figure 5.1 Illustration of the construction of the am_{T2} variable. It is used to discriminate against dileptonic backgrounds with one lost lepton and to describe an asymmetric decay. The dashed line indicates the misidentified particles. In branch a) the not reconstructed particle is a charged lepton with its associated neutrino, while in branch b) the missed particle is the neutrino associated to the identified lepton.

- m_{T2}^{τ} • It is another variant of m_{T2} used to suppress dileptonic $t\bar{t}$ events where one of the two leptons is a tau that decays hadronically τ_{had}. In this asymmetrical topology, a '$\tau-$jet' is proposed for the visible particle in one branch and the measured lepton for the other branch.

  - Measured Particles: In branch a) shown in Figure 5.3, the τ^3 candidate is measured and for branch b) it is the identified lepton.

  - Unmeasured Particles: As the dashed lines show in Figure 5.3, for branch a) are two neutrinos, one associated to the τ production from the W boson decay, and other to the τ hadronically decay. In branch b) the unmeasured particle is the neutrino associated to the identified lepton, comming from the W boson decay.

  - Input masses: Using equation 5.1 and 5.2, the input masses would be m_{q_a}=0 GeV and m_{q_b}=m_{ν}=0 GeV

With this variable an effective hadronic τ veto can be developed in two cases:

1. If an event does not have a reconstructed τ that passes the loose likelihood identification, the event is not vetoed.

2. The event is vetoed if the τ candidate results in an m_{T2}^{τ} <100 GeV. The m_{T2}^{τ} is contructed from the signal lepton and the recontructed τ as the visible particles with test masses zero [89].

This variable is used in the 3-body decay region.

---

[3]Identified as described in section 4.2.6
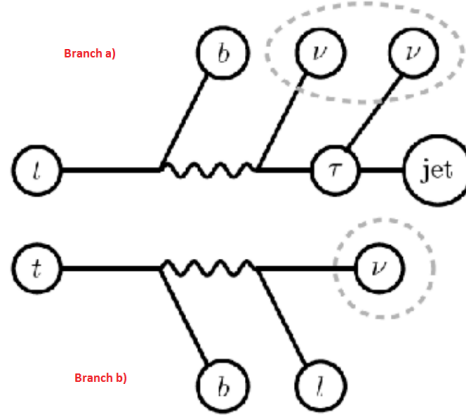
Figure 5.2 Illustration of the discriminating variable m_{T2}^{τ} used to discriminate against hadronically decay tau. The dashed lines indicates the particles that are lost or unidentified in both branches of an asymmetric decay [87].

- *topness* ● It is a variable used in a control region explained in section 6.2.4 separating single top events for the 3-body decay. As the dominant backgrounds to semileptonic stop searches are dileptonic $t\bar{t}$ where one lepton is either too soft or too forward to be identified [130]. Dileptonic top events are reconstructible when both leptons are identified, but when one lepton is lost, this is no longer true and the missing particle is taken as an assumption (as in the am_{T2}). So the condition is that the reconstructed center of mass energy of the event is minimized. A function S is constructed which is a a type of a χ^2-function, and it quantifies how well an event can be described and reconstructed subject to the dileptonic $t\bar{t}$ hypothesis in the form of:

$$S(p_{W,x}, p_{W,y}, p_{W,z}, p_{\nu,z}) = \frac{(m_W^2 - p_W^2)^2}{a_W^4} + \frac{(m_t^2 - (p_{b1} + p_l + p_\nu)^2)^2}{a_t^4} \qquad (5.4)$$

$$+ \frac{(m_t^2 - (p_{b2} + p_W)^2)^2}{a_t^4} + \frac{(4m_t^2 - (\sum_i p_i)^2)^2}{a_{CM}^4}$$

This variable is designed to suppress partially reconstructed $t\bar{t}$ events. The first three arguments of S are the components of the non-reconstructed W boson 3-momentum $p_{W,x}, p_{W,y}, p_{W,z}$. The W is assumed to decay leptonically, but the lepton is not identified and is only noticeable as missing transverse momentum. $p_{\nu,z}$ is the longitudinal momentum of the neutrino from the other W boson decay where the charged lepton was successfully identified. The denominators a_k determine the relative weighting of the mass shell conditions ($p_\nu^2 = 0, p_W^2 = m_W^2$). As suggested by the authors in [130], the values to take are a_W=5 GeV, a_t=15 GeV and a_{CM}=1 TeV, and they should not be smaller than typical resolutions. The inputs to S are two jets, a lepton and $\vec{p}_T^{miss}$. To find the best possible reconstruction, the sum runs over both of the possible pairing of jets with a reconstructed W boson and keep the one that minimizes S. Also both $b-$jets are taken into account, if only one $b-$tagged jet is present it is used together with the leading or sub-leading jet. So at last, *topness* is defined as:

$$t = \ln(minS) \qquad (5.5)$$

The minimization is limited such that the observed transverse momentum is associated to the unobserved W boson (decaying into a not-reconstructed lepton and a neutrino) and a neutrino from the second top decay branch.

- $\Delta\phi(jet_i, \vec{p}_T^{miss})$ • This variable is the azimuthal opening angle between the jet i and $\vec{p}_T^{miss}$ used to suppress multijet events where the $\vec{p}_T^{miss}$ is aligned with a jet. Multijet events can pass the event selection if a jet is misidentified as a lepton or if a real lepton from a hevay flavour decay satisfies the isolation criteria, and large E_T^{miss} can occur due to these missed-jets. This variable is used in both channels, the 3- and 4-body.

- $\Delta\phi(\vec{p}_T^{miss}, l)$ • The azimuthal opening angle between the direction of $\vec{p}_T^{miss}$ and a electron or muon l. In SM processes, $t\bar{t}$ semileptonic correlates the azimuthal direction of the missing transverse momentum in processes generated by the neutrino with the azimuthal angle of the charged lepton. Is used in the three body stop decay, where the neutralinos also contributes to the missing transverse momentum, semileptonic $t\bar{t}$ processes are distributed arbitrarily. Nevertheless the separation in dileptonic $t\bar{t}$ SM processes is weaker but more alike to the SUSY event studied in the analysis, due to the second neutrino, the azimuthal angles of the l and the neutrino are no longer correlated.

- $\Delta R(b_1, b_2)$ • Denotes the opening angle in $\eta - \phi$ space between the first two highest-p_T jets that are $b-$tagged. This variable is only used when a two or more $b-$tag jets are required, in particular for enriching single top events explained in section 6.2.4.

- Hadronic Top Reconstruction • It is a tool used to supress backgrounds like the dileptonic $t\bar{t}$ decay not containing a hadronically decaying top quark. To realize the hadronic top recontruction, an algorithm based on the anti-k_t clustering is used requiring a small radius of the jets. First all small radius jets are clustered using the anti-k_t algorithm with a large radius parameter R_0=3.0 corresponding to a top quark p_T of 120 GeV. Afterwards the very large radius jets are shrunk until its radius matches their p_T using $R_i = 2 \times m/p_T$ taking as m=175 GeV the parameter of the top mass. At last the optimal radius is compared with the actual radius of the candidate, and the candidate can be taken, reclustered again or rejected. There are two parameters to compare the range around the optimal radius that is considered acceptable with R_{up}=0.3 and R_{down}=0.5 (refering as up-higher and down-lower values of the clustered candidate radius) [89]. The reconstruction of the hadronic top decay is used in this thesis for the 4-body preselection, and it is useful because is inefficient at low values of the top quark p_T.

- $\Delta\phi(p_T^{miss}, \vec{b} - jet)$ • Is the azimuthal angle between the missing transverse momentum and the $b-$tagged jet with the largest momenta. This is a discriminating variable used in the 4-boday decay analysis. It is very effective in suppressing W+jets background due to the emission angle of the $b-$jets from gluon splitting which aren't correlated to other decay products. After applying this variable, the background is left mainly with $t\bar{t}$ processes.

- p_T^l/E_T^{miss} • Is the ratio of the lepton p_T and the missing transverse energy. This variable is used in the 4-body decay channel, which requires a very low p_T lepton, and with this variable the sensitivity is improved as shown in chapter 7.

Figure 5.3 shows the comparison between data and MC simulations for the variables after applying the preselectrion criteria for the 3-body decay described in Table 5.1 except the one displayed in the distribution. The comparison shows that the discriminating variables are reasonably modeled in the simulation. Figure 5.4 shows the other kinematic

variables distributions described in this section for the 3-body decay, after the preselection in Table 5.1.
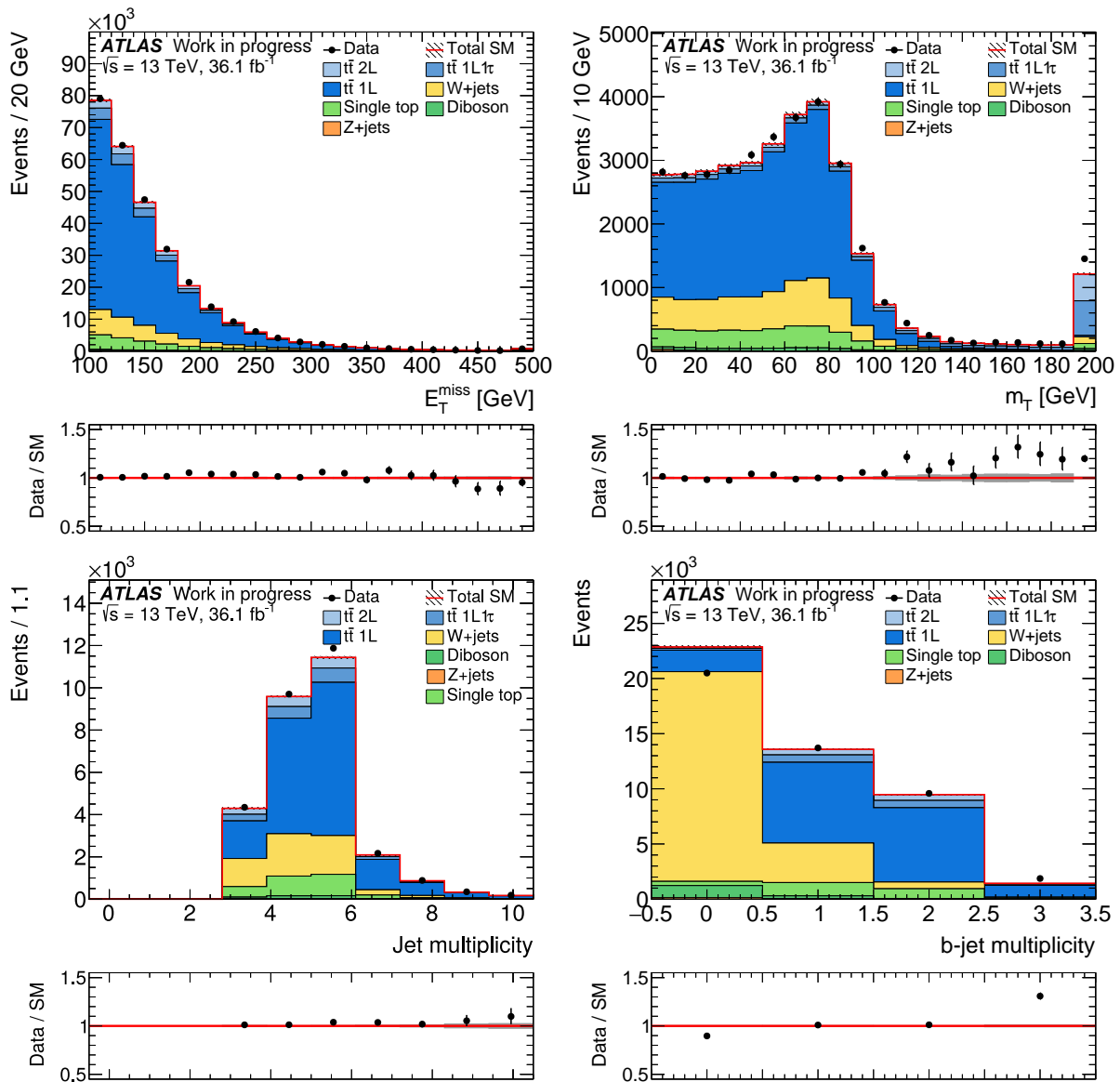
Figure 5.3 Comparison of data with the estimated backgrounds after the applied preselection from table 5.1, except the variable displayed in the distribution.
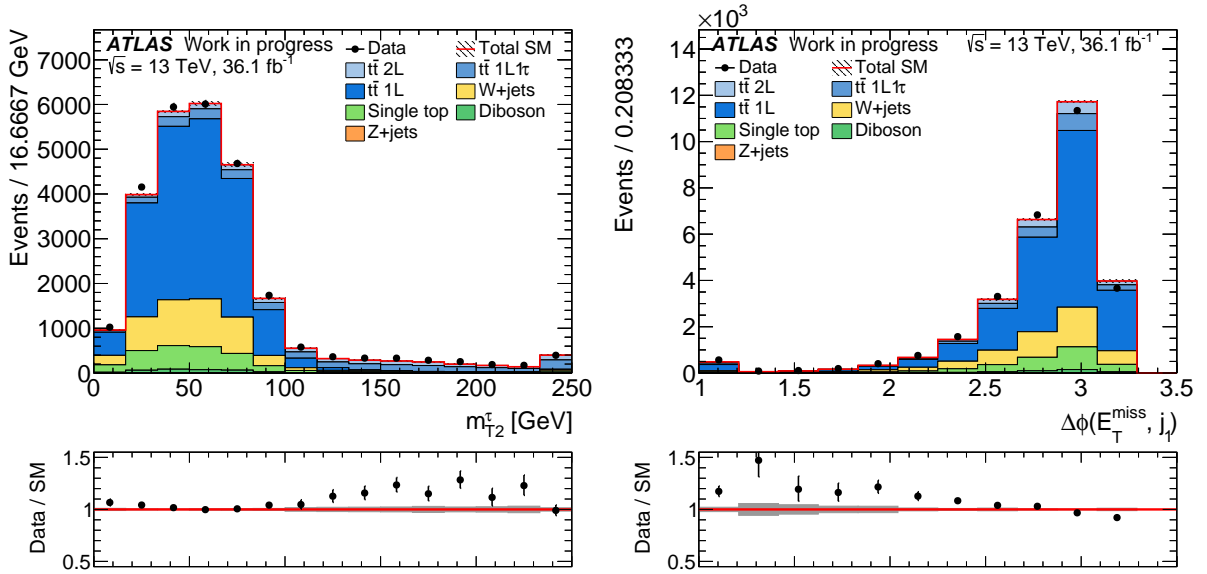
Figure 5.3 Comparison of data with the estimated backgrounds after the applied preselection from table 5.1, except the variable displayed in the distribution.
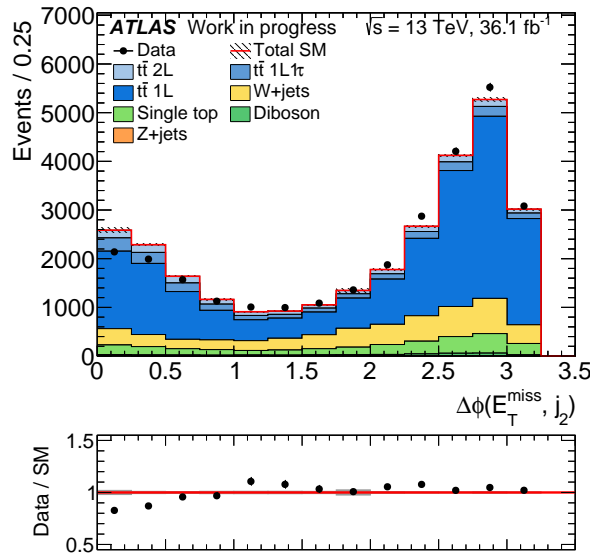
Figure 5.3 Comparison of data with the estimated backgrounds after the applied preselection from table 5.1, except the variable displayed in the distribution.
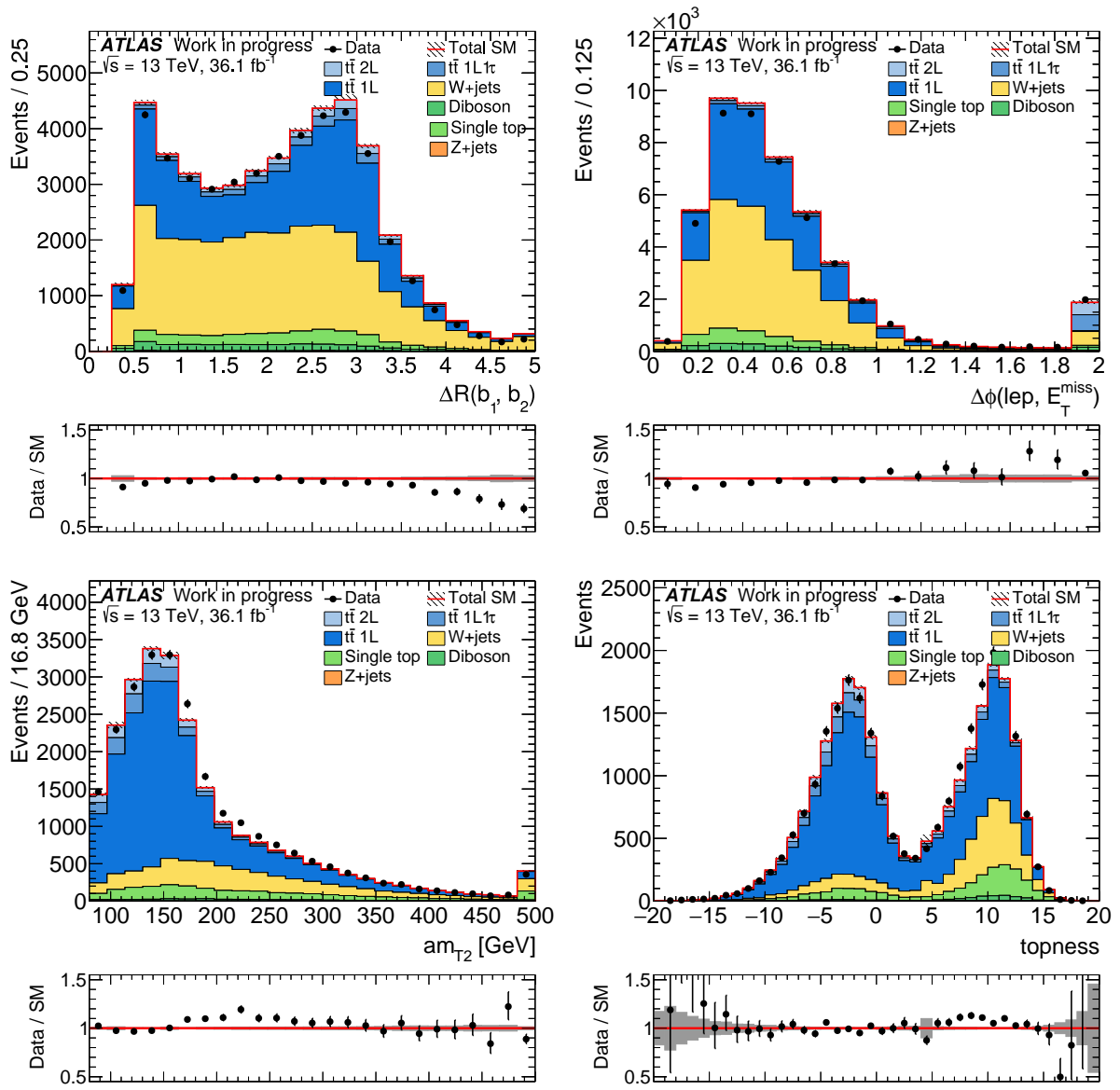
Figure 5.4 Comparison of data with the estimated backgrounds after the applied prese-
lection from table 5.1 of the kinematic variables for the 3-body decay.

Selection	Comments
xe triggers	
jet cleaning	veto events that fail the loose jet criteria
exactly one signal lepton	no additional baseline leptons
≥ 4 signal jets	
$\text{jet}_{1,2,3,4}$ $p_T > 25 GeV$	
number of leptons, tightness	$= 1$ "loose lepton"
Lepton p_T	≥ 25 GeV
$E_T^{miss} > 230$ GeV	
$m_T > 30$ GeV	control of QCD/multijets
$|\Delta\phi(j_{1,2}, \vec{p}_T^{miss})| > 0.4$	control of QCD/multijet background
m_{T2}^τ based τ-veto ($m_{T2}^\tau > 80$ GeV)	remove events with hadronic τ events

Table 5.1 Common preselection for the three-body decay analysis [87].

Selection	Comments
xe triggers	
jet cleaning	veto events that fails the loose jet criteria
exactly one signal soft lepton	$p_T > 4(5) GeV$ for mu(el), no additional baseline leptons.
≥ 2 signal jets	
$\text{jet}_{1,2}$ $p_T > 25 GeV$	
≥ 1 $b-$jet	
$E_T^{miss} > 230$ GeV	
$|\Delta\phi_{1,2}, \vec{p}_T^{miss}| > 0.4$	control of QCD/multijet background
No reclustered jet candidates or	
mass of hadronic top	< 150 GeV
	(To satisfy a veto in reclustered
	hadronic top quarks $m_{top}^{reclustered}$.)

Table 5.2 Common preselection for the four-body decay analysis [87].

5.3 Event Preselections

There is a common preselection for all the stop main decay scenarios used for the signal regions using the E_T^{miss} trigger mentioned in section 5.2, because only events with $E_T^{miss} > 230$ GeV are selected. This preselection is useful in order to check the kinematic distributions considered in the analysis. Here two preselections are used. For the three-body analysis the preselection shown in Table 5.1 is used.

The four-body preselection has some other requirements including: a very soft electron(muon) $p_T > 5(4)$GeV, the first jet needs not to be $b-$tagged, a veto in reclustered hadronic top quarks events for events where no reclustered jet candidates are found or the mass of the hadronic top < 150 GeV (less than the mass of the top quark). In table 5.2 the preselection of the 4-body decay is presented. In Figure 5.5 the n-1 plots after the 4-body preselection is showed and in Figure 5.6 the other kinematic variables distribution.
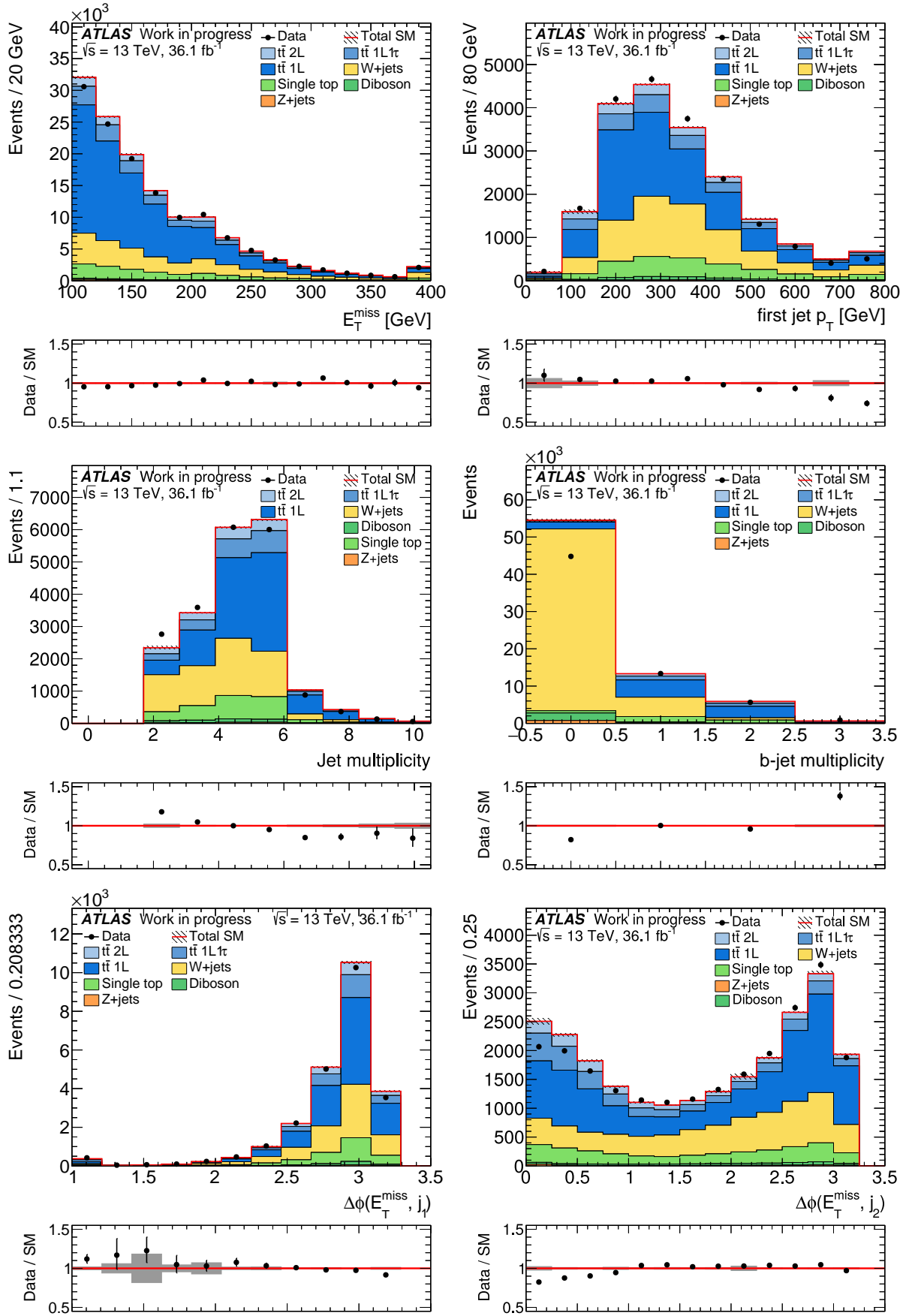
Figure 5.5 Comparison of data with the estimated backgrounds after the applied preselection from table 5.2 for the 4-body region, except the variable displayed in the distribution.
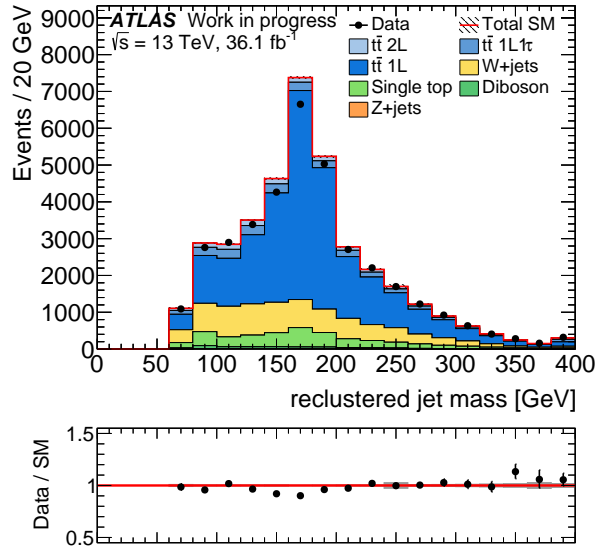
Figure 5.5 Comparison of data with the estimated backgrounds after the applied preselection from table 5.2 for the 4-body region, except the variable displayed in the distribution.
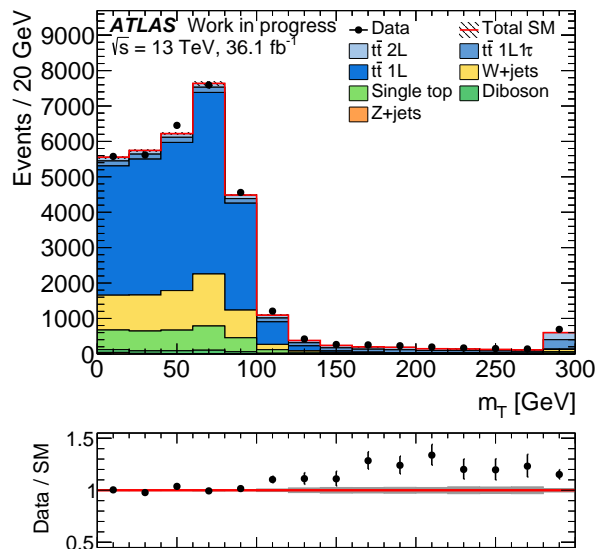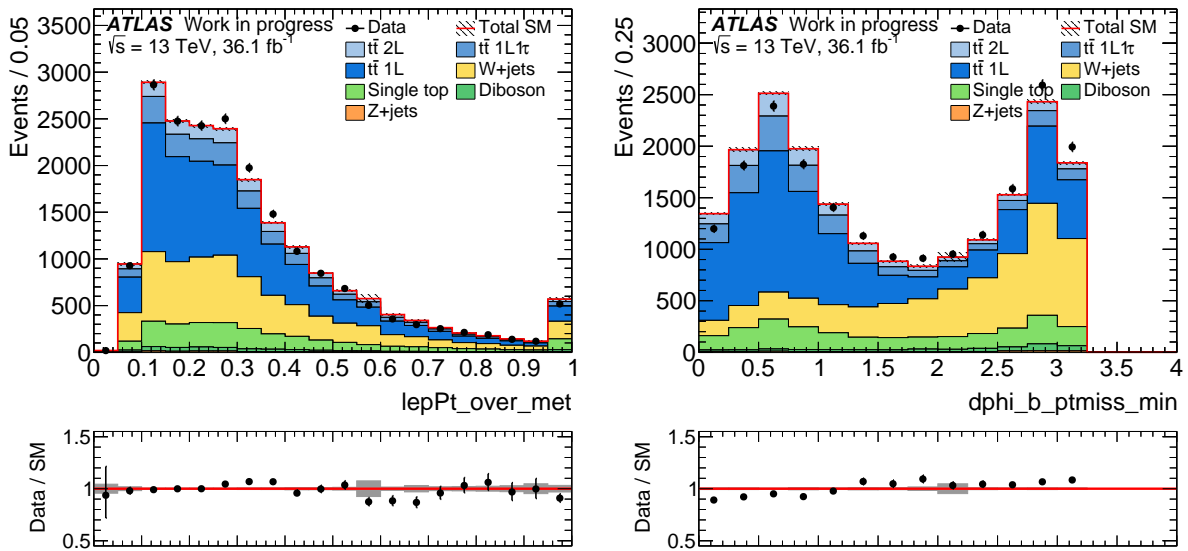
Figure 5.6 Comparison of data with the estimated backgrounds after the applied preselection from table 5.2 of the kinematic variables for the 4-body decay.

Chapter 6

Signal and Background Estimation for the 3-body Analysis

Using the signal region (SR) definition explained in section 6.1, the SM backgrounds can be reduced to an acceptable level. SM processes which have the same signatures as the expected SUSY signal remain. It is important to have a good understanding of these processes to know their contribution in the SR. To estimate background processes contaminating the SR, control regions (CR) are defined. The CRs are designed to have high purity for one type of SM background. They are defined by a set of selection criteria similar to those defining the signal region but with some criteria altered to retain a sufficiently large number of background events and reject most events from the signal and other background processes. Kinematically the CRs should be as close as possible to the SR to have a small extrapolation from CR to the SR.

The prediction obtained from the CR is then verified by comparing it to the observed data in dedicated validation regions (VR), which are typically defined between the SR and the CR. The VRs are used to validate the prediction obtained from the CRs. All the SR, CRs and VRs are required to be orthogonal to each other.

6.1 Signal Region

A signal region (SR) is a region of the phase space defined by the selection criteria on the kinematic variables [132]. The signal region optimization is based on simulation and uses the expected number of signal and background events in the SR to construct a figure of merit. Cuts on the kinematic variables are optimized to suppress most of the background, while increasing the proportional fraction of the signal. A single-binned signal region corresponds to a simple cut-and-count analysis in which the number of events in the signal region is counted.

In the analysis, SUSY samples with the masses of $m(\tilde{t}_1, \tilde{\chi}_1^0) = (350,200)$, $(350,230)$ and $(350,260)$ GeV are considered

The signal region called bWN and is defined in table 6.1. The event yields are shown in Figure 6.1 (left) for 36.1 fb^{-1}. Figure 6.1 (right) shows in a pie chart the breakdown of the individual SM contributions to the signal region. It is clear that the predominant SM background is the dileptonic $t\bar{t}$, with a fraction of $t\bar{t}$2L and $t\bar{t}$1L1τ, contributing with a $\sim$80% of the total background. It is important to calculate the contribution of the signal in the defined region. The mass point with the more event yields is taken for the calculation. In this case is the mass point $m(\tilde{t}_1, \tilde{\chi}_1^0)$=(350,200) GeV. The signal contamination is given

bWN	
Variable	cut
Leading jet p_T	> 50 GeV
jets 2,3,4 p_T	> 25 GeV
E_T^{miss}	>300 GeV
m_T	> 130 GeV
am_{T2}	< 110 GeV
number of $b-$ jets	≥ 1
$\Delta\phi(\vec{p}_T^{miss}, l)$	< 2.5
Signal Contribution	$\approx 92\%$

Table 6.1 Event selection defining the **bWN** signal region. The common preselection defined in Table 6.1 is used [89]. The last row indicates the signal contribution in the bWN region, defined by the percentage of the number of signal events divided by the number of background events.

by the ratio of the total number of events in the signal yield over the total number of events in the background as: N_s/N_b. The values are taken from Figure 6.1 left, and the result expressed in Table 6.1 last row. The signal contamination will be calculated in the same way for all the regions, with this same mass point.

None	el	mu	total
$t\bar{t}$ 2L	11.42 ± 0.80	14.43 ± 1.21	25.84 ± 1.45
$t\bar{t}$ 1L1τ	17.23 ± 3.86	17.07 ± 1.57	34.29 ± 4.16
$t\bar{t}$ 1L	1.94 ± 0.53	0.73 ± 0.13	2.67 ± 0.55
W+jets	0.52 ± 0.16	0.90 ± 0.25	1.42 ± 0.30
Single top	0.60 ± 0.12	1.16 ± 0.26	1.76 ± 0.28
Diboson	0.65 ± 0.20	0.62 ± 0.19	1.28 ± 0.27
Z+jets	0.05 ± 0.04	0.00 ± 0.00	0.05 ± 0.04
$t\bar{t}$+V	0.64 ± 0.22	1.06 ± 0.72	1.70 ± 0.75
Total SM	31.04 ± 3.99	34.97 ± 2.15	66.01 ± 4.53
stop_bWN_350_200	25.06 ± 2.73	35.65 ± 5.62	60.71 ± 8.75
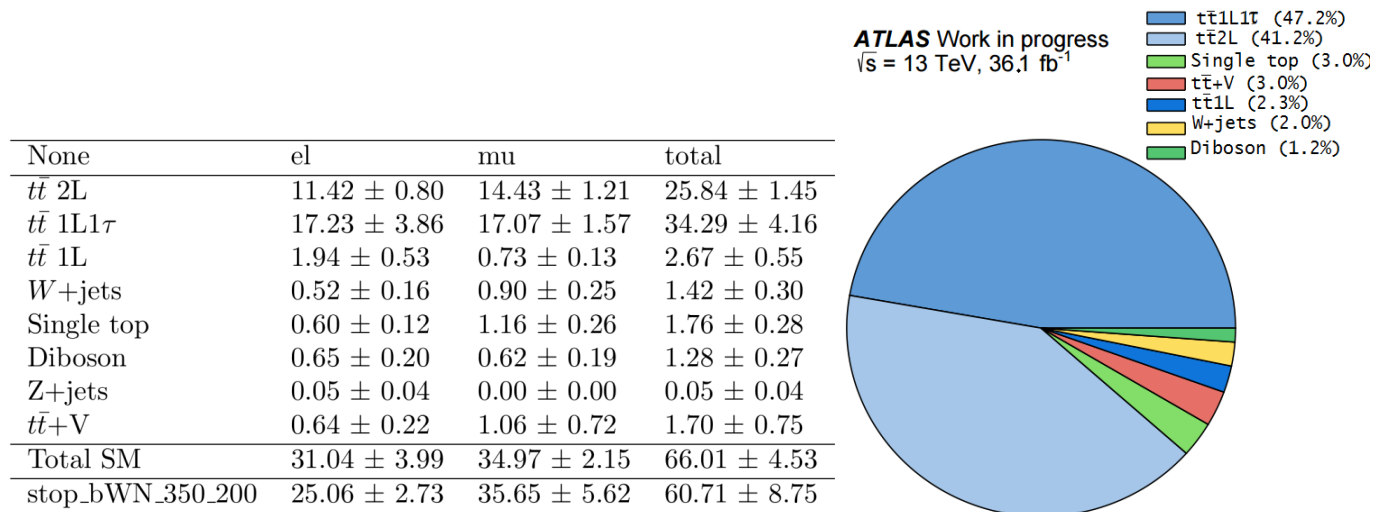
Figure 6.1 (left) Expected events in the **bWN** region, divided in electron (el), muon (mu) for 36.1 fb^{-1}. Only statistical uncertainty of MC samples are presented. stop_ bWN _ 350 _ 200 stands for the mass point m($\tilde{t}_1, \tilde{\chi}_1^0$) = (350,200). (right) Breakdown of the individual SM contributions to the signal region [87].

6.2 Control Regions

After the selection of the signal region in the previous section, it is clear that the background that dominates is dileptonic $t\bar{t}$, with either two (e/μ) charged leptons with one of them lost or miss-identified (2L), or one e or μ and one τ lepton (1L1τ). Therefore the current analysis decided to define only one CR, called the TCR, targeting only dileptonic

Variable	bWN	TCR
Leading jet p_T	> 50 GeV	> 50 GeV
jets 2,3,4 p_T	> 25 GeV	> 25 GeV
E_T^{miss}	>300 GeV	> 230 GeV
m_T	> 130 GeV	> 130 GeV
am_{T2}	< 110 GeV	$\in$[130,170] GeV
number of $b-$ jets	≥ 1	≥ 1
$\Delta\phi(\vec{p}_T^{miss}, l)$	< 2.5	>2.5
Signal Contamination		$\approx 11\%$

Table 6.2 Events selections defining bWN with the associated dileptonic $t\bar{t}$ control region (**TCR**). The event preselection (see Table 5.1) was applied in both cases [89].The last row indicates the signal contamination in the TCR region, defined by the percentage of the number of signal events from the mass point $m(\tilde{t}_1, \tilde{\chi}_1^0)$=(350,200) divided by the number of background events.

$t\bar{t}$ background.

In this thesis it will be shown that by implementing dedicated CRs for the other sub-leading backgrounds ($t\bar{t}$ 1L, W+jets and Single Top) an improvement in analysis is achieved.

6.2.1 Dileptonic CR

Dileptonic $t\bar{t}$ is the dominant background after the SR selection. The SM production is shown in the Feynman diagram of Figure 6.2, where in a top-antitop quark production, both W bosons decay leptonically. The dileptonic control region denoted as TCR is described in table 6.2 compared with the selection of the signal region bWN. The signal contamination in TCR is given in the last row and calculated for the mass point $m(\tilde{t}_1, \tilde{\chi}_1^0)$ = (350,200). am_{T2} selection is close to m_{top} because the $t\bar{t}$ events saturate around this value, so it is restricted to [130< am_{T2} <170 GeV]. The E_T^{miss} is loosened to gain statistics. After applying the m_T >130 GeV selection, the $\Delta\phi(\vec{p}_T^{miss}, l)$ distribution tends to have lower background as shown in Figure 6.3, so this variable cut is shifted for the TCR.
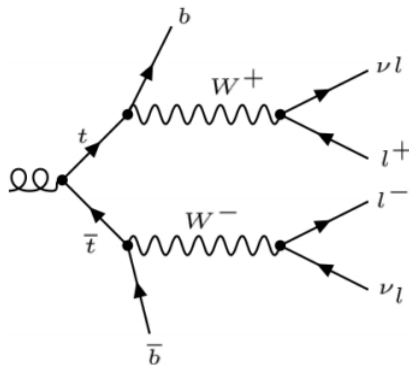
Figure 6.2 Feynman diagram showing the dileptonic $t\bar{t}$ decay channel [127].

In order to ensure a good modeling of the entire $\Delta\phi(E_T^{miss}, l)$ distribution, this variable was verified in a slightly different control region defined as TCR2, showing the entire

None	el	mu	total
$t\bar{t}$ 2L	71.62 ± 9.35	70.79 ± 8.12	142.41 ± 12.38
$t\bar{t}$ 1L1τ	82.53 ± 6.70	100.69 ± 20.28	183.22 ± 21.36
$t\bar{t}$ 1L	6.46 ± 3.64	1.32 ± 0.57	7.78 ± 3.68
W+jets	2.77 ± 1.36	3.93 ± 1.51	6.70 ± 2.03
Single top	9.27 ± 6.57	8.06 ± 3.29	17.33 ± 7.35
Diboson	3.02 ± 1.09	1.22 ± 0.35	4.25 ± 1.15
Z+jets	0.91 ± 0.37	0.06 ± 0.04	0.97 ± 0.37
$t\bar{t}$+V	4.51 ± 0.67	4.87 ± 0.90	9.38 ± 1.13
Total SM	181.10 ± 13.86	190.95 ± 22.17	372.05 ± 26.15
stop_bWN_350_200	13.23 ± 3.27	21.99 ± 6.93	35.21 ± 7.66
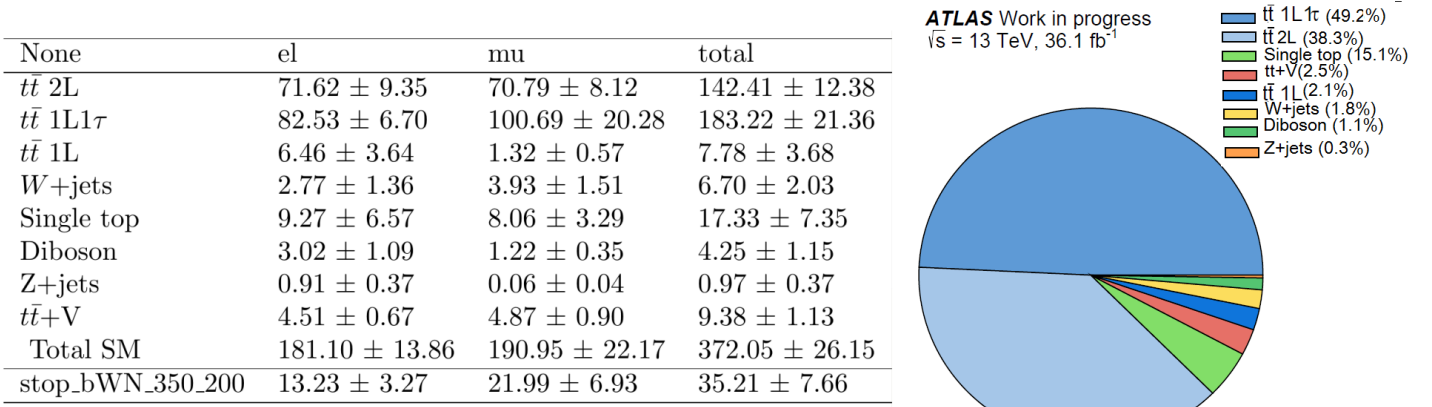
Figure 6.3 The yields table of the **TCR** selection criteria for 36.1fb^{-1}. Only the statistical uncertainty of the MC is given (left). Pie chart of the individual SM contributions (right).[87]

$\Delta\phi(E_T^{miss}, l)$ plane as shown in Figure 6.4 (left). In the TCR2 phase space selection the cut on $\Delta\phi(E_T^{miss}, l)$ is omitted and an extra cut on the leading $b-$jet $p_T >$120 GeV is required, shown in Table 6.3. The signal contamination for the mass point m($\tilde{t}_1, \tilde{\chi}_1^0$)=(350,200) is calculated and given in the last row of Table 6.3. As the two sub-backgrounds of the dileptonic $t\bar{t}$ (2L and 1L1τ) are determined together, their kinematical characteristics needed to be checked. The shape plot of $\Delta\phi(E_T^{miss}, l)$ is shown in Figure 6.4 (right), demonstrating that in fact, both sub-backgrounds are very similar in kinematic shape and can be defined as one single background.

Figure 6.5 shows the kinematic distributions of the variables used in the selection, the cut on the dedicated quantity is omitted[1]. A reasonable agreement between data and simulation is found. The statistical uncertainties are shown as the grey lines in the distribution, and as the grey solid parts in the ratio plots.
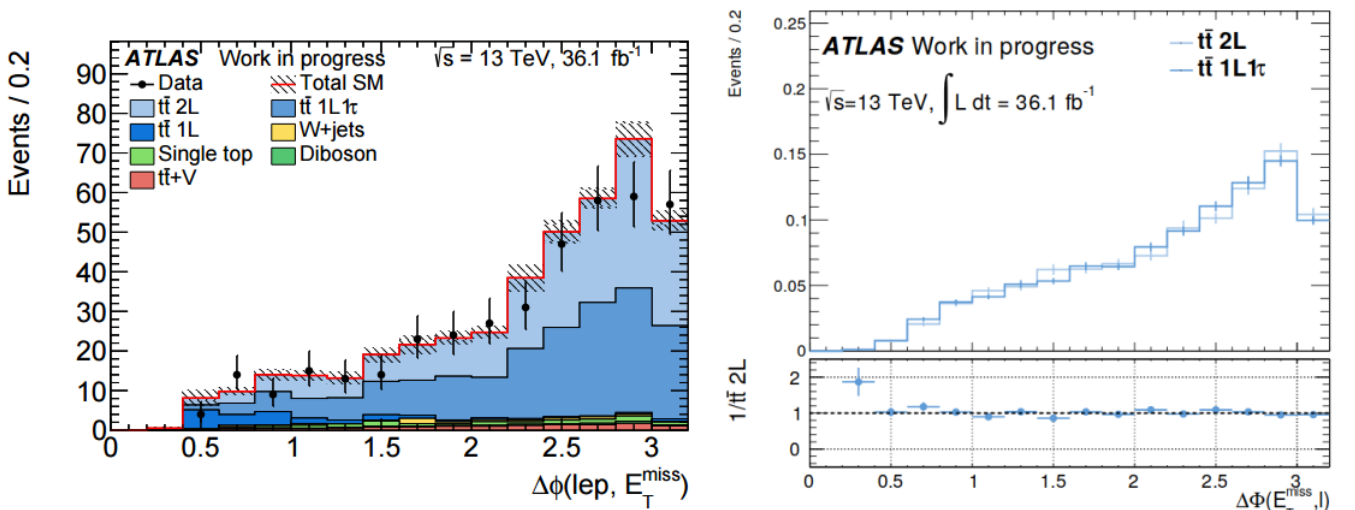
Figure 6.4 (Left) The entire $\Delta\phi(E_T^{miss}, l)$ distribution defined in the **TCR2** (left) showing a good agreement of data and MC. (Right) A shape comparison between the two sub-background (2L and 1L1τ) of dileptonic $t\bar{t}$ background showing a similarity in shape kinematics.

---

[1]This omission in the cut of the plotted quantity is usually referred as n-1 plots.

| Variable	TCR	TCR2
Leading jet p_T	> 50 GeV	> 50 GeV
jets 2,3,4 p_T	> 25 GeV	> 25 GeV
E_T^{miss}	>230 GeV	> 230 GeV
m_T	> 130 GeV	> 130 GeV
am_{T2}	$\in$[130,170] GeV	$\in$[130,170] GeV
number of $b-$ jets	≥ 1	≥ 1
$\Delta\phi(\vec{p}_T^{miss}, l)$	> 2.5	—
$b-$jet p_T	—	>120GeV
Signal Contamination		$\approx 4\%$

Table 6.3 Events selections defining **TCR2** compared with TCR. The event preselection was applied in both cases [89].The last row indicates the signal contamination in the TCR2 region.

Variable	bWN	TCR1L
Leading jet p_T	> 50 GeV	> 50 GeV
jets 2,3,4 p_T	> 25 GeV	> 25 GeV
E_T^{miss}	>300 GeV	> 230 GeV
m_T	> 130 GeV	$\in$[60,90] GeV
am_{T2}	< 110 GeV	$\in$[130,170] GeV
number of $b-$ jets	≥ 1	≥ 1
$\Delta\phi(\vec{p}_T^{miss}, l)$	< 2.5	—
$b-$jet p_T	—	>120 GeV
Signal Contamination		$\approx 0.4\%$

Table 6.4 Events selections defining the **TCR1L** control region and comparing it with the signal region bWN. The event preselection was applied in both cases. The signal contamination in the TCR1L is mentioned.

6.2.2 Semileptonic CR

The semileptonic $t\bar{t}$ background is one of the sub-leading backgrounds for the 3-body decay. The schematic example of the $t\bar{t}$ semileptonic decay is shown in Feynman diagram Figure 6.6, where one of the W bosons coming from the top pair production, decays leptonically and the other hadronically. One of the main variables to define different CRs is the m_T variable. From Figure 5.3 where the distributions after the 3-body preselection were presented, we can appreciate that the backgrounds drop sharply after the mass of the W boson. The signal events can exceed this kinematic endpoint due to the two additional LSPs in the event. By modifying the m_T selection to be a window whose upper edge is near the W boson mass, we can define the different CRs. For the $t\bar{t}$ semileptonic CR (TCR1L) m_T is selected as 60$\leq m_T \leq$90 GeV. A requirement on the leading $b-$jet p_T >120 GeV is required, because in the semileptonic $t\bar{t}$ events the $b-$jet comes from an on-shell top quark. The selection is shown in Table 6.4 comparing it to the signal region bWN.

The pie chart showing the different contributions of the SM backgrounds is shown in Figure 6.7 (right). The contribution of $t\bar{t}$ 1L events is above 80 % in this selection (left). The kinematic distribution of the variables as n-1 plots is shown in Figure 6.8 for the TCR1L selection. A reasonable agreement between data and simulation is also found.
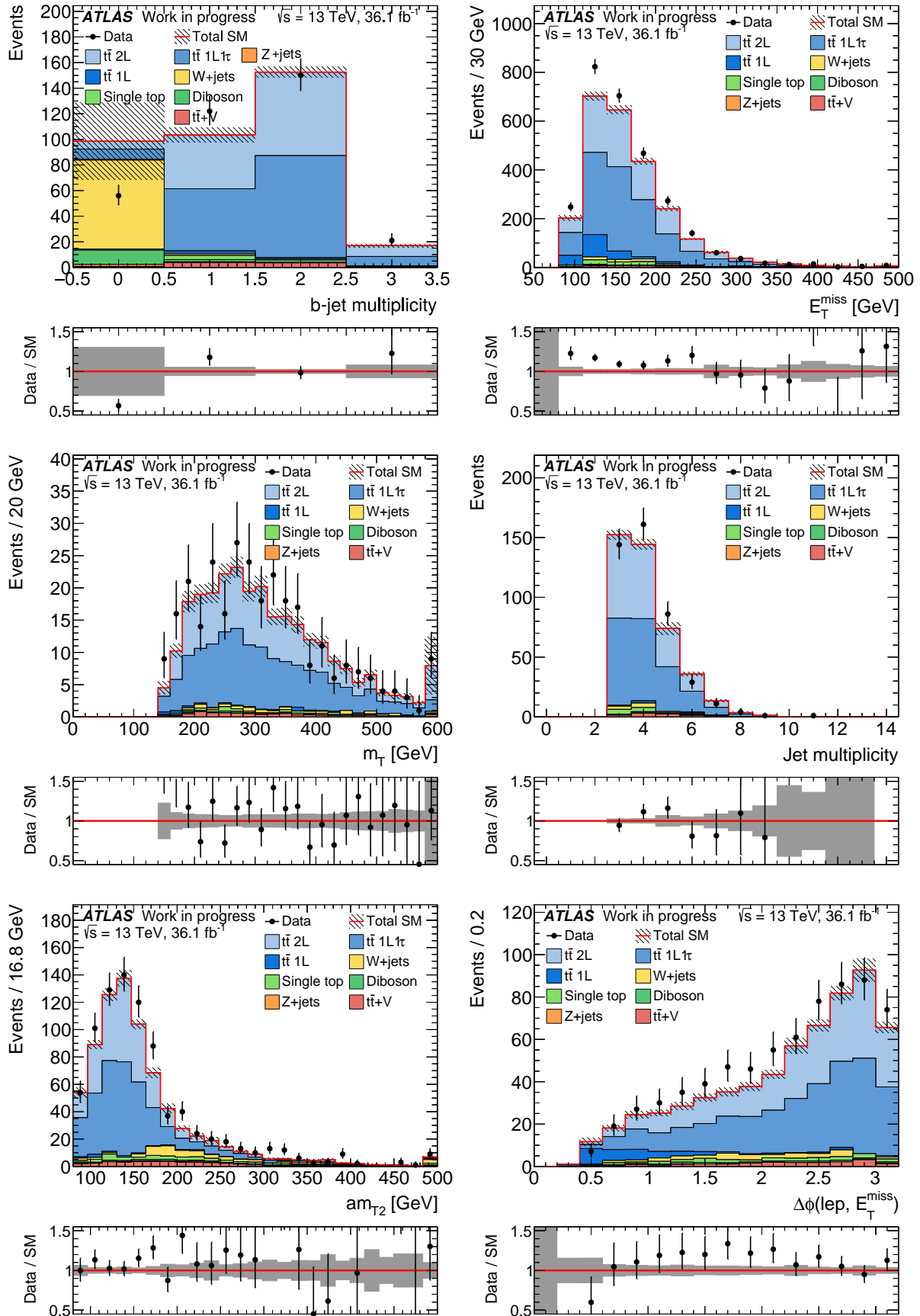
Figure 6.5 Comparison of data and simulation for the dileptonic $t\bar{t}$ CR (**TCR**) before applying the normalization of the simultaneous fit in the n-1 plots. Only statistical uncertainties are displayed. The last bin includes the overflow.
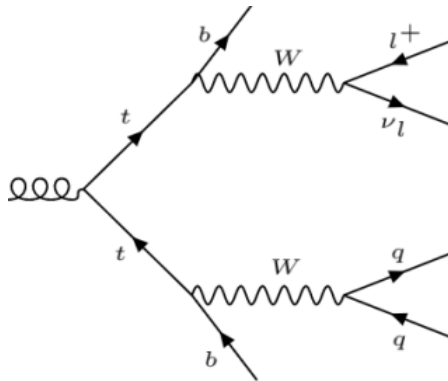
Figure 6.6 Feynman diagram of the $t\bar{t}$ semileptonic decay [127].

None	el	mu	total
$t\bar{t}$ 2L	13.61 ± 2.52	10.73 ± 0.95	24.34 ± 2.69
$t\bar{t}$ 1L1τ	16.30 ± 1.54	14.86 ± 1.74	31.16 ± 2.33
$t\bar{t}$ 1L	861.38 ± 22.59	894.82 ± 27.84	1756.21 ± 35.85
W+jets	70.32 ± 12.14	50.75 ± 5.20	121.07 ± 13.20
Single top	75.53 ± 22.64	92.28 ± 18.65	167.81 ± 29.33
Diboson	5.33 ± 3.07	3.23 ± 0.63	8.56 ± 3.13
Z+jets	0.05 ± 0.03	0.45 ± 0.18	0.50 ± 0.18
$t\bar{t}$+V	7.31 ± 0.85	6.43 ± 1.30	13.74 ± 1.55
Total SM	1049.83 ± 34.48	1073.54 ± 34.00	2123.37 ± 48.42
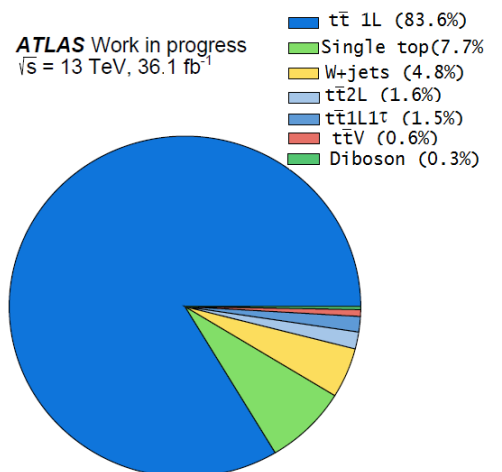
Figure 6.7 (Right) Number of events expected in TCR1L for 36.1 fb^{-1}. Only statistical uncertainty of the MC sample given. (Left) Breakdown of the individual SM contributions to the TCR1L region.
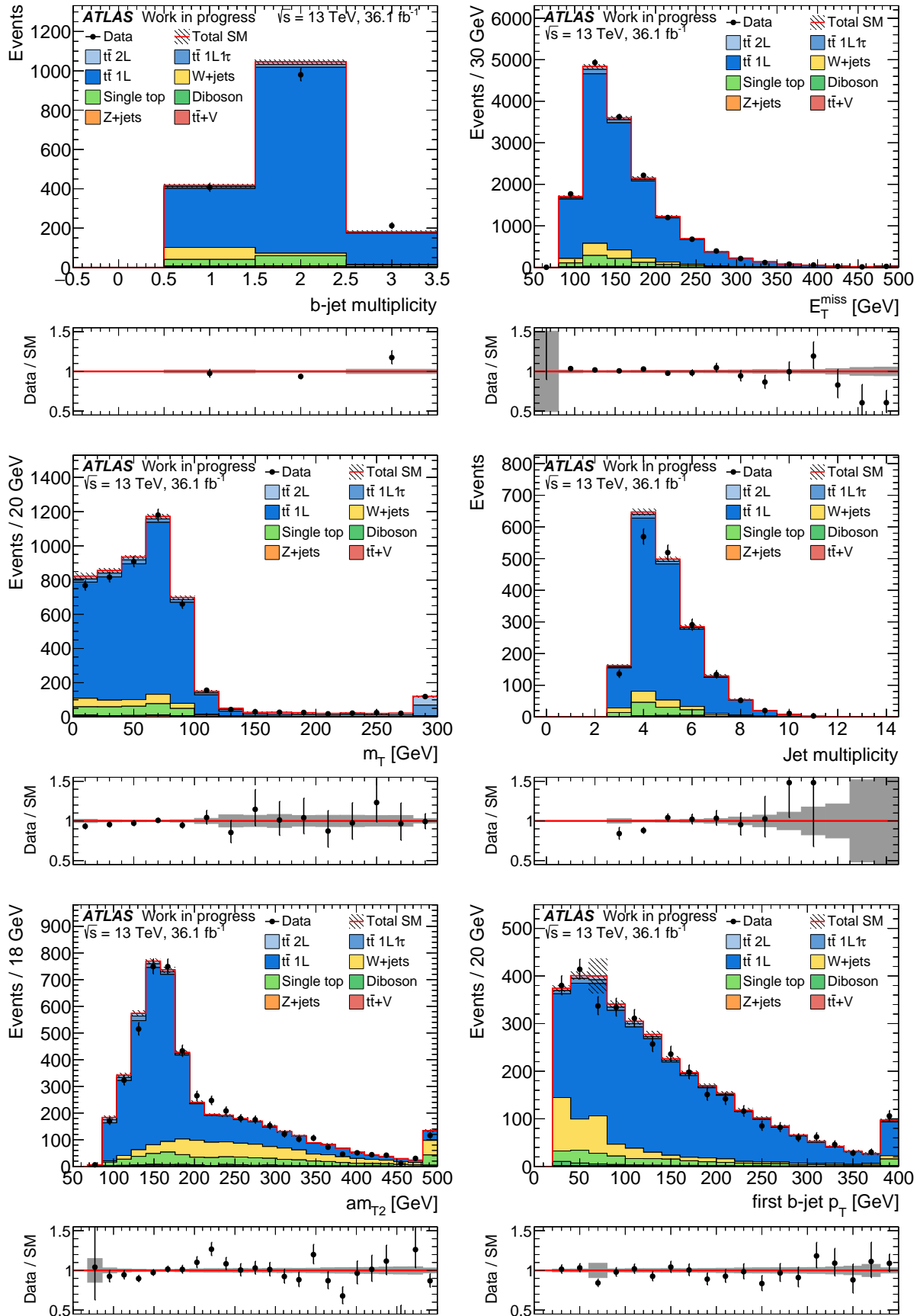
Figure 6.8 Comparison of data and simulation for the semileptonic $t\bar{t}$ CR (**TCR1L**) before applying the normalization of the simultaneous fit as n-1 plots. Only statistical uncertainties are displayed. The last bin includes the overflow.

Variable	bWN	WCR
Leading jet p_T	> 50 GeV	> 50 GeV
jets 2,3,4 p_T	> 25 GeV	> 25 GeV
E_T^{miss}	>300 GeV	> 230 GeV
m_T	> 130 GeV	$\in[30,90]$ GeV
am_{T2}	< 110 GeV	$\in[130,170]$ GeV
number of $b-$ jets	≥ 1	$= 0$
$\Delta\phi(\vec{p}_T^{miss}, l)$	< 2.5	—
$b-$jet p_T	—	—
Signal Contamination		$\approx 0.16\%$

Table 6.5 Events selections the **WCR** control region compared with the bWN signal region. The event preselection was applied in both cases. The signal contamination in the WCR is shown in the las row.

6.2.3 W+jets

Another sub-leading background is the production of W+jets as sketched in Figure 6.9. The dedicated W+jets control region (WCR) requires a $b-$jet veto that enriches the W+jets production as we can appreciate in the Feynman diagram, as relaxing the m_T cut too. The $b-$jet veto suppresses $t\bar{t}$ events and results in a W+jets purity of about 80% as shown in Figure 6.10 (left). In the WCR the $b-$tag veto predominantly select light-flavor W+jets events.
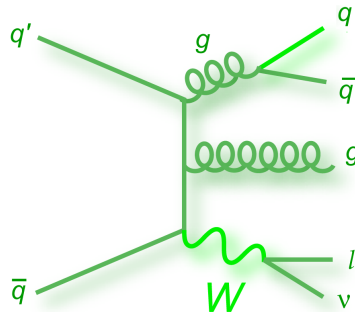
Figure 6.9 Feynman diagram of the $W+$ jets decay channel with a $b-$jet veto required[133].

The WCR selection criteria are described in Table 6.5 in comparison with the bWN, and the n-1 plots distributions of the selected variables in Figure 6.11 are presented. The shape in the n-1 plots is reasonably well described, but a normalization factor is scaling the data points only up to the W+jets events.

6.2.4 Single Top CR

The last of our studied sub-backgrounds is the single top CR (STCR) in the Wt channel as shown in the Feynman diagram of Figure 6.12. This process can evade kinematic bounds from selections targeting the suppression of $t\bar{t}$. Nonetheless, isolating a pure sample of Wt events kinematically close to the SR is challenging due to the similarity of Wt and $t\bar{t}$. The Wt events that pass event selections similar to those for the SR often have a second $b-$jet within the acceptance.

None	el	mu	total
$t\bar{t}$ 2L	5.56 ± 0.72	5.55 ± 0.95	11.11 ± 1.19
$t\bar{t}$ 1L1τ	9.16 ± 3.37	7.18 ± 1.16	16.33 ± 3.56
$t\bar{t}$ 1L	245.42 ± 12.57	245.24 ± 19.31	490.66 ± 23.04
W+jets	1937.30 ± 64.35	1928.33 ± 58.23	3865.62 ± 86.78
Single top	33.13 ± 3.88	36.50 ± 3.98	69.63 ± 5.56
Diboson	80.81 ± 6.76	91.49 ± 11.69	172.29 ± 13.50
Z+jets	2.92 ± 0.68	13.08 ± 3.68	16.00 ± 3.74
$t\bar{t}$+V	1.94 ± 0.41	-0.33 ± 1.17	1.62 ± 1.24
Total SM	2316.22 ± 66.12	2327.04 ± 62.71	4643.26 ± 91.13
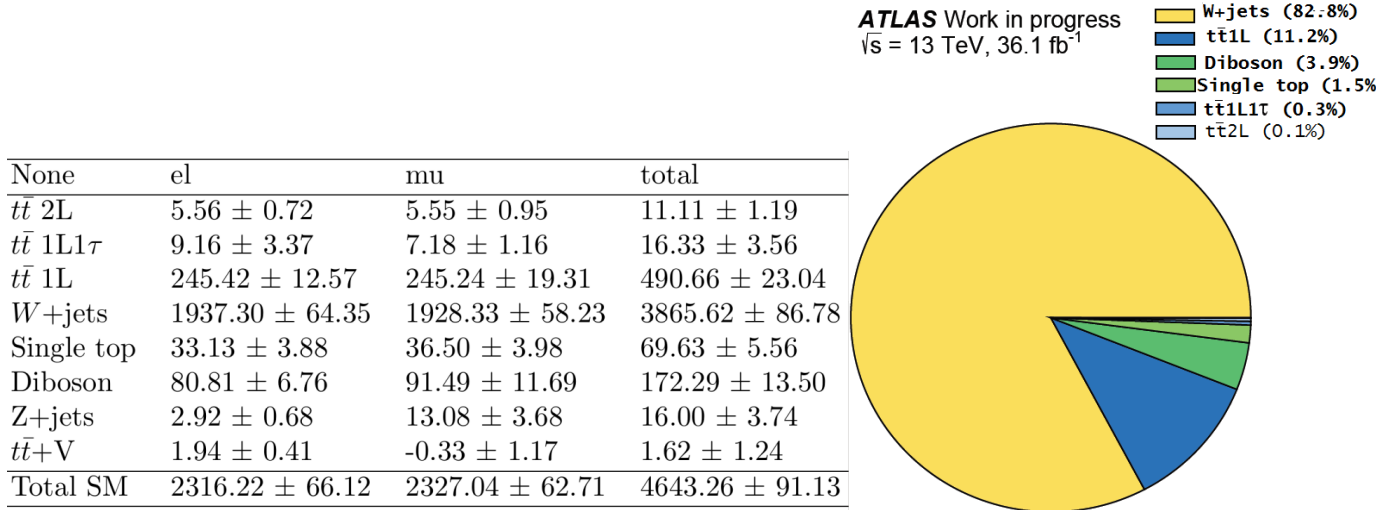
Figure 6.10 Number of events expected in **WCR** for 36.1 fb^{-1}. Only statistical uncertainty of the MC sample given (left). Breakdown of the individual SM contributions to the WCR region (right).
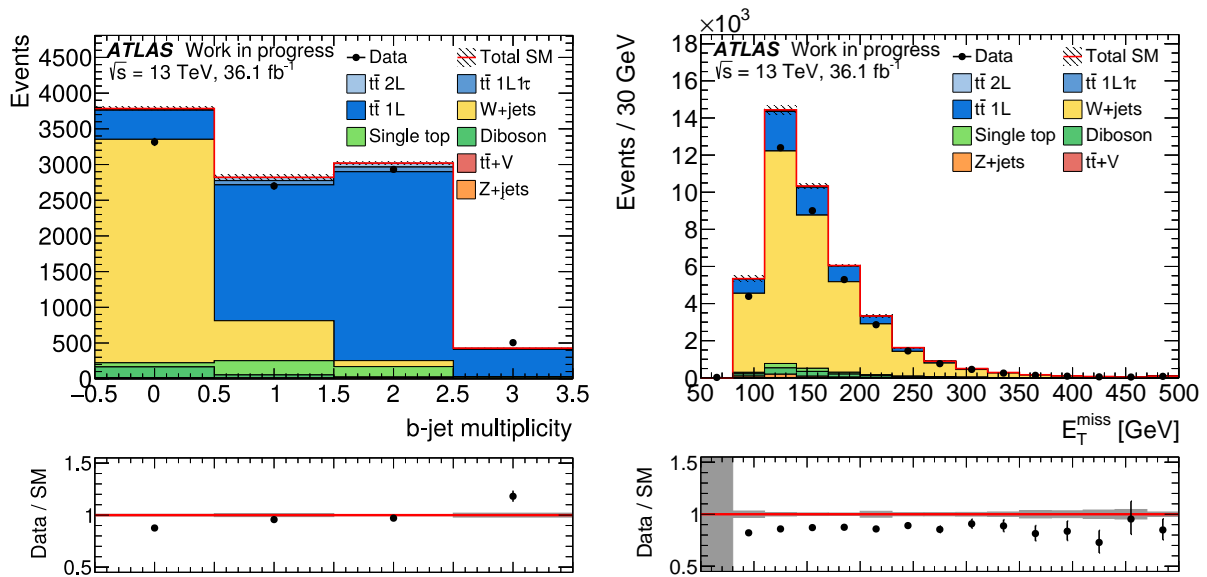
Figure 6.11 Comparison of data and simulation for the W+jets CR (**WCR**) before applying the normalization of the simultaneous fit represented in n-1 plots. Only statistical uncertainties are displayed. The last bin includes the overflow.
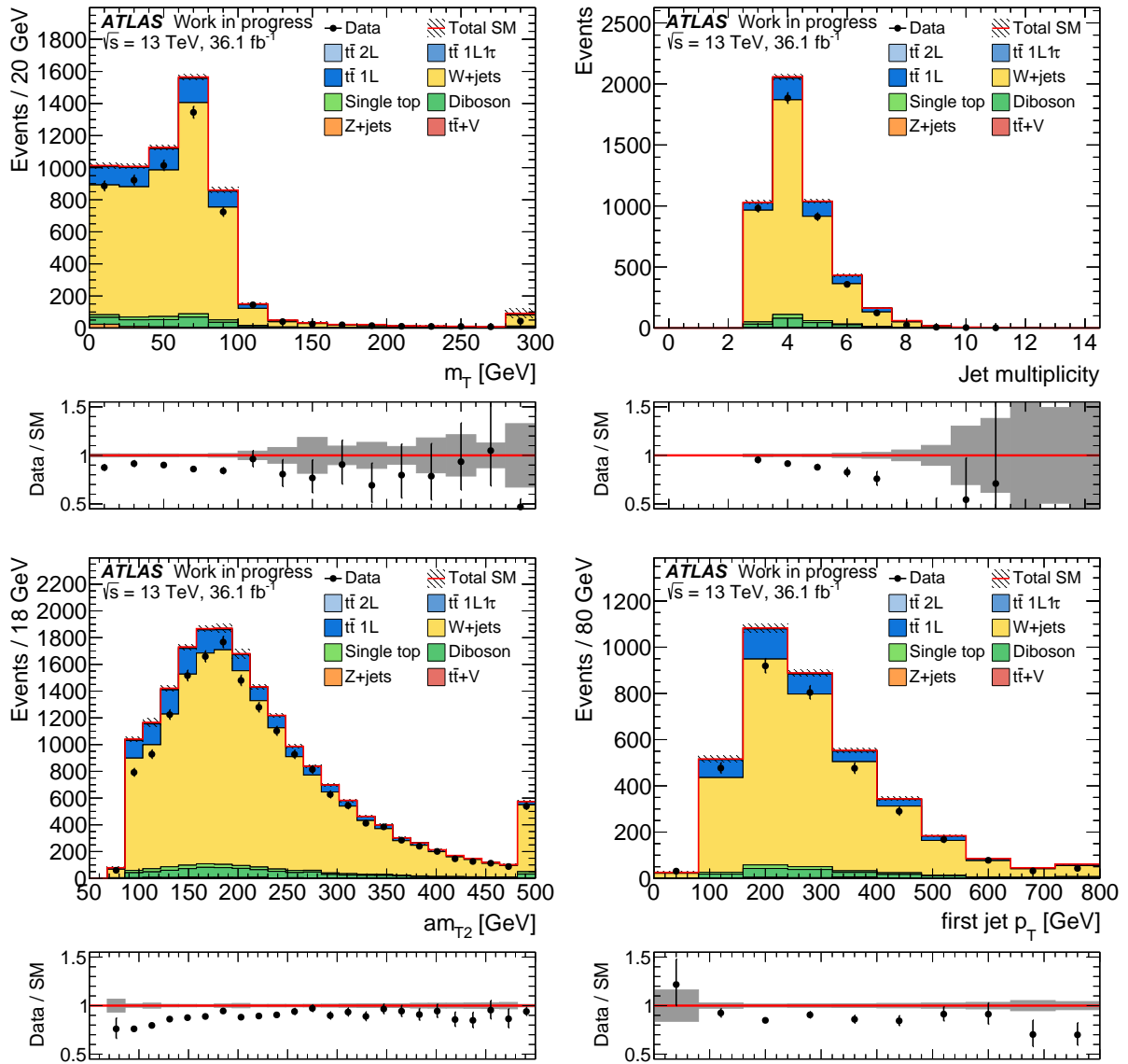
Figure 6.11 Comparison of data and simulation for the W+jets CR (WCR) before applying the normalization of the simultaneous fit represented in n-1 plots. Only statistical uncertainties are displayed. The last bin includes the overflow.

The am_{T2} variable is useful for discriminating between $t\bar{t}$ and Wt because the mass of the Wb system not from the resonant top quark is typically higher than from an on-shell top quark in the phase space selected by this analysis. Therefore, the STCR is characterized by $am_{T2} >$200 GeV. Furthermore, to increase the purity of Wt and reduce the $W+$jets contamination, events are required to have two $b-$tagged jets. Top quark pair events can exceed the am_{T2} kinematic bound when one of the two $b-$tags used in the am_{T2} calculation is a jet produced from a charm quark from the W decay [89][131]. When this jet is from the same top quark as the other $b-$tagged jet, the ΔR(b_1, b_2) between them tends to be smaller than for Wt events. They have two $b-$jets from $b-$quarks that are naturally well separated. Therefore, to further increase the Wt purity, events in the STCR are required to have $\Delta R(b_1, b_2) >$1.5. with b_1, b_2 the highest p_T $b-$tag jets.

Another new variable introduced, in order to get a single top purity of $\sim$60% as shown in Figure 6.13 right, is *topness* as explained in more detail section 5.3. This variable suppresses partially reconstructed $t\bar{t}$ events [130]. At values $>$10 in *topness*, the distribution and shape of this variable gain more single top events, rejecting $t\bar{t}$ as appreciated in Figure 6.14, showing a separation between the $t\bar{t}$ backgrounds. The selection is listed in Table 6.6 and the contribution of the SM background in Figure 6.13. The kinematic distributions of the variables used in the selection are shown in Figure 6.14 as n-1 plots. Further studies are needed to understand the apparent slope that the data forms in th m_T and am_{T2} variables, and check if they are within systematics. In general we have less MC events for this region, but the kinematic variables still show a considerable well modeled distribution.
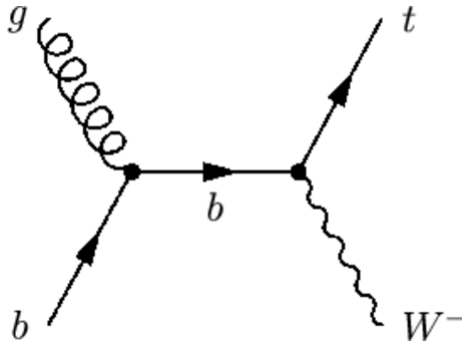
Figure 6.12 Feynman diagram representing the single top production via the Wt chanel [134].

Variable	bWN	STCR
Leading jet p_T	> 50 GeV	> 50 GeV
jets 2,3,4 p_T	> 25 GeV	> 25 GeV
E_T^{miss}	>300 GeV	> 230 GeV
m_T	> 130 GeV	$\in$[30,90] GeV
am_{T2}	< 110 GeV	> 200 GeV
number of $b-$ jets	≥ 1	= 2
$\Delta\phi(\vec{p}_T^{miss}, l)$	< 2.5	—
$b-$jet p_T	—	> 160 GeV
topness	—	> 10
$\Delta R(b_1, b_2)$	—	> 1.5
Signal Contamination		$\approx 0.16\%$

Table 6.6 Event selection in the **STCR** control region compared to the bWN signal region. The event preselection was applied in both cases. The signal contamination in the STCR is mentioned.

None	el	mu	total
$t\bar{t}$ 2L	0.77 ± 0.18	0.89 ± 0.23	1.66 ± 0.30
$t\bar{t}$ 1L1τ	1.06 ± 0.16	2.41 ± 0.67	3.47 ± 0.69
$t\bar{t}$ 1L	47.59 ± 4.65	28.65 ± 6.77	76.24 ± 8.21
W+jets	53.80 ± 6.08	58.79 ± 4.75	112.59 ± 7.71
Single top	101.81 ± 5.84	107.34 ± 13.65	209.14 ± 14.85
Diboson	1.84 ± 0.49	3.59 ± 1.67	5.42 ± 1.74
Z+jets	0.08 ± 0.03	0.21 ± 0.19	0.29 ± 0.20
$t\bar{t}$+V	2.92 ± 0.54	1.77 ± 0.58	4.69 ± 0.79
Total SM	209.86 ± 9.66	203.63 ± 16.07	413.50 ± 18.75

ATLAS Work in progress
$\sqrt{s}$ = 13 TeV, 36.1 fb^{-1}

- Single top (63.2%
- W+jets (17.6%)
- $t\bar{t}$1L (16.5%)
- $t\bar{t}$1L1τ (1.0%)
- tt+V (0.8%)
- Diboson (0.5 %)

Figure 6.13 Number of events expected in **STCR** for 36.1 fb^{-1}. Only statistical uncertainty of the MC sample given (left). Breakdown of the individual SM contributions to the STCR region (right).
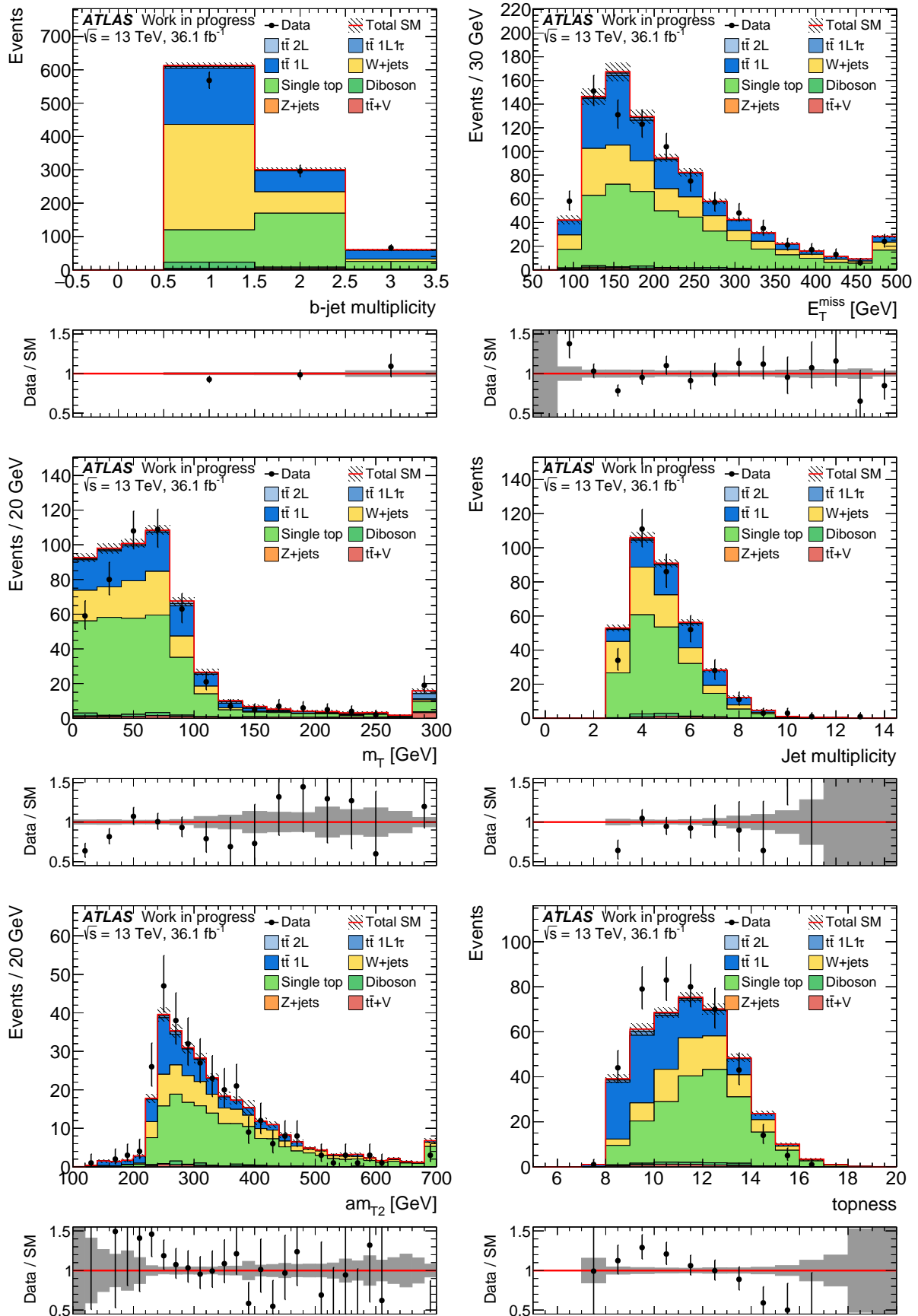
Figure 6.14 Comparison of data and simulation for the single top CR (**STCR**) before applying the normalization of the simultaneous fit. Only statistical uncertainties are displayed. The last bin includes the overflow.
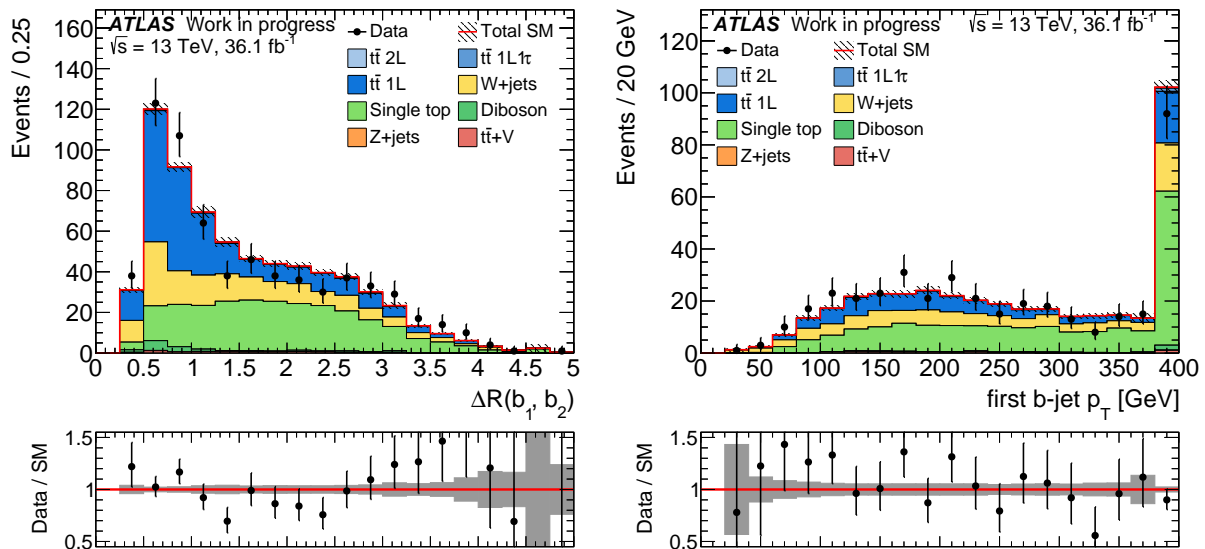
Figure 6.14 Comparison of data and simulation for the single top CR (STCR) before applying the normalization of the simultaneous fit. Only statistical uncertainties are displayed. The last bin includes the overflow.

6.3 Validation Regions

The background estimates are tested using validation regions (VR), which are disjoint to both the control and signal regions. Background normalizations determined in the control regions are extrapolated to the VRs and compared with the observed data. The validation regions are used to provide a statistically independent test of the background estimates made using the CRs.

The VRs are designed to be kinematically close to the associated SR to test the background estimates in regions of phase space as similar as possible to the SR. For most analyses the associated VRs are defined following a similar strategy as used for the CRs but with a different am_{T2} requirement, which leads to a set of events orthogonal to both the associated CRs and the SR. The event selections for the $t\bar{t}$2L, $t\bar{t}$1L, W+jets and single top VRs, TVR, TVR1L, WVR and STVR respectively, are given in table 6.7 compared with the SR. The SM contribution of the main background is shown for every VR and the signal contamination is calculated. A diagram shown in Figure 6.15, indicate the kinematic boundaries.

A histogram showing the total number of events per signal, control and validation regions is presented in Figure 6.16, for the nominal predicted samples.

6.4 Systematic Uncertainties

An important point in the background estimation is to know how accurate the results are. We can have statistical fluctuations as swell as ystematic uncertainties that can increase the uncertainty in the result.

The systematic uncertainties are evaluated for all background and signal samples, using MC simulations. Since the yields from the dominant background sources, $t\bar{t}$, W+jets and single top, are obtained in dedicated control regions, the modeling of uncertainties for

Variable	bWN	TVR	T1LVR	WVR	STVR
E_T^{miss} [GeV]	>300	> 300	> 300	> 300	> 300
m_T [GeV]	> 130	> 130	[60,90]	[30,90]	[30,90]
am_{T2} [GeV]	< 110	[110,130]	[110,130]	[110,130]	>200
number of $b-$ jets	≥ 1	≥ 1	≥ 1	$= 0$	$= 2$
$\Delta\phi(\vec{p}_T^{miss}, l)$	< 2.5	> 2.5	—	—	—
Purity of leading bkg $\sim$		89%	75%	83%	52%
Signal contamination $\sim$		7%	1.7%	0.2%	0.02%

Table 6.7 Events selections defining the bWN signal region with the associated validation regions for dileptonic $t\bar{t}$, semileptonic $t\bar{t}$, W+jets and single top (TVR, T1LVR, WVR and STVR respectively). The event preselection as in Table 5.1 was applied in all cases. The percentage of the SM contribution for the leading background is given for each validation region as the signal contamination.
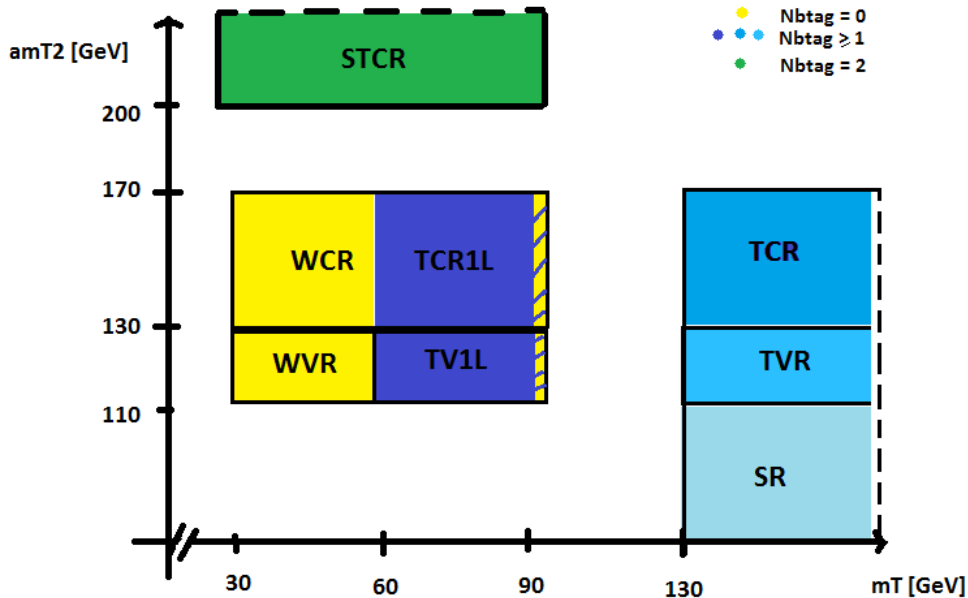
Figure 6.15. Schematic diagram for various event selections used to estimate and validate the background model and then search for the stop production. It is represented in the phase space of the two main discriminating variables: m_T and am_{T2}. Dashed lines indicate events that are extended beyond the boundary. SR, CR and VR stands for signal region, control region and validation region respectively. T, T1L, W, ST stands for $t\bar{t}$2L, $t\bar{t}$1L, W+jets and single top.
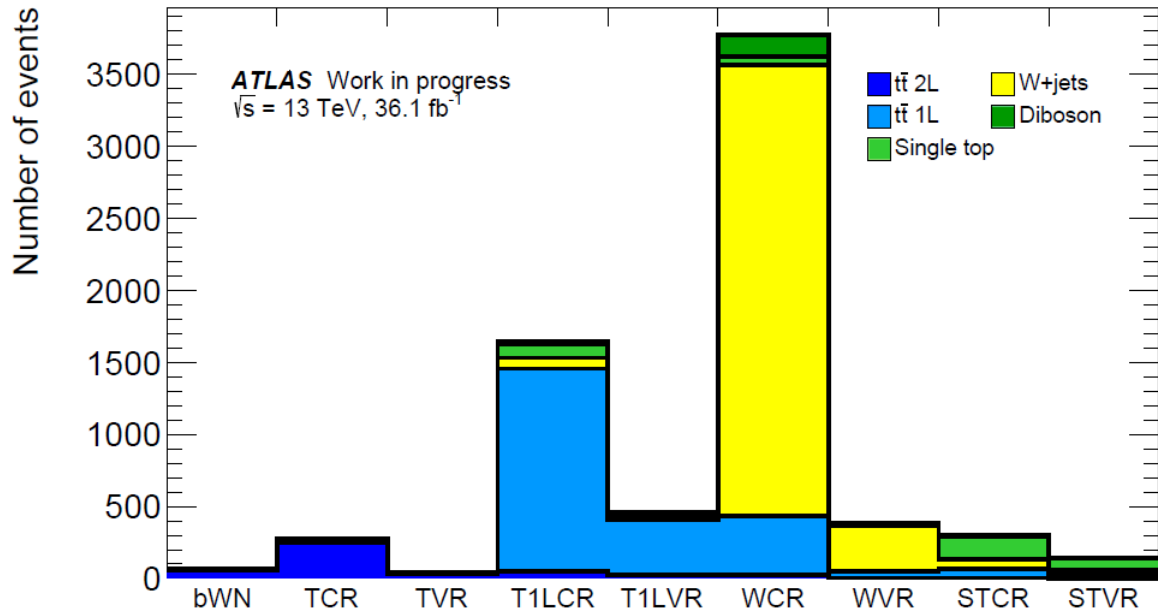
Figure 6.16 Histogram showing in every bin the total number of events of the nom-
inal samples per defined regions: signal region (SR), dileptonic control region (TCR),
dileptonic validation region (TVR), semileptonic control region (TCR1L), semileptonic
validation region (TVR1L), W+jets control region (WCR), W+jets validation region
(WVR), single top control region (STCR) and single top validation region (STVR).

these processes affect only the extrapolation from the CRs into the SR, but not the
overall normalization.

There are two types of systematic uncertainties: uncertainties due to theoretical pre-
dictions and modeling (theoretical uncertainties), and uncertainties stemming from ex-
perimental effect (experimental uncertainties).

6.4.1 Experimental Systematic Uncertainties

The main experimental uncertainties arise from the calibration of the jet energy (JES)
[135] and the measurement of the jet energy resolution (JER) [136]. The total uncertainty
from the JER, and the jet mass scale and resolution on the large-R jets is obtained from
both data and MC simulations [137]. The uncertainty from the $b-$tagging efficiency
is estimated by varying the efficiency correction factors for b and c jets and the miss-
tag rate correction factors which are measured in $t\bar{t}$ and dijet events [138][139]. The
other experimental uncertainties originate from the modeling of the average number of
interactions per bunch crossing, the modeling of the contribution to the E_T^{miss} from energy
deposits which are not associated to reconstructed objects or arise from pileup effects,
the modeling of the trigger, identification efficiency, energy and momentum scale and
resolution, isolation and τ-veto, and the uncertainty on the integrated luminosity.

6.4.2 Theoretical Systemic Uncertainties

Since the yields for the dominant background sources, $t\bar{t}$, W+jets and single top are ob-
tained in dedicated control regions, the modeling uncertainties for these processes affect
only the extrapolation from the CRs into the signal region but not the overall normaliza-
tion.

They are given by the generator modeling, parton distribution function choice and parton shower uncertainties. In the following the different theoretical systematic uncertainties will be explained for each background.

6.4.2.I Transfer Factor Method

Many observables are chosen, as described in 6.2 section, to separate between regions. To extract accurate information from the data, a probability density function (PDF) is used whose parameters are used in the fitting procedure. The fit performed to data is based on statistically independent CRs and SR.

One of the key ingredients to the fit procedure are the ratios of the event counts, called *transfer factors* (TF), of each normalized background between the SR and CRs. It is defined as the ratio of the yields. As an example for the TCR region, we can compute something like: $\text{TF} = y_{SR}/y_{TCR}$, y_{WCR}/y_{TCR}, y_{STCR}/y_{TCR}, y denoting the total number of yields in each region of the suffix. We calculate this for the nominal (TF_{nom}) and the systematic (TF_{syst}) samples[2]. And the double ratio (u) gives us the desired systematics uncertainties:

$$u = \frac{(TF_{syst} - TF_{nom})}{TF_{nom}} \tag{6.1}$$

Then they are all added in quadrature as $((TF_{syst1} - TF_{nom})/TF_{nom})^2 + ((TF_{syst2} - TF_{nom})/TF_{nom})^2 + ...$

The great advantage of this method is that by choosing more kinematically similar CRs to the SR, a greater cancellation in the systematic uncertainties is obtained in the extrapolation, as seen in the ratio from equation 6.1 from MC estimates [132].

The statistical uncertainties (σ) are calculated as usual:

$$\sigma_{TF} = TF \cdot \sqrt{(\frac{\sigma_{SR}}{y_{SR}})^2 + (\frac{\sigma_{CR}}{y_{CR}})^2} \tag{6.2}$$

Where the y stands for the event yield of the region. So for the double ratio u they are defined as:

$$\sigma_u = \frac{TF'}{TF} \cdot \sqrt{(\frac{\sigma_{TF'}}{TF'})^2 + (\frac{\sigma_{TF}}{TF})^2} \tag{6.3}$$

And in equation 6.3, TF' denotes the transfer factor of the systematic sample and TF the one of the nominal sample.

6.4.2.II Variable by Variable Approach

When the theory uncertainties are limited due to the available statistics for alternative samples, a method called variable by variable (VBV) is used. It "boost" the statistics by:

1. When defining the regions (SR, TCR, TVR1L..), the number of events is taken separately for each main kinematic variable defined in the SR. So the preselection is taken

---

[2]The nominal samples are the ones we used for the analysis and are described in Table 4.1. The systematic samples are different for each background and will be explain in more detail in the following section.

into account plus the cut of only one main kinematic variable. In our case they are am_{T2}, m_T, E_T^{miss}, number of $b-$jets, and $\Delta\phi(\vec{p}_T^{\,miss}, l)$.

2. Then the TFs are computed for one variable at a time, i.e.: $TF_{m_T} = SR_{m_T}/TCR_{m_T}$.

3. They are added variable by variable in quadrature for each systematic source. By this the uncertainty associated to each variable is then summed in quadrature to obtain the total uncertainty estimate.

$$u_{total} = \sqrt{\sum_i^{variable} u_i^2} \tag{6.4}$$

$$\sigma_{u_{total}} = \frac{1}{\sum_i^{variable} u_i^2} \cdot \sum_i^{variable} u_i^2 \cdot \sigma_{u_i}^2 \tag{6.5}$$

The disadvantage of this method is that by boosting our statistics, we are not completely sure if this gives the correct uncertainty numbers, nevertheless it gives better results. In the following section the systematic samples used in this analysis will be described.

6.4.2.III $t\bar{t}$

The selection of samples evaluate three main effects [89]:

- **MC generator/ hard scatter:** The MC generator uncertainty is estimated by comparing events with POWHEG+HERWIG++ (referred as hpp _ ttbar and taken as the nominal sample for the comparison) and aMC@NLO+HERWIG++ (referred as amcatnlo_ ttbar and taken as the systematic sample).

- **Fragmentation/ hadronization (Had/Frag):** Events generated with POWHEG are hadronized with either PYTHIA6 (referred as powheg_ ttbar and taken as the nominal sample) or HERWIG++ (referred as hpp_ ttbar and taken as the systematic sample) to estimate the effect from modeling of the fragmentation and hadronization.

- **Additional Radiation:** The impact on altering the amount of initial- and final-state radiation is estimated from comparisons of POWHEG+PYTHIA samples with different parton shower radiation, NLO radiation, and modified factorization an renormalization scales. A variation to the lower limit of the radiation, called radiation low (radLo), and a variation in the upper limit, radiation high (radHi) is taken.

The results of such calculations can be appreciated in Table 6.8 by TF method and in Table 6.9 by VBV approach for the extrapolation of the TCR to the SR and the rest of the CRs and VRs. It is appreciated that by the VBV approach the numbers, especially the statistical uncertainties, have smaller results. By the TF method the statistical uncertainties are so large that the results are not trustful.

After several investigations, we found out that not separating the samples in either single leptonic or dileptonic in this analysis gives better results in the uncertainties, so we will take the whole $t\bar{t}$ sample, instead of splitting it in single- and di-leptonic, for the fit.

A generalization for calculating the theoretical systematic uncertainties, based on equation 6.1, but only taking the the number of events (n) can be expressed as:

Theory uncertainties on ttbar [%]							
	bWN	TVR	T1LCR	WCR	STCR	T1LVR	WVR	STVR
Radiation	19.72±2.82	1.82±4.18	18.5±3.67	18.41±5.16	12.83±9.0	10.44±10.87	37.09±5.17	16.16±11.76
Hard scatter	15.44±17.68	-15.76±32.29	4.08±21.4	39.07±27.04	-42.77±45.43	-24.41±25.25	-27.21±24.01	-77.3±73.98
Had./Frag.	-9.82±4.55	-2.12±6.47	-13.85±6.47	-3.84±8.56	-10.24±14.18	-21.71±7.87	-4.8±9.56	-21.16±13.63
Total	26.91±10.49	16.0±31.81	23.47±6.07	43.36±24.48	45.81±42.61	34.3±18.95	46.25±14.75	81.76±70.08

Table 6.8 Theoretical systematic uncertainties using the transfer factor method (TF) on the extrapolation for the TCR to the bWN, T1LCR, TVR, WCR, WVR, STCR, STVR for the bWN signal selection.

Theory uncertainties on ttbar VBV [%]							
	bWN	TVR	T1LCR	WCR	STCR	T1LVR	WVR	STVR
Radiation	14.01±3.55	5.42±3.45	29.8±1.71	26.07±1.8	28.64±1.59	25.56±1.77	22.11±1.85	27.31±1.68
Hard scatter	6.29±7.8	19.41±8.97	4.42±5.6	7.56±2.9	3.35±5.97	8.1±7.1	7.12±4.32	5.37±6.13
Had./Frag.	15.92±3.84	5.57±3.49	24.15±1.78	33.81±2.65	24.04±1.67	30.34±1.74	28.07±1.65	31.13±1.7
Total	22.12±4.2	20.91±8.43	38.61±1.84	38.76±7.38	37.54±1.7	40.49±2.23	32.17±2.01	41.76±1.85

Table 6.9 Theoretical systematic uncertainties using the VBV approach on the extrapolation for the TCR to the bWN, T1LCR, TVR, WCR, WVR, STCR, STVR for the bWN signal selection.

- Difference up and down scale

$$n = \frac{N_{up} - N_{down}}{N_{up} + N_{down}} \tag{6.6}$$

- Difference systematic and nominal samples

$$n = \frac{N_{syst} - N_{nom}}{N_{syst}} \tag{6.7}$$

In Figure 6.17 the histograms show the total number of events of the systematic and nominal samples for the $t\bar{t}$ systematics in every region for the different effects. At the bottom plot the output of the systematic uncertainties calculation with equations 6.6 and 6.7 is shown. With this is more clear where do the bad systematics come from. In the regions where we have less events and a bigger difference between the samples, the uncertainty is larger. This is one reason why the VBV approach helps to get better results.

6.4.2.IV W+jets

The uncertainty in the W+jets background from the merging of matrix elements and parton showers is studied by varying the scales related to the matching scheme. To estimate this, samples produced at EVENGEN [89] (SHERPA 2.2.0) only, and the uncertainty is evaluated at truth level. They have the following variations scales:

- **Renormalization scale variations (renorm):** varied by a factor of × 2 and × 0.5.

- **Factorization scale variations (fac):** varied by a factor of × 2 and × 0.5.

- **QSF variations (qsf):** varied by a factor of × 2 and × 0.5. It is the resummation scale.

- **CKKW matching variations(ckkw):** in this scale, the nominal value is 20 GeV and the variations goes down to 15 GeV and up to 30 GeV [87].
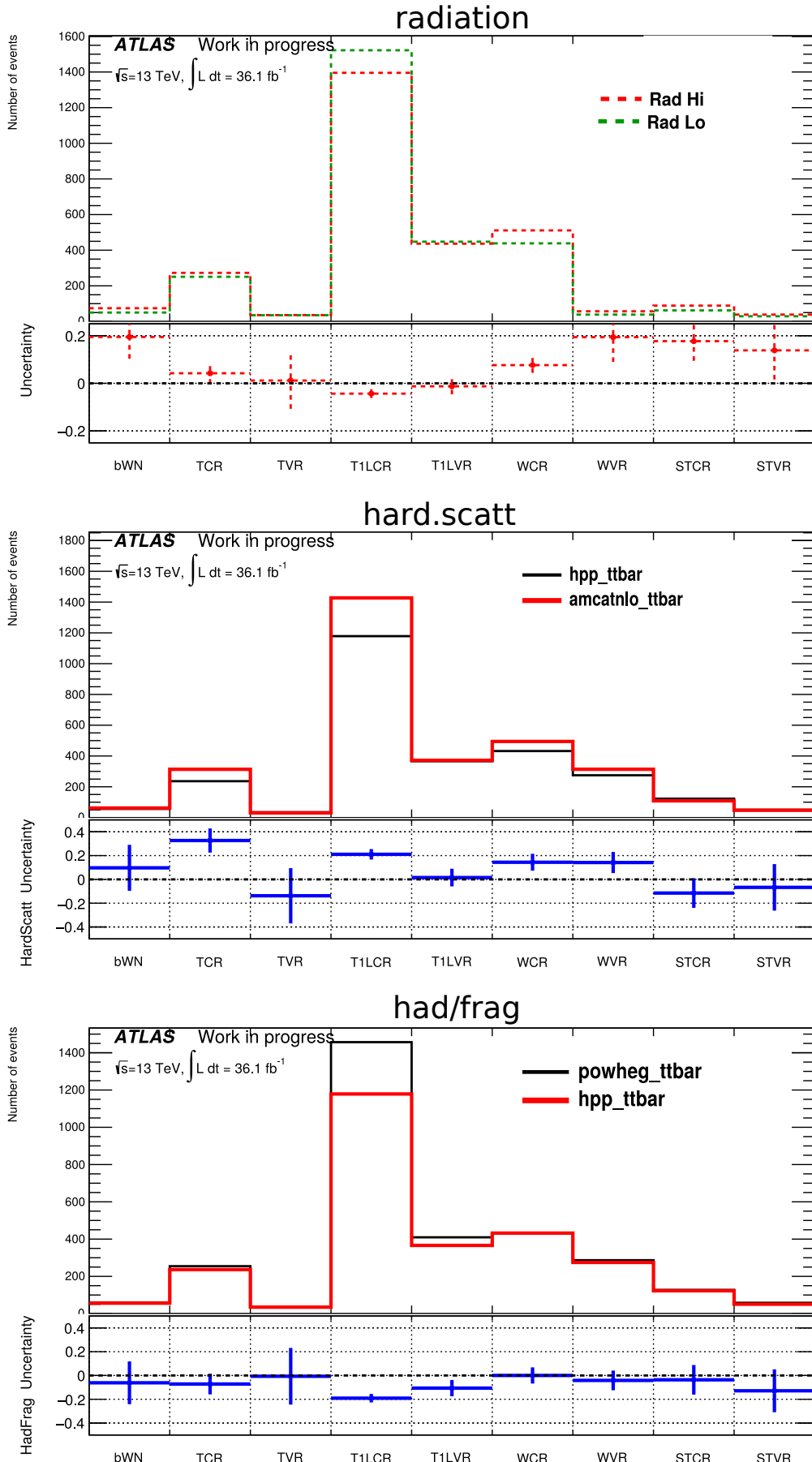
Figure 6.17 Histograms showing the number of events with the nominal and systematic
samples for each variation in $t\bar{t}$ theoretical uncertainties, per defined region. In the ra-
tio plot at the bottom of each histogram, the systematic uncertainty calculation (n) is
presented.

Theory uncertainties on W+jets [%]							
	bWN	TVR	T1LCR	TCR	STCR	T1LVR	WVR	STVR
ckk	3.02±15.05	0.13±21.0	2.55±3.25	-4.58±154.86	2.82±2.0	2.66±5.32	1.74±1.52	3.12±2.37
fac	4.08±15.05	3.34±20.92	3.35±3.25	1.26±144.0	3.38±1.99	3.34±5.31	3.35±1.51	3.55±2.36
generator	-4.69±28.63	-26.79±34.42	8.07±6.12	-33.76±83.5	11.1±4.17	16.37±9.85	8.46±1.65	17.72±6.93
qsf	0.6±14.98	0.99±20.95	0.57±3.25	3.61±147.53	0.22±1.98	0.57±5.31	0.87±1.51	-0.42±2.36
renorm	33.03±13.43	33.49±18.62	33.54±2.88	24.4±140.88	32.83±1.77	33.21±4.73	32.64±1.35	32.69±2.11
Total	33.75±13.92	43.03±25.92	34.76±3.15	42.08±107.82	34.94±2.14	37.28±6.07	33.93±1.37	37.49±3.77

Table 6.10 Theoretical systematic uncertainties using the transfer factor method (TF) on the extrapolation for the WCR to the bWN,T1LCR,TVR,TCR,WVR,STCR,STVR for the bWN signal selection.

Theory uncertainties on VBV W+jets [%]							
	bWN	TVR	T1LCR	TCR	STCR	T1LVR	WVR	STVR
ckk	0.85±0.06	1.65±0.24	0.67±0.01	1.97±0.38	1.2±0.02	1.29±0.01	0.89±0.01	1.58±0.03
fac	0.36±0.02	0.38±0.03	0.05±0.0	0.38±0.03	0.11±0.0	0.18±0.0	0.15±0.0	0.2±0.0
generator	13.92±2.55	30.5±4.66	9.42±0.17	27.9±4.23	9.66±0.22	8.67±0.18	3.53±0.05	10.65±0.3
qsf	0.88±0.04	1.7±0.27	0.17±0.0	1.98±0.26	0.54±0.01	1.17±0.01	1.07±0.01	1.38±0.01
renorm	1.5±0.09	2.19±0.25	0.21±0.0	2.46±0.31	0.27±0.01	0.35±0.0	0.41±0.0	0.4±0.0
Total	14.06±2.53	30.67±4.63	9.45±0.17	28.15±4.19	9.76±0.22	8.85±0.18	3.82±0.05	10.86±0.3

Table 6.11 Theoretical systematic uncertainties using the VBV approach on the extrapolation for the WCR to the bWN,T1LCR,TVR,TCR,WVR,STCR,STVR for the bWN signal selection.

- **Generator comparison (generator):** `MADGRAPH + PYTHIA 8` are chosen to evaluate the uncertainty due to the generator. The full difference between the nominal sample (`SHERPA`) and the systematic sample (`MADGRAPH`) is taken as the uncertainty.

As shown in the bullet points before, systematic uncertainties on the W+jets process arise from the merging of the matrix elements (ckkw), the parton shower modeling in `SHERPA` (qsf), the variation of the renormalization (renorm) and factorization (fac) scales. In addition, the uncertainty from the choice of MC generator is also considered and estimated by comparing the `SHERPA` and `MadGraph+Pythia 8` samples.

For calculating the reweights, formula 6.6 is used and for the generator the formula 6.7 is applied. In Figure 6.18 we can appreciate the number of events from the samples per region, and the uncertainty. In Table 6.10 the numerical results of the theory uncertainties are shown by TF method and in table 6.11 by VBV approach.
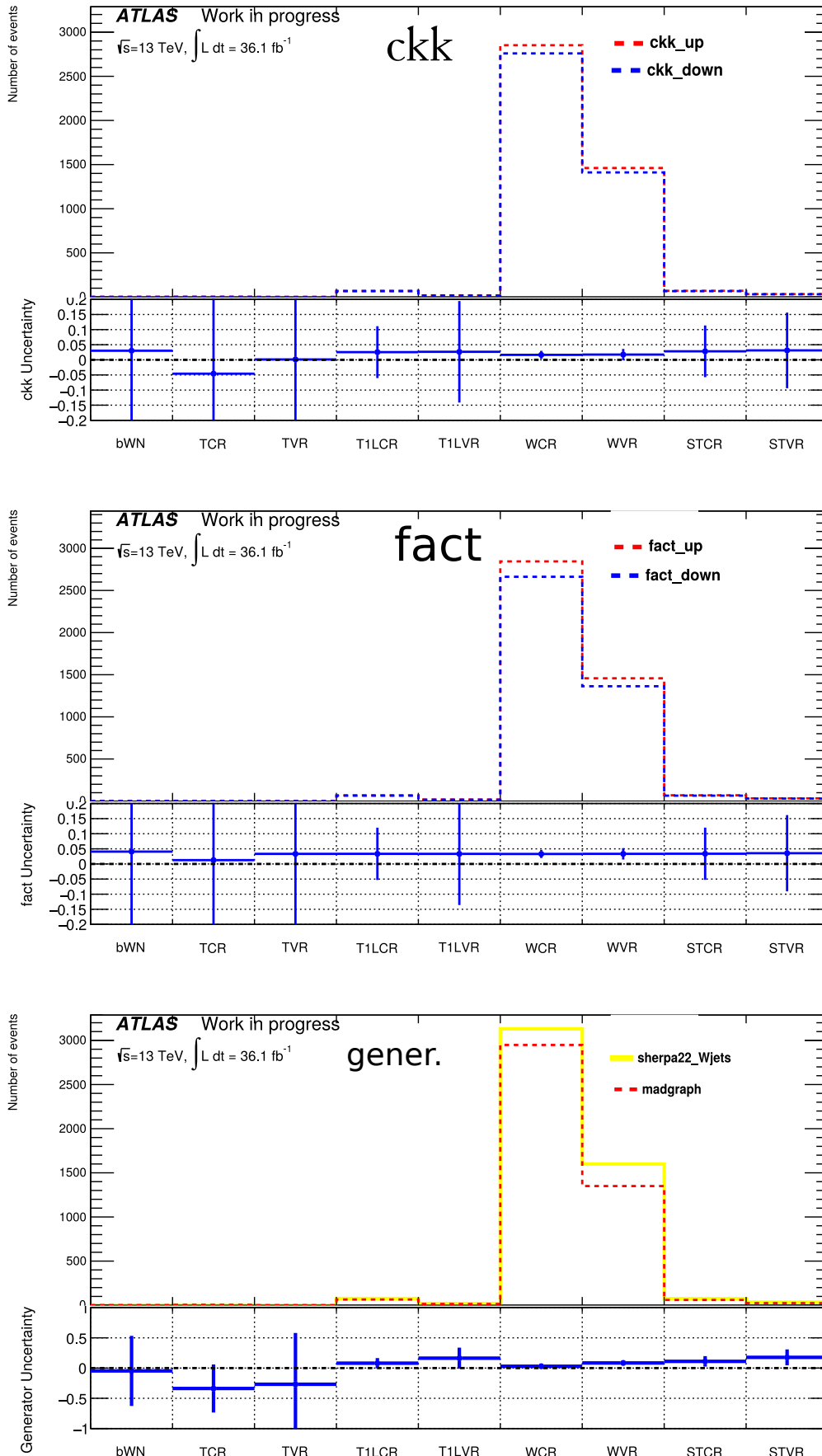
Figure 6.18 Histograms showing the W+jets events per defined region, with the nominal and systematic samples for each variation in the W+jets theoretical uncertainties. In the ratio plot at the bottom of each histogram, the systematic uncertainty calculation (n) is presented.
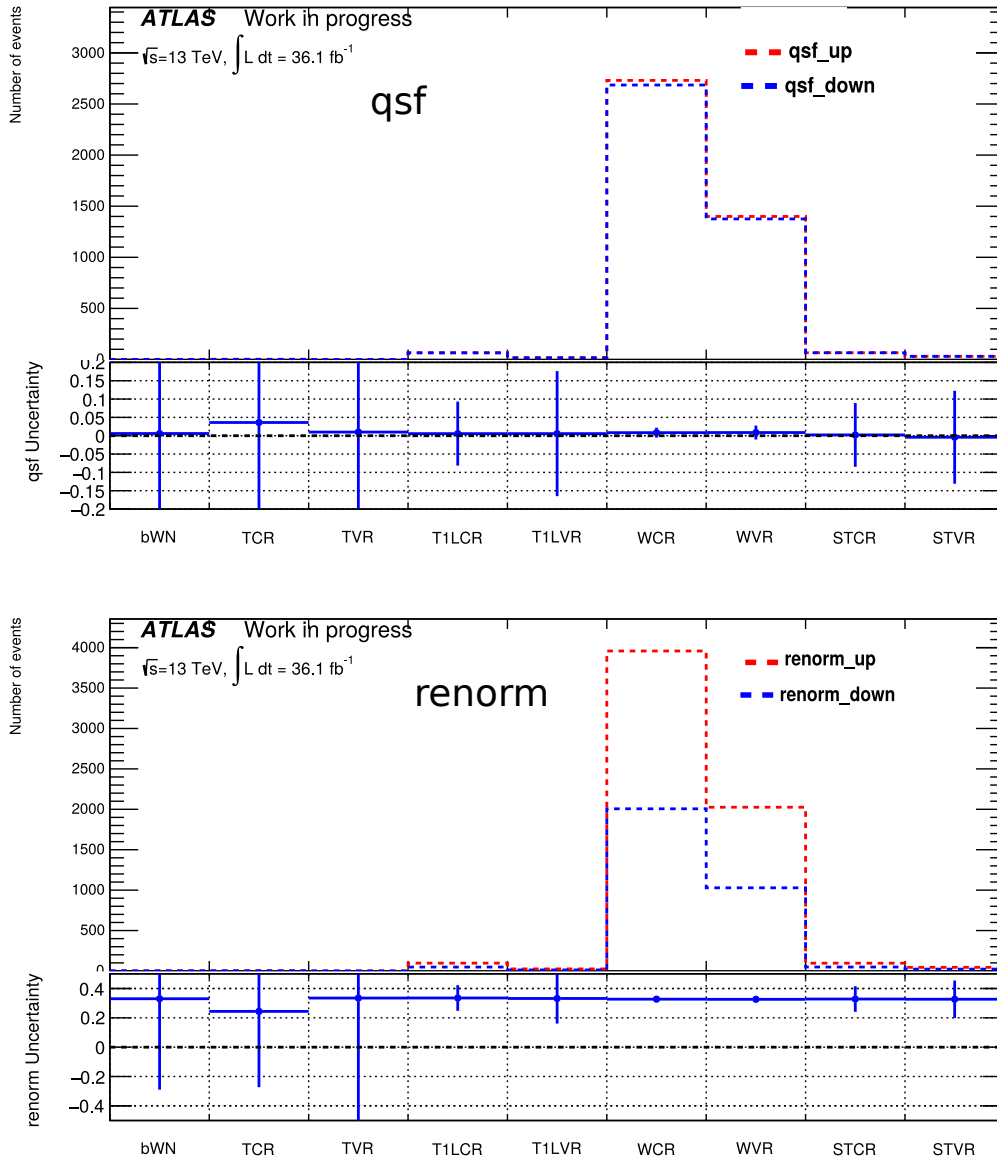
Figure 6.18 Histograms showing the $W+$jets events per defined region, with the nominal and systematic samples for each variation in the $W+$jets theoretical uncertainties. In the ratio plot at the bottom of each histogram, the systematic uncertainty calculation (n) is presented.

6.3.2.V Single Top

The only relevant mode of he single top in the analysis is the Wt channel.

- **MC generator/ hard scatter:** The MC generator uncertainty is estimated by a comparison of `POWHEG+HERWIG++` sample as the nominal and `aMC@NLO+HERWIG++` as the systematic sample.

- **Fragmentation/ hadronization (Had/Frag):** The events generated with `POWHEG` are hadronized by comparing with `HERWIG++` as `POWHEG+HERWIG++` taken the systematic sample, and with `PYTHIA6` as `POWHEG+PYTHIA6` taken the nominal sample.

- **Additional Radiation:** As in the $t\bar{t}$ variation, using `POWHEG+PYTHIA` and a variation to the lower limit of the radiation, radiation low (radLo), and a variation in the upper limit, radiation high (radHi) is taken.

- **Interference:** There can be terms of interference between Wt and $t\bar{t}$ at NLO. It has been observed that the diagram removal (DR)[3] versus the diagram substraction (DS)[4] approach is not a reasonable comparison in the region of phase space studied, because it can easily reach one order of magnitude [87]. A different approach is followed in the LO MC samples, generating separated samples for $t\bar{t}$, Wtb, and $WWbb$ with `MADGRAPH` LO multi-leg processes. The sum of the $t\bar{t} + Wtb$ is taken as the nominal sample, and the $WWbb$ contribution as the systematic sample.

The formulas used to calculate the double ratio in for the single top uncertainties are applied with the same logic as equation in 6.7 in hard scatter, had/frag and interference. For radiation we use the same formula as in equation 6.6.

The histograms in Figure 6.19 show the number of events of the samples in each dedicated region used for the calculations of the uncertainties for W+jets. In the ratio plot at their bottoms the calculation of the systematic uncertainties (n) is presented. In Tables 6.12 and 6.13 the systematics by TF and VBV methods are shown.

---

[3]Which does not include diagrams with $t\bar{t}$. The interference term with the leading order of $t\bar{t}$ and Wt production is removed.

[4]It substracts the resonant $t\bar{t}$ contribution locally from the cross section.

Theory uncertainties on single Top [%]							
	bWN	TVR	T1LCR	WCR	TCR	T1LVR	WVR	STVR
Radiation	27.7±8.25	5.26±17.63	4.43±1.18	19.11±5.06	13.8±5.42	7.51±2.23	-4.25±10.29	22.93±0.69
Hard scatter	-70.11±18.91	-33.5±36.82	-36.4±3.98	-29.74±22.86	-18.02±17.26	-47.17±6.9	-100.0±23.98	-41.83±2.47
Had./Frag.	143.21±53.24	390.22±164.14	89.31±5.63	56.34±21.82	232.65±39.81	78.71±9.49	247.81±105.23	82.41±3.55
Interference	14.08±11.95	-5.14±9.45	-2.21±2.24	-53.43±55.87	-3.89±3.65	-0.17±4.08	-100.0±0.0	-37.12±5.12
Total	162.45±47.67	391.73±163.54	96.57±5.42	85.31±38.69	233.78±39.64	92.07±8.85	285.35±43.63	102.2±3.57

Table 6.12 Theoretical systematic uncertainties using the TF method on the extrapolation for the STCR to the SR and the corresponding CRs and VRs for the bWN signal selection.

Theory uncertainties on Single Top VBV [%]							
	bWN	TVR	T1LCR	WCR	TCR	T1LVR	WVR	STVR
Radiation	6.41±3.38	11.6±6.29	9.18±0.68	10.4±0.82	7.93±3.39	12.27±1.62	13.98±1.72	10.4±0.47
Hard scatter	29.3±17.69	35.45±10.44	4.46±3.54	13.11±8.5	72.0±23.63	27.58±13.04	45.78±16.06	13.35±3.03
Had./Frag.	34.24±5.1	29.43±3.63	10.04±1.36	8.74±1.88	36.11±4.84	12.83±4.33	14.02±4.65	3.26±1.1
Interference	145.29±1.59	127.21±2.1	100.03±0.73	100.42±4.86	126.24±1.95	116.78±0.91	118.24±7.65	130.0±1.13
Total	152.25±3.9	135.79±3.49	101.05±0.76	102.18±4.9	149.95±11.52	121.3±3.13	128.33±9.1	131.13±1.17

Table 6.13 Theoretical systematic uncertainties using the VBV approach on the extrapolation for the STCR to the SR and the corresponding CRs and VRs for the bWN signal selection.
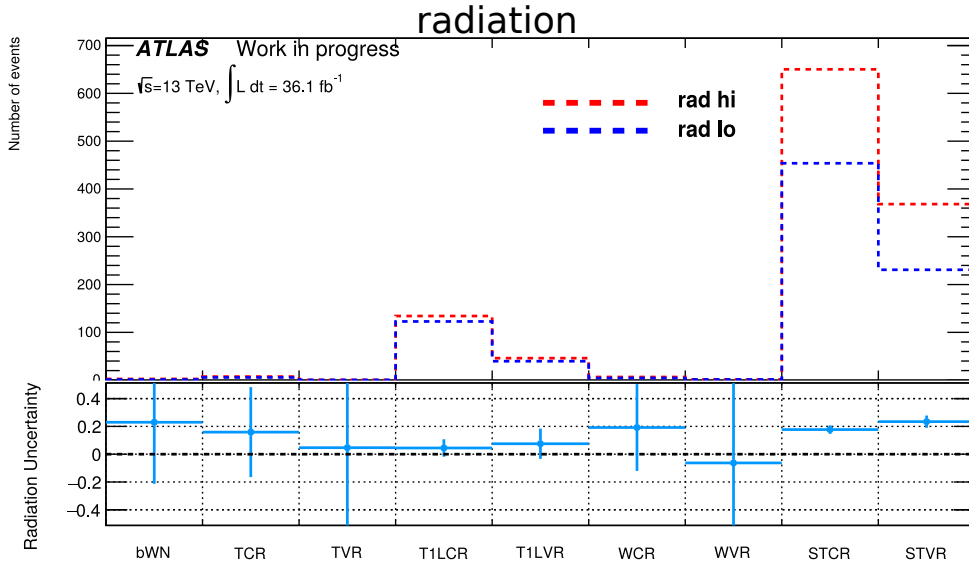
Figure 6.19 Histograms showing the single top number of events per defined region, with the nominal and systematic samples for each variation or effect in the Single Top theoretical systematic uncertainties. In the ratio plot at the bottom of each histogram, the systematic uncertainty calculation (n) is presented.
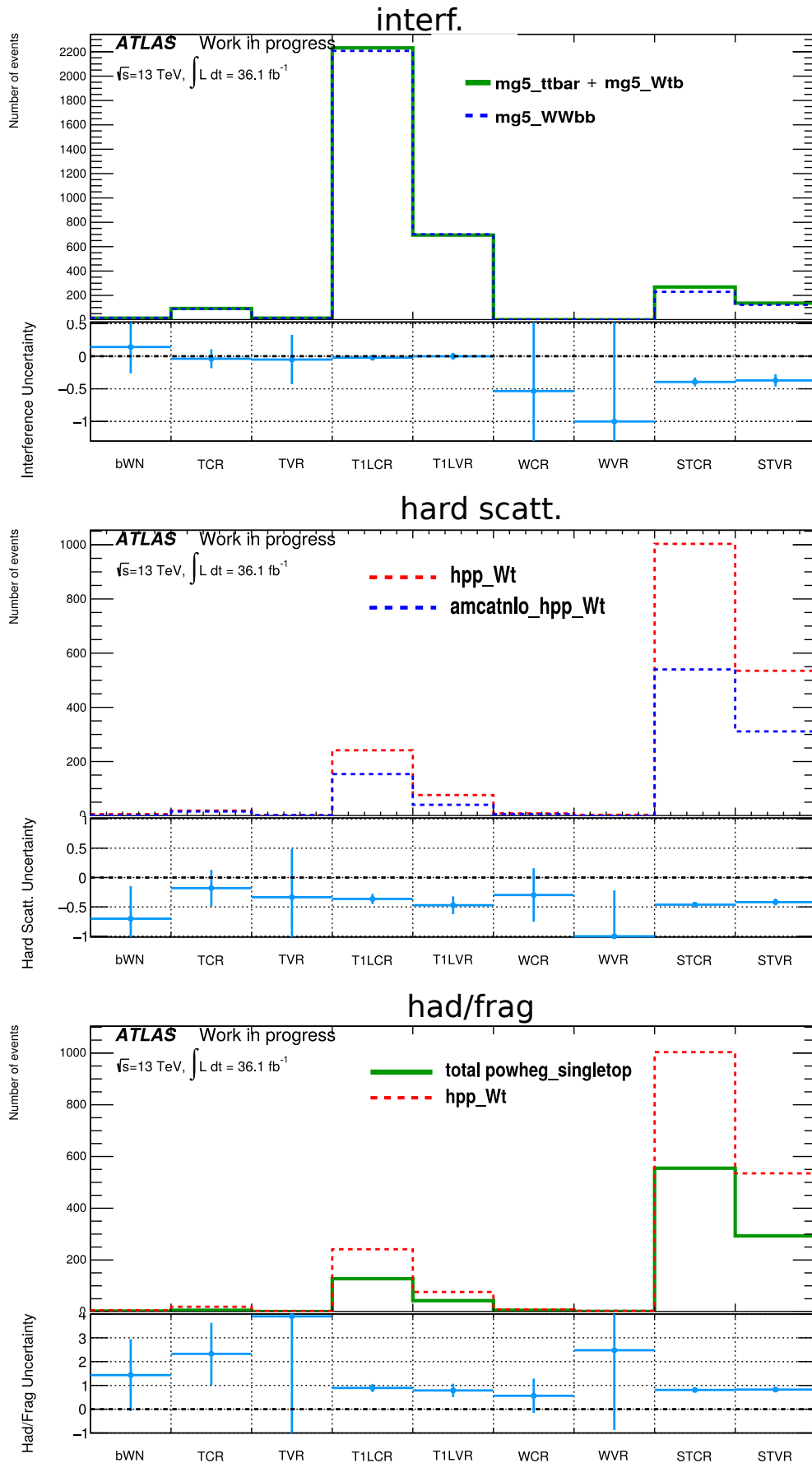
Figure 6.19 Histograms showing the single top number of events per defined region,
with the nominal and systematic samples for each variation or effect in the Single Top
theoretical systematic uncertainties. In the ratio plot at the bottom of each histogram,
the systematic uncertainty calculation (n) is presented.

6.5 Background Fit

Particle physics experiments have a large number of data samples and they need to be carefully analyzed. In general, the analyses rely on the predicted number of signal and background events in data. As discussed in the previous sections, the expected numbers of background events may be constructed entirely from simulated events or data-driven methods (i.e. using dedicated control regions). In the case of a search for physics beyond the SM, the expected number of signal events are always obtained from simulations[5]. In the case that no excess over the expected SM background is observed in the data, exclusion limits can be set on these parameters, as shown in more detail in chapter 7.

6.5.1 Outline of Fitting Setup

Background events follow a Poisson probability distribution as [143]:

$$P(n_i|b_i) = \frac{b_i^{n_i}}{n_i!}e^{-b_i} \tag{6.8}$$

Where $P(n_i|b_i)$ is the probability to observe n_i events in bin i when b_i background events are expected. The same holds for the signal-plus-background model, and in a more specific expression introducing our different CRs as:

$$P(n_i|s_i,b_i) = \frac{(s_i + (b_{i_{t\bar{t}}} + b_{i_{W+jets}} + b_{i_{ST}}))^{n_i}}{n_i!}e^{-(s_i+(b_{i_{t\bar{t}}}+b_{i_{W+jets}}+b_{i_{ST}}))} \tag{6.9}$$

with s_i the number of expected signal events in bin i and b_i the number of backgorund events in bin i in the different control regions defined.

The search results are obtained by maximizing a likelihood function. The inputs to the likelihood fit are the number of expected and observed events in the SR and CRs. The concept of likelihood can be explained with an event counting experiment, in which a variable is measured in a signal region and the resulting data is summarized in a histogram. The number of entries are denoted by $n = n_1 + n_2...$ The expectation value for bin i to have n_i entries is calculated by:

$$E[n_i] = \mu s_i + b_i \tag{6.10}$$

where μ is the strength of the signal process. So $\mu = 0$ stands for the background-only hypothesis and $\mu = 1$ for the signal-plus background model [140]. The s_i and b_i events are obtained by probability density functions (PDFs). The shape of the PDFs are characterized by nuisance parameters describing the effect of systematic uncertainties [140] and explain in more detail in [141].

As the experiment can depend on different variables, the total probability of obtaining a specific result is given by the product of the individual probabilities for each bin [141], which is the likelihood. The systematic uncertainties are included as nuisance parameters and profiled in the likelihood fits. The nuisance parameters are constrained by terms corresponding to the sizes of the systematic uncertainties. The nuisance parameters contain the normalization parameters related to backgrounds and the systematic and statistical uncertainties described in the previous section.

---

[5]The simulation of the signal process depends in our case on the masses of the stop $\tilde{t}_1$ and neutralino $\tilde{\chi}_1^0$.

The fit performed to data is based on statistically independent CRs and SR, ensuring that they can be modeled by different PDFs and combined in a simultaneous fit. Through the fit to data, the observed event counts in CRs are used to coherently normalize the background estimates in all regions, notably in the SR.

Between the common fit strategies, in this thesis only a background-only fit was performed using the uncertainties results by VBV approach from tables 6.9, 6.11 and 6.13.

6.5.2 Background-Only Fit

The fit performed to data is based on statistically independent CRs and SR, ensuring that they can be modeled by different PDFs and combined in a simultaneous fit. Through the fit to data, the observed event counts in CRs are used to coherently normalize background estimates in all regions, notably in the SR.

The fit is performed using the HistFitter software framework [142]. It is a flexible and programmable framework and contains tools to perform the fits, as well as interpret and present results. In the HistFitter package, a PDF is constructed from the parameters of interest. The figure of merit for excluding a part of the parameter space in a BSM search is based on the so-called confidence level (CL) method [146] which is also implemented in HistFitter, and explained in more detail in section 7.2.

Here the free parameters are $\mu_{t\bar{t}}$, μ_{Wjets} and $\mu_{singletop}$ of the $t\bar{t}$, W+jets and Single Top backgrounds, respectively. For diboson and $t\bar{t}+Z/W$ background samples are assigned 23% and 99% of normalization uncertainty respectively. By doing so the systematic uncertainties assigned to these backgrounds are assumed to be uncorrelated to one another.

There is a good agreement between the observed events in the bWN SR and the fitted background events from the different backgrounds as shown in Table 6.14. In Table 6.15 a breakdown of the dominant systematic uncertainties on background estimated in signal is presented, for all SR, CRs and VRs.

yields channel	bWN	TCR	TVR	T1LCR	T1LVR	WCR	WVR	STCR	STVR
Observed events	68	293	62	1599	109	3316	355	296	141
Fitted bkg events	68.87 ± 6.57	292.27 ± 16.89	52.77 ± 5.96	1599.73 ± 38.87	133.03 ± 12.80	3314.85 ± 57.46	343.13 ± 22.74	295.92 ± 17.62	141.77 ± 9.48
Fitted powheg_ttbar events	62.47 ± 6.39	272.70 ± 18.57	48.44 ± 6.07	1428.82 ± 42.79	115.99 ± 12.75	427.60 ± 87.41	47.03 ± 11.13	66.23 ± 7.45	29.70 ± 4.00
Fitted sherpa22_Wjets events	1.44 ± 0.61	4.09 ± 2.17	0.66 ± 0.40	65.16 ± 17.42	6.01 ± 1.82	2674.71 ± 128.88	274.19 ± 25.61	54.88 ± 17.22	26.32 ± 8.57
Fitted powheg_singletop events	2.22 ± 0.78	5.70 ± 1.34	1.23 ± 0.57	89.53 ± 16.00	9.52 ± 1.98	59.44 ± 17.13	6.00 ± 2.26	167.07 ± 28.65	82.05 ± 14.28
Fitted amcnlo_ttV events	1.86 ± 1.81	7.74 ± 7.50	1.97 ± 1.92	10.06 ± 9.83	1.16 ± 1.13	3.18 ± 3.14	$0.44^{+0.45}_{-0.44}$	3.60 ± 3.51	2.08 ± 2.03
Fitted sherpa221_diboson events	0.87 ± 0.28	2.03 ± 0.66	0.46 ± 0.14	6.16 ± 2.10	0.34 ± 0.21	149.91 ± 40.31	15.48 ± 4.80	4.15 ± 1.73	1.64 ± 0.83
MC exp. SM events	67.95	273.25	50.54	1645.32	137.31	3767.65	389.82	301.30	144.45
MC exp. powheg_ttbar events	61.42	253.38	46.19	1466.41	119.63	431.74	47.62	68.09	30.80
MC exp. sherpa22_Wjets events	1.69	4.76	0.77	76.40	7.04	3126.51	320.63	64.40	30.85
MC exp. powheg_singletop events	2.13	5.47	1.19	86.41	9.16	57.05	5.72	161.11	79.12
MC exp. amcnlo_ttV events	1.84	7.61	1.94	9.93	1.14	3.13	0.43	3.55	2.05
MC exp. sherpa221_diboson events	0.87	2.03	0.46	6.17	0.35	149.21	15.42	4.14	1.63

Table 6.14 Observed events in the control and validation regions for bWN together with the fitted background events for 36.1^{-1} fb. The lower part of the table shows the background estimates as obtained from Monte Carlo before the background-only fit. The upper part of the table shows the corrected values after the fit. Note that the individual uncertainties can be correlated, and do not necessarily add up quadratically to the total background uncertainty.

| Uncertainty of channel	bWN	TCR	TVR	T1LCR	T1LVR	WCR	WVR	STCR	STVR
Total background expectation	68.87	292.27	52.77	1599.73	133.03	3314.85	343.13	295.92	141.77
Total statistical ($\sqrt{N_{\mathrm{exp}}}$)	±8.30	±17.10	±7.26	±40.00	±11.53	±57.57	±18.52	±17.20	±11.91
Total background systematic	±6.57 [9.54%]	±16.89 [5.78%]	±5.96 [11.30%]	±38.87 [2.43%]	±12.80 [9.62%]	±57.46 [1.73%]	±22.74 [6.63%]	±17.62 [5.96%]	±9.48 [6.68%]
alpha_powheg_ttbar_Fragmentation	±7.04	±0.00	±2.49	±259.92	±28.52	±71.30	±10.09	±12.64	±7.48
alpha_powheg_ttbar_Radiation	±5.78	±0.00	±1.72	±270.50	±18.79	±69.06	±6.46	±12.52	±5.28
alpha_powheg_ttbar_HardScatter	±5.27	±0.00	±5.08	±60.00	±9.04	±18.64	±3.45	±2.92	±1.96
mu_ttbar	±5.51	±24.06	±4.27	±126.07	±10.23	±37.73	±4.15	±5.84	±2.62
alpha_JES_GroupedNP1	±2.81	±8.26	±0.66	±14.23	±5.11	±34.89	±1.75	±5.37	±2.58
alpha_xsec_powheg_singletop	±2.18	±5.62	±1.22	±88.57	±9.40	±58.64	±5.90	±165.07	±81.07
mu_singletop	±2.15	±5.53	±1.20	±86.88	±9.24	±57.68	±5.82	±162.11	±79.61
alpha_xsec_amcnlo_ttV	±1.80	±7.49	±1.90	±9.76	±1.12	±3.08	±0.43	±3.49	±2.01
gamma_stat_bWN_cuts_bin_0	±1.57	±0.00	±0.00	±0.00	±0.00	±0.00	±0.00	±0.00	±0.00
alpha_bTag	±1.28	±6.28	±0.97	±55.81	±4.49	±85.20	±10.14	±11.59	±5.98
alpha_MET_Reso_para	±1.27	±1.75	±0.15	±1.11	±0.63	±0.54	±1.95	±1.15	±0.23
alpha_prw	±1.07	±6.79	±0.64	±63.18	±5.96	±75.48	±10.88	±13.25	±5.49
alpha_cTag	±1.05	±0.69	±0.70	±27.02	±2.02	±59.29	±6.41	±14.89	±6.61
alpha_MET_Reso_perp	±1.01	±1.86	±0.58	±0.04	±0.66	±1.34	±2.51	±1.06	±0.85
alpha_cextra	±0.68	±0.32	±0.39	±0.17	±0.08	±0.21	±0.05	±0.01	±0.00
mu_wjets	±0.60	±1.70	±0.28	±27.14	±2.51	±1114.23	±114.22	±22.86	±10.96
alpha_xsec_sherpa22_Wjets	±0.60	±1.69	±0.27	±26.91	±2.48	±1103.93	±113.19	±22.67	±10.86
alpha_sherpa22_Wjets_generator	±0.41	±1.90	±0.34	±11.14	±0.97	±0.00	±19.37	±10.10	±5.41
alpha_MET_Scale	±0.40	±0.74	±0.22	±2.88	±0.05	±3.00	±0.11	±0.74	±0.10
alpha_JES_GroupedNP2	±0.34	±1.75	±0.41	±1.45	±0.44	±2.97	±3.52	±0.41	±0.53
alpha_JES_NonClosure	±0.28	±0.04	±0.07	±1.66	±0.66	±1.58	±1.77	±0.36	±0.43
alpha_JER	±0.23	±7.18	±0.80	±23.79	±0.06	±20.15	±1.16	±0.52	±0.08
alpha_xsec_sherpa221_diboson	±0.20	±0.46	±0.10	±1.41	±0.08	±34.22	±3.54	±0.95	±0.37
alpha_bextra	±0.08	±0.25	±0.08	±5.97	±0.21	±4.80	±0.72	±6.17	±3.63
alpha_JES_GroupedNP3	±0.05	±0.26	±0.10	±1.34	±0.01	±4.49	±0.62	±0.86	±0.23
alpha_lTag	±0.05	±1.57	±0.15	±11.53	±1.13	±53.07	±5.68	±11.39	±5.10
alpha_sherpa22_Wjets_renorm	±0.02	±0.10	±0.01	±0.14	±0.02	±0.00	±1.13	±0.15	±0.10
alpha_sherpa22_Wjets_qsf	±0.01	±0.08	±0.01	±0.09	±0.07	±0.00	±2.91	±0.29	±0.36
alpha_sherpa22_Wjets_ckk	±0.01	±0.08	±0.01	±0.43	±0.08	±0.00	±2.43	±0.66	±0.41
alpha_sherpa22_Wjets_fac	±0.01	±0.02	±0.00	±0.03	±0.01	±0.00	±0.40	±0.06	±0.05

Table 6.15 Breakdown of the dominant systematic uncertainties on background estimates in the signal, control, and validation regions for the bWN analysis. Note that the individual uncertainties can be correlated, and do not necessarily add up quadratically to the total background uncertainty. The percentages show the size of the uncertainty relative to the total expected background.

Uncertainty of channel	bWN	TCR	TVR	T1LCR	T1LVR	WCR	WVR	STCR	STVR
gamma_stat_TCR_bWN_cuts_bin_0	±0.00	±5.79	±0.00	±0.00	±0.00	±0.00	±0.00	±0.00	±0.00
gamma_stat_T1LVR_bWN_cuts_bin_0	±0.00	±0.00	±0.00	±0.00	±2.41	±0.00	±0.00	±0.00	±0.00
gamma_stat_WCR_bWN_cuts_bin_0	±0.00	±0.00	±0.00	±0.00	±0.00	±23.99	±0.00	±0.00	±0.00
gamma_stat_TVR_bWN_cuts_bin_0	±0.00	±0.00	±1.39	±0.00	±0.00	±0.00	±0.00	±0.00	±0.00
gamma_stat_T1LCR_bWN_cuts_bin_0	±0.00	±0.00	±0.00	±11.47	±0.00	±0.00	±0.00	±0.00	±0.00
gamma_stat_STCR_bWN_cuts_bin_0	±0.00	±0.00	±0.00	±0.00	±0.00	±0.00	±0.00	±3.77	±0.00
gamma_stat_WVR_bWN_cuts_bin_0	±0.00	±0.00	±0.00	±0.00	±0.00	±0.00	±5.48	±0.00	±0.00
gamma_stat_STVR_bWN_cuts_bin_0	±0.00	±0.00	±0.00	±0.00	±0.00	±0.00	±0.00	±0.00	±2.16

Table 6.15 Breakdown of the dominant systematic uncertainties on background estimates in the signal, control, and validation regions for the bWN analysis. Note that the individual uncertainties can be correlated, and do not necessarily add up quadratically to the total background uncertainty. The percentages show the size of the uncertainty relative to the total expected background.

6.5.3 Background-Only Fit Results

- **in CRs:** The results table 6.13, show the background estimates after the fit to the control regions in the upper part and the background estimates obtained from Monte Carlo simulation at the bottom. On the first lines, the number of observed events is given and it is compared to the fitted total background expectation values. The background-only fit leads to a very good agreement between the total fitted background estimate and the data in all CRs.

- **in VRs:** The results of the background-only fit in the CRs are extrapolated to the VRs in order to cross-check the extrapolation to larger E_T^{miss} and lower am_{T2} values and thus to the SR. The background estimates before and after the background-only fit are shown together with the observed data in Table 6.13 for the validation regions with the VRs suffixes. The agreement between fitted background estimates and observed data is also summarized in the pull plot in Figure 6.20. The pull plot shows at the bottom the difference of the observed data subtracted by the number of expected events normalized to the total uncertainty (including statistical and systematic uncertainties), which are called pulls. The background estimates in the validation regions after the fit are slightly lower than the observed number of data in the TVR and WVR, in the T1LCR the numbers are higher, as seen in Table 6.13. However, the fitted background estimates are in agreement with observed data within 1σ, as shown in the pull plot.
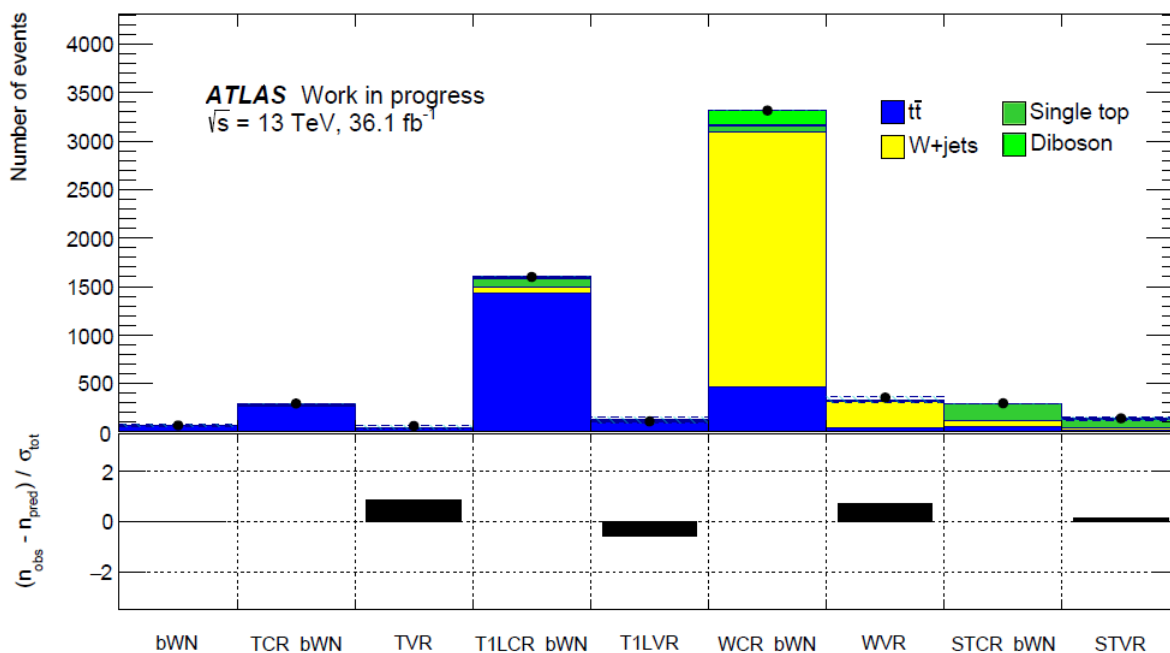
Figure 6.20 fitted number of events after performing the fit, in the different regions. At the bottom the pulls are shown for the four VRs. The fitted background estimates slightly overestimate in the observed data for T1LVR, therefore the pulls are shifted to negative values. However, the deviations are within 1σ when considering all uncertainties.

- **in SR:** Similarly to the case of the VRs, the results of the background-only fit in the CRs are extrapolated to the SR. The fitted background estimate yields 68.87 ± 6.57 in the bWN region and 68 observed events. A good agreement between data and fitted background estimates is shown. In fact, comparing these results with the

ones in the actual analysis [89], where only one dedicated CR (TCR) was defined, an improvement is reached. By defining CRs for the other sub-leading backgrounds in the analysis, we obtain a reduction in background uncertainties of about $\sim 50\%$. The improvement can be appreciated in Table 6.16 where a reduced version of the results tables from this studies and the current analysis is shown. It contains the observed events and fitted background events and the total background uncertainty.

The uncertainties on the background estimates contain both systematic and statistical uncertainties. A break-down into the various components is given in Table 6.14. Due to correlations, the final uncertainties do not necessarily match to the squared sum of the single uncertainties. The $t\bar{t}$ fragmentation, radiation and hard scattering have the largest contribution to the total uncertainty. In this part, we can also see a reduction in the background systematic numbers, compared with the results of the current analysis as shown in Table 6.16.

Uncertainty of channel	bWN	TCR	TVR
Observed Events	68	293	62
Fitted bkg events	70.70±15.70	292.89 ± 17.11	52.43±8.34
Total statistical ($\sqrt{N_{exp}}$)	±8.41	±17.11	±7.45
Total background systematic	±15.70 [22.18%]	±17.11 [5.94%]	±8.34 [15.04%]

Uncertainty of channel	bWN	TCR	TVR
Observed Events	68	293	62
Fitted bkg events	68.87±6.57	292.27 ± 16.89	52.77±5.96
Total statistical ($\sqrt{N_{exp}}$)	±8.30	±17.10	±7.26
Total background systematic	±6.57 [9.54%]	±16.89 [5.78%]	±5.96 [11.30%]

Table 6.16 On the top table, the results of background-only fit in the current analysis [87] with only one dedicated CR for the main background. The data shows a small under-fluctuation in the bWN channel. At the bottom table, the results of this studies with dedicated CRs for the other sub-backgrounds. After the background-only fit as shown in bottom table, an improvement in the fitted background in the bWN is achieved in comparison with the upper table. The total background systematics are are significantly reduced after the fit.

Chapter 7

Results

7.1 Limits

For calculating the significance of a signal excess, a probability is defined to interpret elements of a set as a hypothesis, i.e. statements which are true or false and explained in more detail in [144]. In a hypothesis test two assumptions are taken. First the null hypothesis H_0: background-only processes exists, and secondly the hypothesis H_1: both signal-plus-background processes exists. In the simplest case, the hypothesis test is a number counting experiments for these assumptions.

The crucial part in the hypothesis test is the decision when the null hypothesis H_0 should be accepted or rejetced. Ideally the probabiity of rejecting H_0 should kept small. For this purpose a significance level α is definded, usually before performing the test and by convention with a small value, about 0.05, explained in [144]. As the signal model is characterized by continuous parameters representing the masses of new particles (stop and neutralino masses), we can perform a test in the range of α for the most important values in our 3-body diagonal phase space, and those values who are not rejected constitute what is called a *confidence region* for parameters with a *confidence level* of CL = $1-\alpha$. By construction a hypothesized point in parameter space will, if it is true, be rejected with probability α. Therefore the confidence region will contain the true value of the parameters with probability $1 - \alpha$. With α set at = 0.05 as said before, the regions will have a confidence level of 95%.

The outcome of the hypothesis can be expressed in the $p-$value. The $p-$value gives the probability to observe the same or more extreme results than the measured one, assuming H_0 to be true. It describes how likely it is that an observed excess, potentially coming from the signal-plus-background model, is caused by background processes. Following this, a model is excluded if p_{s+b} <5%, which corresponds to CL_{s+b}=95%. This can be problematic for low sensitivity in the signal processes, i.e. having a number of background and signal events almost equal to the background-only events ($s + b \approx b$). Such models can be falsely excluded. To avoid this, the CL_s method is introduced as [145]:

$$CL_s = \frac{p_{s+b}}{1 - p_b} \tag{7.1}$$

If the test statistics of $s + b$ and b are close to each other, then p_b is large and the denominator is therefore small. As a consequence CL_s is larger than CL_{s+b}. In the case where p_b is small and the denominator is ~ 1, we have $CL_s \sim CL_{s+b}$. So the model should be choose to have an exclusion of CL_s <5%.

The $p-$value is equivalently formulated by the significance Z which is the number of standard deviations a Gaussian variable would need to fluctuate in one direction to give the same $p-$value. The significance (Z) is obtained by [144]:

$$Z = \Phi^{-1}(1 - p) \tag{7.2}$$

Φ^{-1} is the inverse of the cumulative distribution of the standard Gaussian. Z measures the probability in units of standard deviations (σ) that an observed excess in data would correspond to a statistical fluctuation of the hypothesized background.

After performing the hypothesis tests with HistFitter framework [142], and running it over the main mass points $\Delta m(\tilde{t}_1, \tilde{\chi}_1^0) < m_{top}$ corresponding to the phase space in the 3-body decay, the results are presented in Figure 7.1. The expected significance plots can be appreciated. On the top we have the results of the current analysis, and on the bottom in this studies. The numbers in the plots are the results of the expected significance in those mass points, while the dotted line represents the limits excluded.

From Figure 7.1 we can see that the exclusion limit is improved with these studies (i.e. gaining more space in the diagonal where the 3-body decay takes place), going up to stop masses of 450 GeV and neutralino masses of 300 GeV. The sensitivity numbers are also higher specially in the bins for the stop mass of 250 and 300 GeV.

If no significant excess of data over SM background expectation is observed, one can set exclusion limits on the parameter space of the signal model with a certain confidence level (CL). Figure 7.2 shows the contour which encloses the signal points tha can be excluded, from the 3-body decay phase space diagonal, with $CL \geq 95\%$, derived using the hypothesis testing utility of HistFitter framework [142]. At the top the results to for the current analysis and at the bottom the results of the studies for these thesis. The red curve of the plot shows the observed limit. This curve has been calculated by using the nominal signal cross sections. When modifying the signal cross sections (up or down) by their theoretical uncertainties and evaluated as described in the last section, the dotted red lines are obtained. The yellow band indicates the $\pm 1\sigma$ variations on the expected limit [142]. All lines are given at a 95% CL.
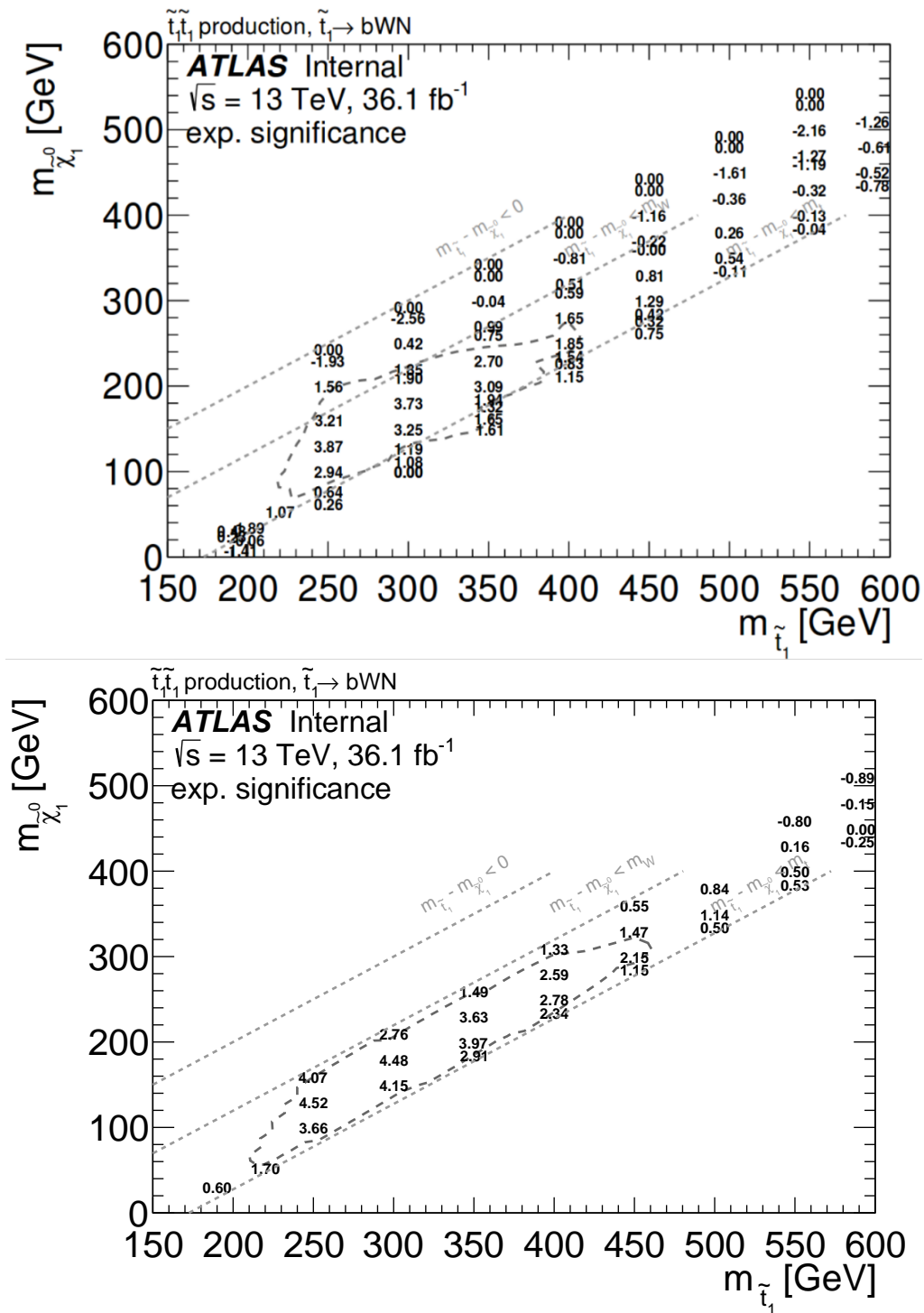
Figure 7.1 Expected significance result plots for the 3-body decay diagonal. On the top the result of the current analysis [89] and on the bottom the results of the studies made for this thesis.
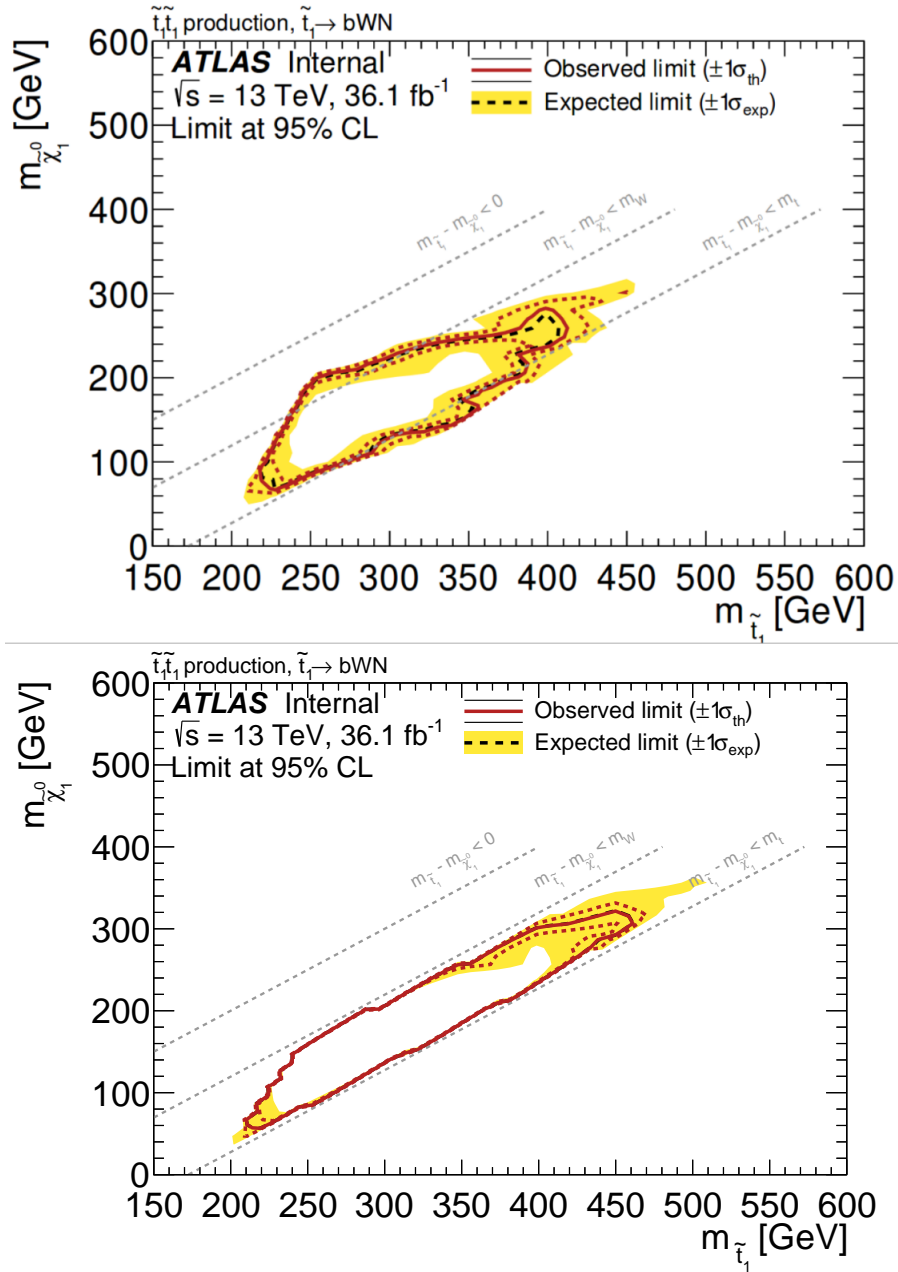
Figure 7.2 Exclusion limits at 95% *CL* together with its $\pm 1\sigma$ error band calculated by HistFitter in the $(m_{\tilde{t}_1}, m_{\tilde{\chi}_1^0})$-plane. The red curve shows the observed limit. On the left side the results of the current analysis is presented [89]. On the right side the results of the studies of these thesis. Both plots are generated for an integrated luminosity of 36.1 fb^{-1}.

Chapter 8

Sensitivity Studies in the 4-Body Channel

In this chapter a short description of a more compressed phase space in a pure bino LSP scenario will be given. The target of this phase space is the pair production of top squarks with a mass splitting of at most 80 GeV. For small mass splittings, the lepton in the final sate originate from a virtual W boson decay, and is expected to have low p_T. The stop quark can decay to a bottom quark, two different and light fermions and the LSP. Preliminary studies defining an optimal signal region will be presented.

8.1 4-Body Decay

For the stop four body decay the difference in the mass Δm of the stop-neutralino phase space is even smaller than in the 3-body case. This decay channel happens when $\Delta m(\tilde{t}_1, \tilde{\chi}_1^0) < m_W$, so the $\tilde{t}_1$ decays via $b-$jet, two different fermions f and the neutralino $\tilde{\chi}_1^0$ known as the four body decay channel bffN, as seen in Feynman diagram in Figure 2.8 right.

The leptons in the final state, originating from the off-shell W boson decay, are expected to have very low p_T. To compensate this, a high transverse momentum jet from an initial state radiation (ISR) is required to boost the system in the opposite hemisphere enhancing a E_T^{miss} value expected from the two LSPs, as shown in Figure 8.1. By this the final states expected are a high-p_T ISR, a soft lepton (e or μ), jets and a huge amount of undetected energy.
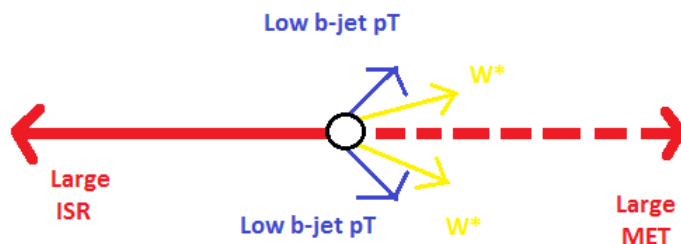
Figure 8.1 Illustration showing the required ISR jet to boost the system and obtain the required E_T^{miss}. The resulting objects are soft (low p_T) including the soft lepton selected from the off-shell W boson.

	bffN
	soft-lepton
Preselection	
Leading jet p_T (no $b-$ tagged)	> 400 GeV
E_T^{miss}	>300 GeV
m_T	< 160 GeV
p_T^{lep}/E_T^{miss}	< 0.02
$\min(\Delta\phi(\vec{p}_T^{\,miss}, b-\text{jet}))$	< 1.5

Table 8.1 Event selection defining the kinematic variables for the bffN signal region in the current analysis [87]. The soft preselection in table 5.2 was applied.

8.2 Motivation

In the current stop 1L analysis, no dedicated signal region for the 4-body decay channel was developed. Instead, since the bffN signature is very similar to Higgsino (see Fig 2.7 right and 2.8 right) with a single soft-lepton, this soft-lepton Higgsino SR was used for the bffN search, named bC soft diagonal [87].

8.2.1 Current Status

The preselection described in Section 5.3 Table 5.2 is used for the current analysis. A requirement on the $\min(\Delta\phi(\vec{p}_T^{\,miss}), b-\text{jet}))$ was set to reduce $W+$ jets background, resulting in a leading background of semileptonic $t\bar{t}$ events. The variables p_T^{lep}/E_T^{miss}, $m_{top}^{reclustered}$ have been introduced and explained in more detail in section 5.2. The selection for the bffN SR is shown in Table 8.1.

At first the results seemed promising, and sharing the information from the bC soft diagonal SR seemed sufficient. A total background event yield of ~ 66 and a signal event yield of ~ 65 for the mass point $m(\tilde{t}_1, \tilde{\chi}_1^0)=(350,300)$ GeV [87] was obtained. Afterwards, it was noticed that the proper efficiency filter was not applied in the first set of samples, and when fixing the problem a reduction of a factor of 3 in the cross section for the bffN was obtained. So the results were not promising anymore, leading to the results shown in Figure 8.2, describing the obtained event yields with the correct samples. The significance Z^1 lead to a number of 0.836. The main background obtained with this selection is $t\bar{t}$1L ($\sim 34\%$) as shown in the pie chart. Figure 8.3 and 8.4 shows the distributions of the main kinematic variables and the n-1 plots for the samples with the proper efficiency filter into account. The bffN mass points used were $m(\tilde{t}_1, \tilde{\chi}_1^0)=(350,270)$, (350,300) and (400,350) GeV.

---

[1]Explain in more detail in the next subsection 8.2.2.

bffN	el	mu	total
$t\bar{t}$ 2L	1.40 ± 0.48	3.23 ± 0.24	4.63 ± 0.54
$t\bar{t}$ 1L1τ	1.66 ± 0.17	5.58 ± 0.29	7.24 ± 0.34
$t\bar{t}$ 1L	4.85 ± 0.28	18.29 ± 0.69	23.14 ± 0.74
W+jets	3.51 ± 0.38	13.36 ± 1.10	16.87 ± 1.17
Single top	3.09 ± 1.10	7.22 ± 1.09	10.31 ± 1.55
Diboson	0.16 ± 0.07	2.56 ± 1.62	2.72 ± 1.62
Total SM	14.66 ± 1.31	50.24 ± 2.38	64.91 ± 2.71
bffN_350_300	4.51 ± 1.73	15.57 ± 2.15	20.08 ± 2.76
Significance Z			0.836
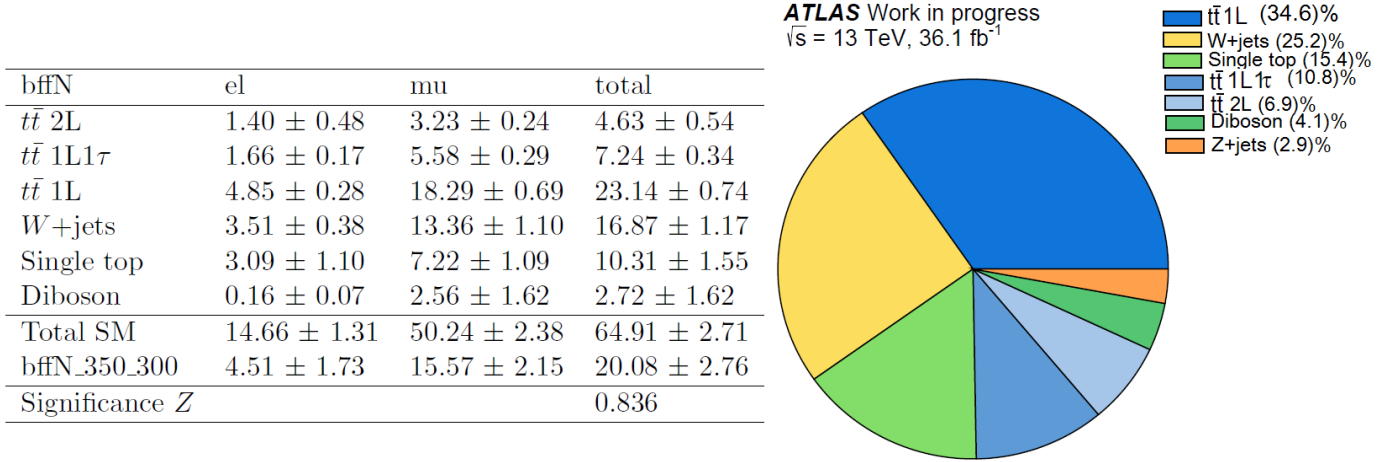
Figure 8.2 On the left the event yield table of the expected number of events for an integrated luminosity of 36.1 fb^{-1} after applying the selection in Table 8.1 is presented. It corresponds to the results in the current analysis after the correct filter efficiency was applied. It is divided in the number of yields in the electron (el) and muon (mu) channel. bffN_350_300 stands for the signal mass point m($\tilde{t}_1, \tilde{\chi}^0_1$)=(350,300) GeV. The significance calculation Z is given in he last row and explained in section 8.2.2. On the right the breakdown of the main SM background processes is shown.
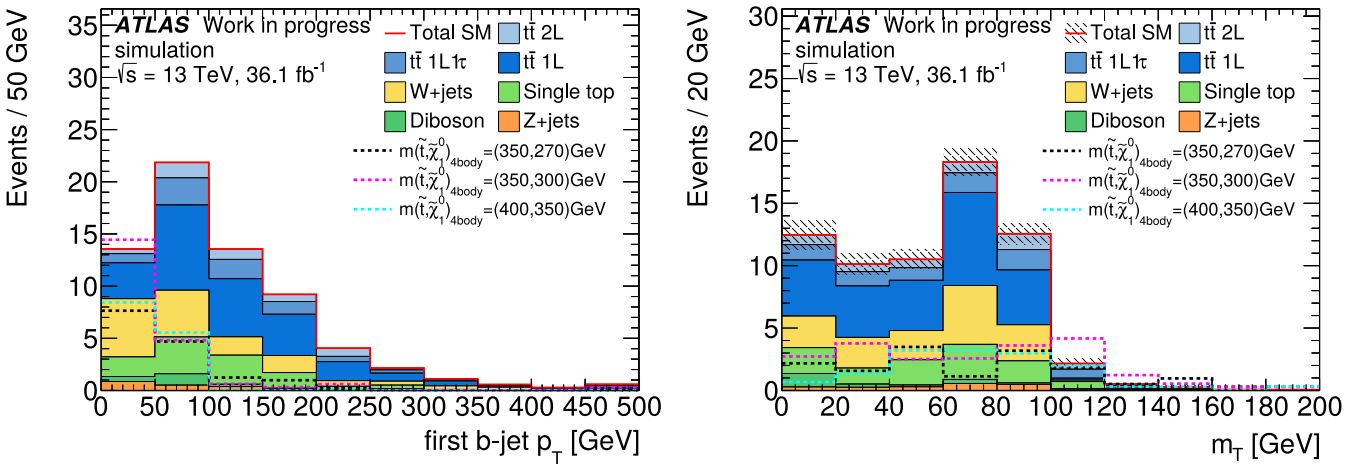
Figure 8.3 Distributions of the main kinematic variables after applying the selection of the current analysis (see Table 8.1). The proper filter efficiency is taken into account.
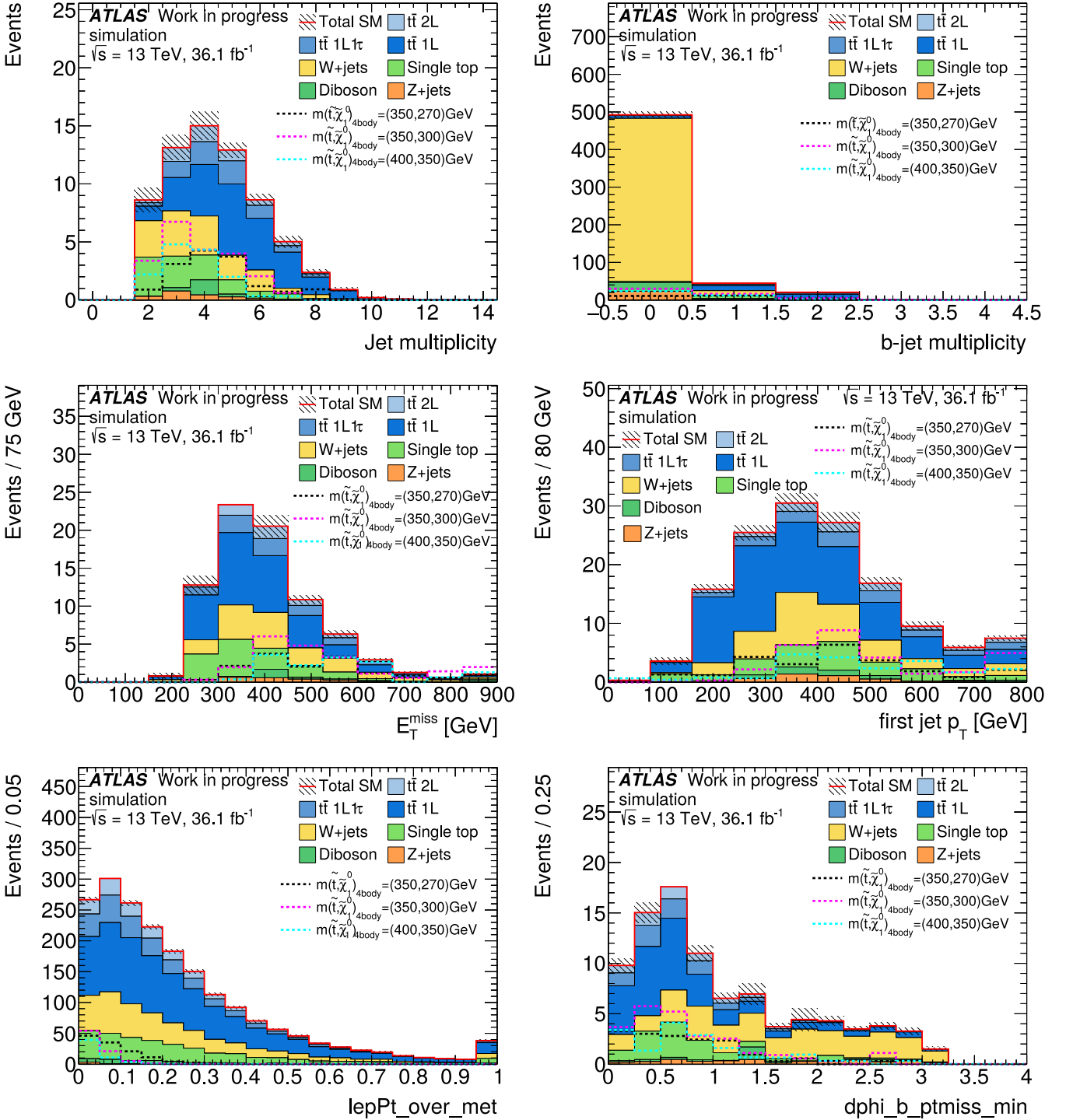
Figure 8.4 Distributions of the main kinematic variables after applying the selection of the current analysis (see Table 8.1), except for the requirement that is imposed on the variable being plotted. The proper filter efficiency is taken into account.

	bffN Current	bffN First Idea
Preselection	soft-lepton	soft-lepton
Leading jet p_T (no $b-$ tagged)	> 400 GeV	> 400 GeV
E_T^{miss}	>300 GeV	>300 GeV
m_T	< 160 GeV	—
p_T^{lep}/E_T^{miss}	< 0.02	<0.1
$\min(\Delta\phi(\vec{p}_T^{miss}, b-\mathrm{jet}))$	< 1.5	< 0.5
First $b-$jet p_T	—	< 50 GeV

Table 8.2 Event selection defining bffN signal region in the actual analysis [87] and comparing it to the first idea of optimization.

8.2.2 Improved Selection

After noticing the previous significance problem, new studies looking for a dedicated SR for the 4-body region were performed. We came with a preliminary idea, by analyzing the n-1 plots distributions, of the following: to relax the variable p_T^{lep}/E_T^{miss}, to omit the m_T cut, tighten the $\min(\Delta\phi(\vec{p}_T^{miss}, b-\mathrm{jet}))$ variable to get rid of W+jets background, and to require the first $b-$jet p_T to be below 50 GeV. With this new selection as shown in Table 8.2, significant better results were obtained. The mass points taken to test were $m(\tilde{t}_1, \tilde{\chi}_1^0)=(350,270)$, $(350,300)$ and $(400,350)$ GeV as shown in the n-1 plots in Figure 8.5, showing the distributions of the main kinematic variables and the signal contribution.

One comon criteria used in several analyses to define a SR, is to find the best achiavble significance Z in the SR. As in this model we have low signal and background event rates expected in the SR, the background needs to be described by a Poisson distribution (see 6.5.1) [144]. To obtain a more accurate value of Z, its value is determined taking also into account the uncertainties on background events, explained in more detail in [147]. For the bffN optimization studies, we took a flat 30% of background relative uncertainty (Δb_{rel}). The calculation of Z is implemented by ROOT software framework [148]. The function is defined as [149]:

$$\texttt{RooStats::NumberCountingUtils::BinomialExpZ}(s, b, \Delta b_{rel}) \qquad (8.1)$$

with s the number of signal event yields and b of the background. With this tool used for the Z calculation, the significance with this first idea is improved to $Z= 1.370$ as shown in Figure 8.4 left. The contribution of the main SM backgrounds is also seen in the pie chart at the right. We can appreciate that after this selection we have more W+jets background events ($\sim$34%).

After realizing that an improvement in Z is feasible, deeper studies were made focusing on optimizing the SR. Studies looking at different possible discriminating variables were performed using an optimization tool. This tool created by a member of our group, have as an input the main and possible discriminating variables with a loose selection. Then the tool is performed and it search through all permutations of the different cuts on the variables, for the cut combination with the optimal result of all, i.e. the best significance Z value.

bffN First Idea	el	mu	total
$t\bar{t}$ 2L	0.83 ± 0.19	0.95 ± 0.14	1.78 ± 0.24
$t\bar{t}$ 1L1τ	1.17 ± 0.15	2.32 ± 0.23	3.49 ± 0.27
$t\bar{t}$ 1L	3.49 ± 0.27	6.04 ± 0.42	9.53 ± 0.50
W+jets	4.99 ± 0.44	6.45 ± 0.61	11.44 ± 0.76
Single top	1.89 ± 0.49	3.22 ± 0.78	5.11 ± 0.92
Diboson	1.17 ± 0.69	0.84 ± 0.54	2.01 ± 0.88
Total SM	13.53 ± 1.02	19.83 ± 1.24	33.36 ± 1.60
bffN_350_300	8.85 ± 2.02	15.25 ± 2.31	24.10 ± 3.07
Significance Z			1.370
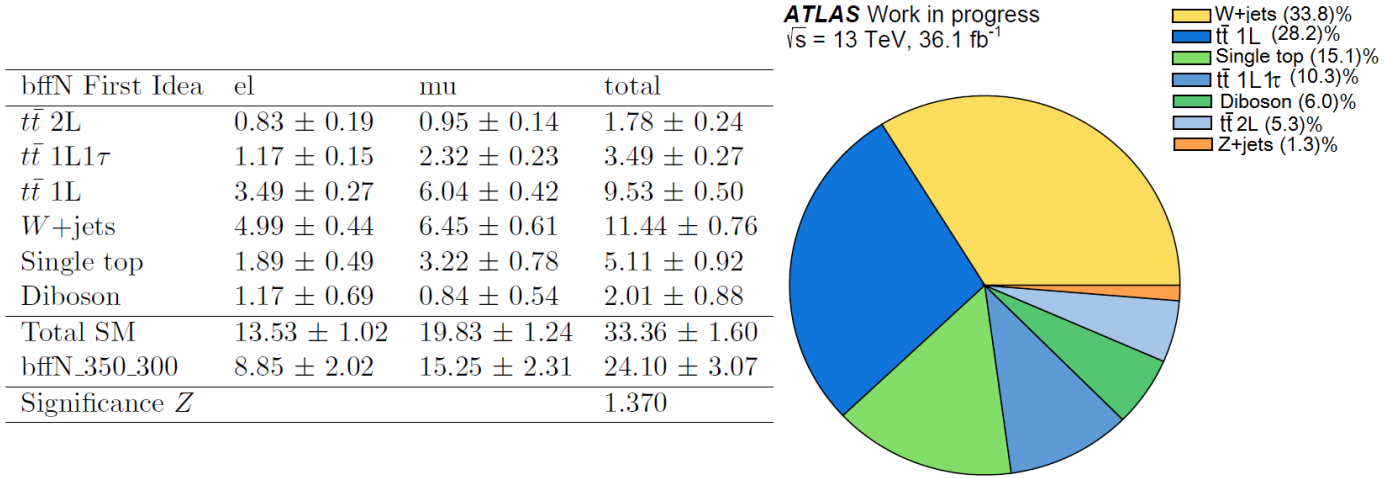
Figure 8.4 On the left the event yield table of the expected number of events for an integrated luminosity of 36.1 fb^{-1} after applying the selection in Table 8.2. It corresponds to the first idea of optimization. It is divided in the number of yields in the electron (el) and muon (mu) channel. bffN_350_300 stands for the signal mass point m($\tilde{t}_1, \tilde{\chi}_1^0$)=(350,300) GeV. The significance calculation Z is given in he last row.p On the right the breakdown of the main SM background processes is shown.
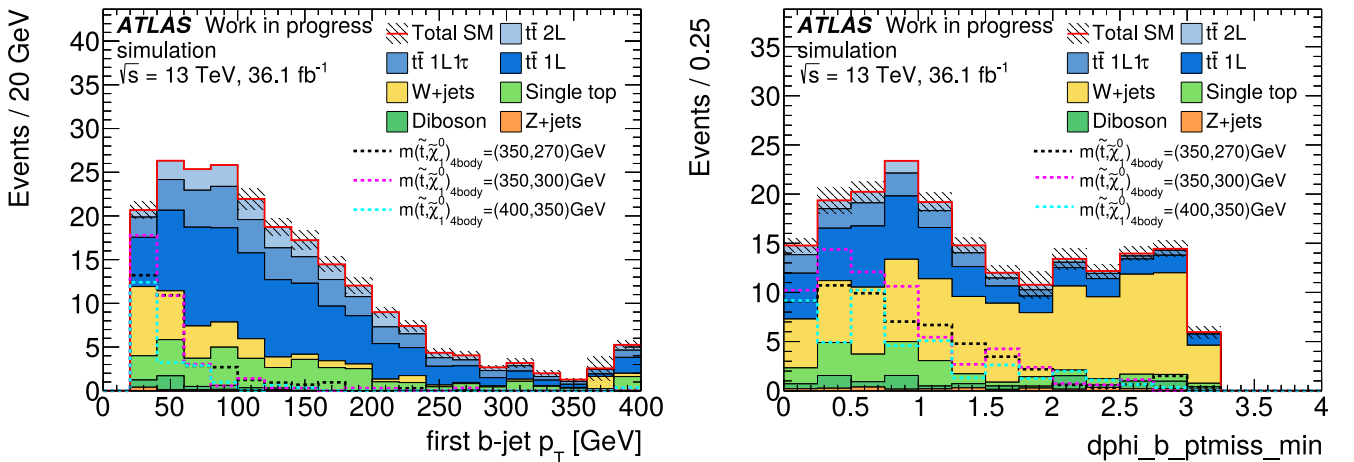
Figure 8.5 Distributions of the main kinematic variables after applying the selection of Table 8.2, except for the requirement that is imposed on the variable plotted.
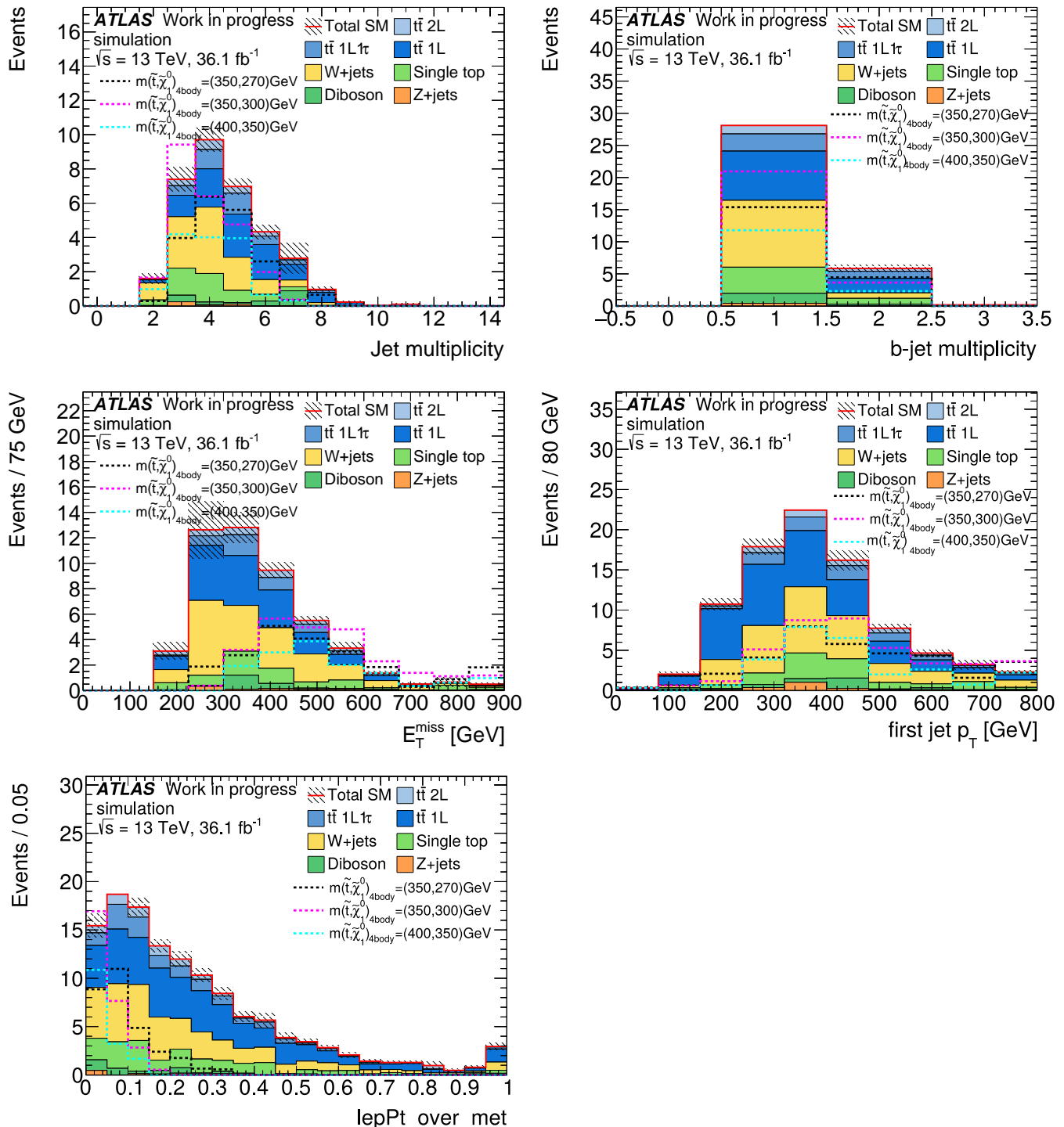
Figure 8.5 Distributions of the main kinematic variables after applying the selection of Table 8.2, except for the requirement that is imposed on the variable being plotted.

	bffN Current	bffN Optimal Idea
Preselection	soft-lepton	soft-lepton
Leading jet p_T (no $b-$ tagged)	> 400 GeV	> 400 GeV
E_T^{miss}	>300 GeV	>350 GeV
m_T	< 160 GeV	> 100 GeV
p_T^{lep}/E_T^{miss}	< 0.02	<0.1
$\min(\Delta\phi(\vec{p}_T^{\,miss}, b-\text{jet}))$	< 1.5	< 1.5
First $b-$jet p_T	—	< 70 GeV

Table 8.3 Events selections defining bffN signal region in the actual analysis [87] and comparing it to the optimal result.

In this preliminary studies the presented kinematic variables in table 8.3 were used as an input in the tool and two extra ones: H_T and MET_{sig}[2]. The best result found is presented in Table 8.3 showing the selection on the discriminanting variables. A requirement on m_T was suggested. The first $b-$jet p_T and the p_T^{lep}/E_T^{miss} requirements are relaxed, compared to the current selection. With this selection we reach a significance of $Z = 3.286$, taking the event yields from Figure 8.6 and the mass point m$(\tilde{t}_1, \tilde{\chi}_1^0)$=(350,270) GeV. The breakdown of the main SM background contributions is shown and we can see that the main background is now dileptonic $t\bar{t}$ ($\sim$67%). In the n-1 plots in Figure 8.7 also the mass points for m$(\tilde{t}_1, \tilde{\chi}_1^0)$ = (350,300) and (400,350) GeV are shown.

For the other mass points tested in this optimal region, the significances obtained were: for m$(\tilde{t}_1, \tilde{\chi}_1^0)$=(350,300) GeV a Z value of 2.508 (which in the current analysis is $Z \sim$0.836 with the same mass point), and for m$(\tilde{t}_1, \tilde{\chi}_1^0)$=(400,350) GeV a Z value of 1.45. We can see that when the mass difference Δm between the stop and the neutralino is closer to 80 GeV (to the W boson mass) the mass point is well optimized. In this region the average lepton momentum increases and a soft $b-$jets can be reconstructed. When Δm is smaller, the lepton momentum is even lower and the reconstruction of the variables could not enter the acceptance.

---

[2]These variables are not further described because their performance after using the toll was not optimal, so we did not take them for this studies. H_T is the negative sum of jets and lepton vectors and MET_{sig} is $E_T^{miss}/\sqrt{H_T}$.

None	el	mu	total
$t\bar{t}$ 2L	1.42 ± 0.13	1.98 ± 0.19	3.39 ± 0.23
$t\bar{t}$ 1L1τ	2.27 ± 0.18	3.18 ± 0.20	5.45 ± 0.27
$t\bar{t}$ 1L	0.23 ± 0.09	0.27 ± 0.05	0.50 ± 0.10
W+jets	0.41 ± 0.12	0.76 ± 0.19	1.18 ± 0.22
Single top	0.48 ± 0.20	0.96 ± 0.24	1.44 ± 0.31
Diboson	0.74 ± 0.29	0.47 ± 0.08	1.20 ± 0.30
Total SM	5.55 ± 0.44	7.62 ± 0.42	13.17 ± 0.61
bffN_350_270	8.00 ± 1.48	17.64 ± 2.58	25.63 ± 2.97
Significance Z			3.286
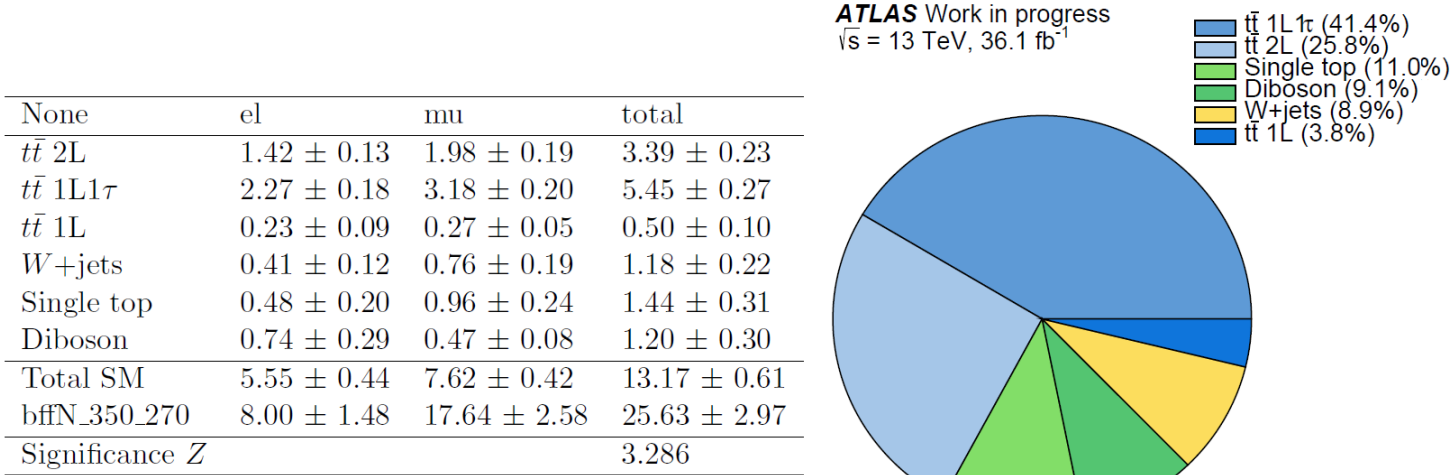
Figure 8.4 Event yield table of the expected events at 36.1 fb^{-1} after applying the selection in Table 8.3, as the optimal result obtained so far. It is divided in the number of yields in the electron (el) and muon (mu) channel. bffN_350_270 stands for the signal mass point m($\tilde{t}_1$, $\tilde{\chi}_1^0$)=(350,270) GeV. On the right the breakdown of the main SM background processes is shown.
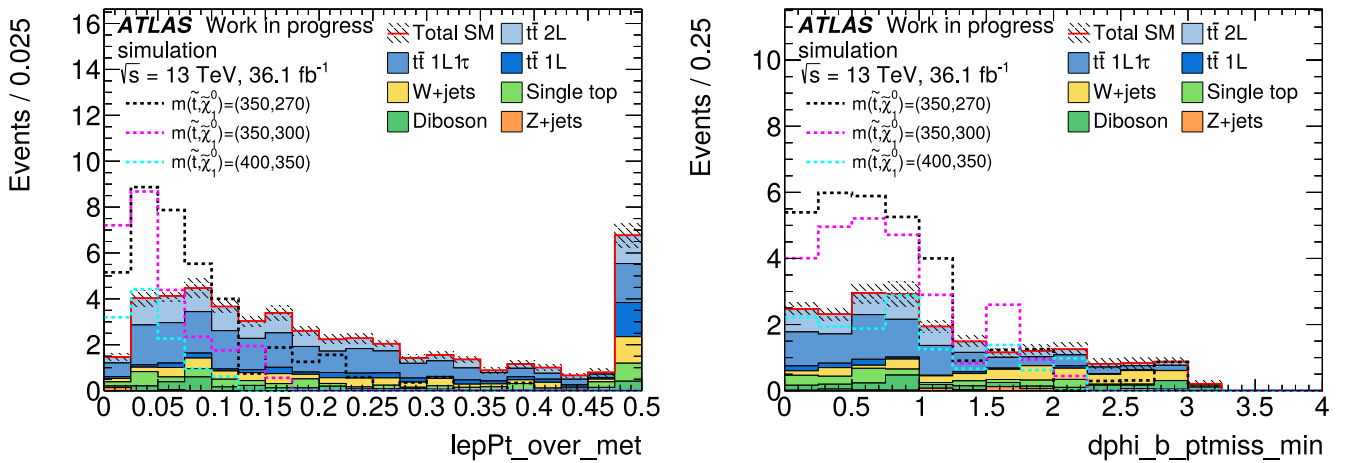
Figure 8.7 Distributions of the main kinematic variables after applying the selection of Table 8.3, except for the requirement that is imposed on the variable being plotted.
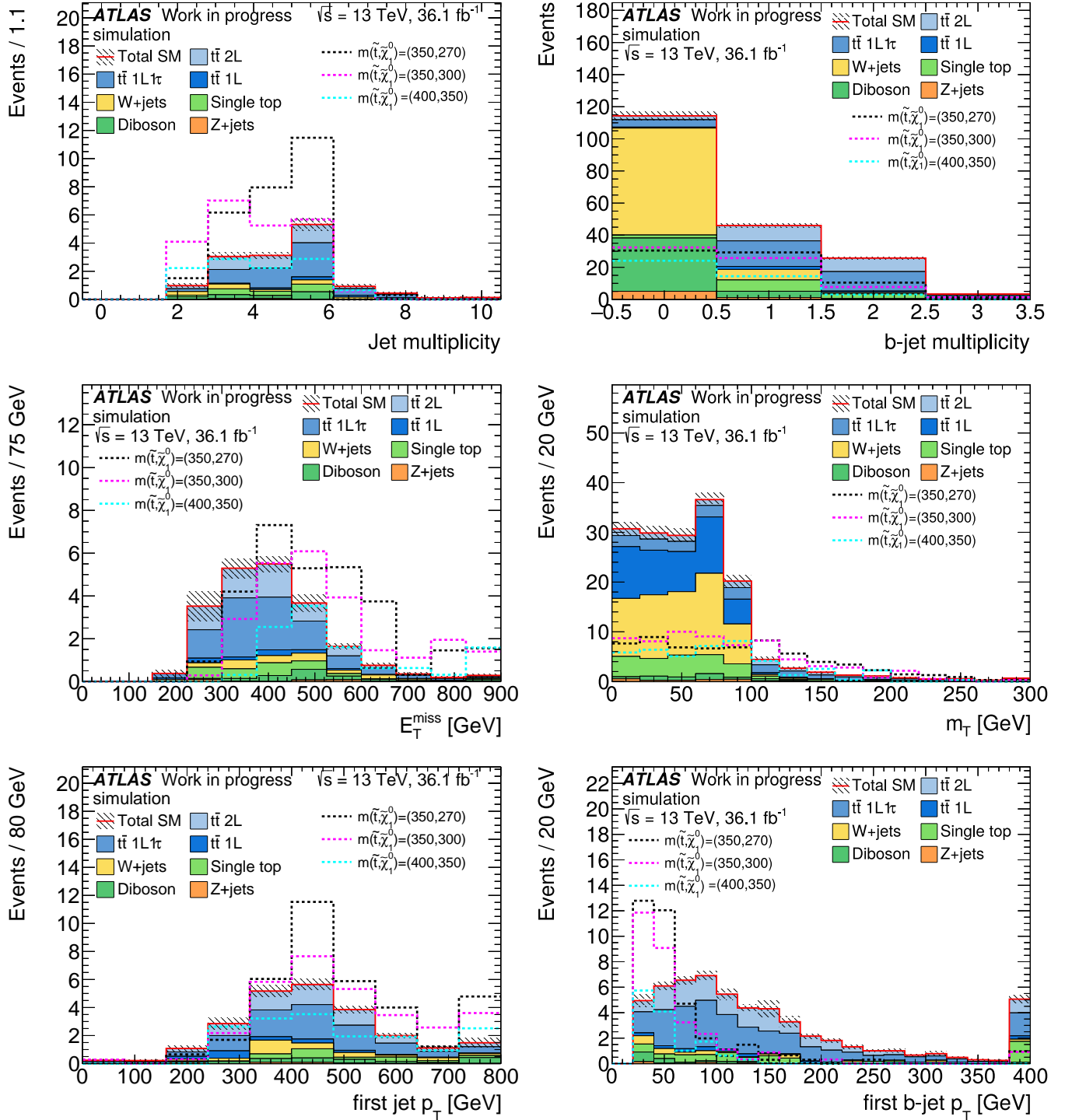
Figure 8.7 Distributions of the main kinematic variables after applying the selection of Table 8.3, except for the requirement that is imposed on the variable being plotted.

Chapter 9

Conclusion and Outlook

If SUSY exists, it must be spontaneously broken. Such broken symmetry would solve many problems, for example, the fine-tuning problem of the Higgs boson mass. A direct confirmation of the existence of SUSY would be the production of SUSY partners (sparticles) of existing particles in the proton-proton collisions at the LHC.

A light stop is motivated by natural SUSY in which the stop should cancel the large radiative correction from the top quark to the Higgs boson mass. This thesis presented a search for evidence of the stop pair production. The searches were performed requiring at the final state of a signal event one electron or muon, one neutrino originating from the decay of an on- or off-shell W boson, two b quarks (reconstructed as b jets), two light-flavor quarks and two lightest supersymetric particles (LSPs). The LSPs are not interacting with the detector material and cause large missing transverse energy (E_T^{miss}) together with the neutrino. Therefore, the event selection in the analysis requires exactly one isolated electron or muon, E_T^{miss} and at least one b-jet. Using 36.fb^{-1} of data taken with the ATLAS detector throughout 2015 and 2016 at a center of mass energy $\sqrt{s}$=13TeV. No excess in data over the SM predictions is found.

The analysis presented, considered the pure bino LSP simplified model of the stop decay scenario. It focused on two different regions in the supersymmetric parameter space, exhibiting small mass differences between the stop and the neutralino $\Delta m = m_{\tilde{t}_1} - m_{\tilde{\chi}_1^0}$. When $\Delta m < m_{top}$, we had a three-body decay (bWN), where the stop $\tilde{t}_1$ undergoes via a b quark, a W boson and a neutralino $\tilde{\chi}_1^0$. When Δm is less than the mass of the W boson, the stop decays via the 4-body channel (bffN) via b quark, two different fermions f and a neutralino $\tilde{\chi}_1^0$.

In the current three-body decay analysis [87], only one control region (CR) for the main dileptonic $t\bar{t}$ background was defined. Extended studies from the current analysis were presented here, developing dedicated control regions and validation regions (VR) for the other sub-leading backgrounds. The CRs were defined using different kinematic variables properties, to ensure a small extrapolation to the SR, while keeping the background purity high. Constraining the background with more than one region helped to identified variables for getting highly enriched backgrounds samples. This information is also useful for future analyses. When performing the statistical inference using the statistical and the systematic uncertainties with the extra defined regions, a significant improvement compared to the current analysis was shown. In particular, in the bWN signal region (SR), a better agreement between data and the background estimates was obtained. A reduction of $\sim 50\%$ in the background systematic uncertainty, using the background estimate from

all the regions, was achieved. As no significant excess of data over SM background expectation was observed, the exclusion limits were set. The contour plots showed a gain in the exclusion mass points, covering more phase space in the 3-body decay diagonal than the current status, enclosing 50 GeV more in the stop mass and 20 GeV in the neutralino mass.

For the other region studied, the 4-body channel, no signal region in the current analysis was defined. Instead a Higgsino scenario with a soft lepton was used, which seemed to have good sensitivity in the bffN region. After fixing the filter efficiency problem in the Monte Carlo (MC) samples, the cross section was reduced by a factor of three and the sensitivity in this phase space dropped. With this motivation, preliminary studies for defining a signal region with a better sensitivity were presented. We tested the simple kinematic variables used at the beginning to define SR, and extra ones to find better optimization results. After using an optimization tool to calculate the best significance (Z) in the SR, an improvement was found. The Z value in the current analysis is $\sim$0.83, and in the optimal region found in this studies the Z value increases to $\sim$2.41, with the same mass point ($\mathrm{m}(\tilde{t}_1, \tilde{\chi}_1^0)$=(350,300) GeV). A better significance was found for a mass point with a mass difference closer to the mass of the W boson ($\mathrm{m}(\tilde{t}_1, \tilde{\chi}_1^0)$=(350,270) GeV) with $Z \sim$3.29. After the results, we can conclude that defining a bffN signal region with sufficient statistics is possible. With lower Δm we have seen issues that need to be further studied. More sensitivity studies are required, targeting other possible regions (like b-veto), in order to find the most optimal result. Further work testing possible discriminating kinematic variables used in other analyses is needed.

Bibliography

[1] ATLAS Collaboration. Observation of a new particle in the search for the Standard Model Higgs boson with the ATLAS detector at the LHC. Phys.Lett. B716 (2012)1-29,2012. arXiv:1207.7214 [hep-ex].

[2] CMS Collaboration. "Observation of a New Boson at a Mass of 125 GeV with the CMS Experiment at the LHC". Phys. Lett. B **716** (2012) 30. `arXiv:1207.7235v2[hep-ex]`.

[3] Rayleigh (1941). "Joseph John Thomson. 1856-1940". Obituary Notices of Fellows of the Royal Society. London: Royal Society. **3** (10): 586-609. doi:10.1098/rsbm.1941.002

[4] S. F. Novaes. "Standard Model: An Introduction". `arXiv:hep-ph/0001283v1[hep-ph]`.

[5] David Griffiths. "Introduction to Elementary Particle Physics". Wiley-VCH,2008. Section 2.3 Quantumchromodynamics (QCD), pp: 61-64.

[6] David Griffiths. "Introduction to Quantum Mechanics". Pearson Prentice Hall,2005. Second edition.

[7] C. Patrignani et al. (Particle Data Group), Chin. Phys. C, **40**, 100001 (2016) and 2017 update. Physical Constants. `http://pdg.lbl.gov/2017/reviews/rpp2016-rev-phys-constants.pdf`

[8] O. Cremonesi. "Neutrino Masses". PoS **EPS-HEP2013** (2014) 146.

[9] C. Patrignani et al. (Particle Data Group), Chin. Phys. C, **40**, 100001 (2016) and 2017 update. Online: `http://pdg.lbl.gov/2017/tables/rpp2017-sum-gauge-higgs-bosons.pdf`.

[10] C. Patrignani et al. (Particle Data Group), Chin. Phys. C, **40**, 100001 (2016) and 2017 update. `http://pdg.lbl.gov/2017/tables/rpp2017-sum-leptons.pdf`

[11] C. Patrignani et al. (Particle Data Group), Chin. Phys. C, **40**, 100001 (2016) and 2017 update. `http://pdg.lbl.gov/2017/tables/rpp2017-sum-quarks.pdf`

[12] David Griffiths. "Introduction to Elementary Particle Physics". Wiley-VCH,2008.

[13] M. E. Peskin and D. V. Schroeder. "An Introduction to Quantum Field Theory". Westview Press, 1995.

[14] David Griffiths. "Introduction to Elementary Particle Physics". Wiley-VCH,2008. Chapter 10 pp. 319-322

[15] D. Schaile. Lecture Notes on "Advanced Particle Physics". 2015. LMU Munich. Chapter 6.

[16] M. Thomson. "Particle Physics". University of Cambridge. Lectures 2009. On-line: Online: `http://www.hep.phy.cam.ac.uk/~thomson/lectures/partIIIparticles/Handout7_2009.pdf`.

[17] J.D.Walecka. "Advanced Modern Physics: Theoretical Foundations". World Scientific Publishing Co.2011. Section 6.3.1.2 Isospinor, pp.131-133.

[18] C. S. Wu, E. Ambler, R. W. Hayward, D. D. Hoppes, and R. P. Hudson. "Experimental Test of Parity Conservation in Beta Decay". Phys. Rev. **105**, 1413. `https://journals.aps.org/pr/abstract/10.1103/PhysRev.105.1413`

[19] H. Frauenfelder, J. D. Jackson, and H. W. Wyld, Jr. "Polarization Effects following Beta Decay". Phys. Rev. **110**, 451. 15 April 1958. Online: `https://journals.aps.org/pr/abstract/10.1103/PhysRev.110.451`.

[20] D. Schaile. Lecture Notes on "Advanced Particle Physics". 2015. LMU Munich. Chapter 1.

[21] M.Thomson. "Modern Particle Physics". New York: Cambridge University Press, 2013. `ISBN: 9781107034266`.

[22] David Griffiths. "Introduction to Elementary Particle Physics". Wiley-VCH,2008. Section 10.7.3 Electro-Weak Mixing. pp. 336.

[23] David Griffiths. "Introduction to Elementary Particle Physics". Wiley-VCH,2008. Chapter 9. pp 279.

[24] F.Mandl and G.Shaw. "Quantum Field Theory". John Wiley & Sons Ltd. Second edition. 2010.

[25] C.R. Nave. "The Color Force". HyperPhysics. Georgia State University, Department of Physics.

[26] R.D.Klauber. "Electroweak Symmetry Breaking". University notes. Online:`http://www.quantumfieldtheory.info/Electroweak_Sym_breaking.pdf`.

[27] P. W. Higgs. "Broken Symmetries and the Masses of Gauge Bosons". Phys. Rev. Lett. **13** (1964) 508-509.

[28] F. Englert and R. Brout. "Broken Symmetry and the Mass of Gauge Vector Mesons". Phys. Rev. Lett. **13** (1964) 321-323.

[29] C. Patrignani et al. (Particle Data Group), Chin. Phys. C, **40**, 100001 (2016) and 2017 update. Online: `http://pdg.lbl.gov/2017/tables/rpp2017-sum-gauge-higgs-bosons.pdf`.

[30] W. de Boer. "The Discovery of the Higgs Boson with the CMS Detector and its Implications for Supersymmetry and Cosmology". *Time and Matter* 2013 (TAM2013). Italy. Online: `https://inspirehep.net/record/1252561/files/arXiv:1309.0721.pdf`.

[31] G.'t Hooft. "Naturalness, Chiral Symmetry and Spontaneous Chiral Symmetry Breaking". NATO Sci.Ser.B **59** (1980) 135-157 PRINT-80-0083 (UTRECHT). Online: `http://inspirehep.net/record/144074/references?ln=es`.

[32] S.P. Martin. "A Supersymmetry Primer". hep-ph/9709356, version 7, January 2016.

[33] F. Zwicky, "Die Rotverschiebung von extragalaktischen Nebeln", Helv. Phys. Acta 6,110-127 (1933).Published online: 18 November 2008. DOI 10.1007/s10714-008-0707-4. Online: `http://www.ymambrini.com/My_World/History_files/Zwicky.pdf`

[34] K. Garrett and G. Duda. :Dark Matter: A Primer". Adv. Astron. 2011 (2011), p. 968283. `arXiv:1006.2483[hep-ph]`.

[35] E. Corbelli and P. Salucci, "The Extended Rotation Curve and the Dark Matter Halo of M33", *Monthly Notices of the Royal Astronomical Society*, vol. 311, no. 2, pp. 441-447, 2000. Online: `http://mnras.oxfordjournals.org/content/311/2/441.abstract`

[36] Dyson F., Eddington A. and Davidson C., "A Determination of the Deflection of Light by the Sun's Gravitational Field, from Observations Made at the Total Eclipse of May 29, 1919". Phil. Trans. Roy. Soc. 220 291

[37] R. Massey, T. Kitching, and J. Richard, "The Dark Matter of Gravitational Lensing".`arXiv:1001.1739`.

[38] D.Clowe et.al. "A Direct Empirical Proof of the Existence of Dark Matter". Astrophys.J.648:L109-L113, 2006. `arXiv:astro-ph/0608407`.

[39] ESA and the Planck Collaboration Collaboration. "Simple but Challenging: The Universe According to Planck". (2016) . Online: `http://sci.esa.int/jump.cfm?oid=51551`

[40] D. Scott, "The Standard Cosmological Model". `arXiv:astro-ph/0510731` .

[41] David J. Gross, H. David Politzer, Frank Wilczek. The Nobel Prize in Physics 2004. Popular Information. Online: `https://www.nobelprize.org/nobel_prizes/physics/laureates/2004/popular.html`

[42] J. Conlon, "Introduction to Supersymmetry (lecture notes)". Online: `https://www-thphys.physics.ox.ac.uk/people/JosephConlon/LectureNotes/SUSYLectures.pdf`

[43] M. Bustamante, L. Cieri, and J. Ellis, "Beyond the Standard Model for Montañeros". arXiv:0911.4409

[44] K. Inoue et al.,"Aspects of Grand Unified Models with Softly Broken Supersymmetry". Prog. Theor. Phys. **68** (1982) 927.

[45] I. J. R. Aitchison, "Supersymmetry and the MSSM: An Elementary Introduction". `arXiv:hep-ph/0505105`.

[46] N. R. Shah. "Minimal Supersymmetric Standard Model". (Lecture Notes). Online: `//theory.uchicago.edu/~sethi/Teaching/P487-S2003/MSSMnausheen.pdf`.

[47] R. Barbieri and G. Giudice. "Upper Bounds on Supersymmetric Particle Masses" Nucl.Phys. **B306** (1988) 63.

[48] K. Rolbiecki, J. Tattersall, and G. Moortgat-Pick. "Towards Measuring the Stop Mixing Angle at the LHC". Eur.Phys.J. **C71** (2011) 1517. `arXiv:0909.3196[hep-ph]`.

[49] C. Patrignani et al. (Particle Data Group), Chin. Phys. C, **40**, 100001 (2016) and 2017 update. `http://pdg.lbl.gov/2017/listings/rpp2017-list-p.pdf`

[50] Image from `http://www.quantumdiaries.org/tag/ckm/`

[51] P.Fayet. "The Supersymmetric Standard Model". Eur. Phys. J. **C** (2014) 74: 2837 `https://doi.org/10.1140/epjc/s10052-014-2837-z`.

[52] C. Patrignani et al. (Particle Data Group), Chin. Phys. C, **40**, 100001 2016 revision. "Supersymmetry, Part I (Theory)". H. E. Haber. Online: `http://pdg.lbl.gov/2017/reviews/rpp2016-rev-susy-1-theory.pdf`

[53] I. J. R. Aitchison. "Supersymmetry and the MSSM: an Elementary Introduction". `arXiv:hep-ph/0505105v1`. 12 May 2005

[54] N. R. Shah. "Minimal Supersymmetric Standard Model (lecture notes)". Online: `http://theory.uchicago.edu/~sethi/Teaching/P487-S2003/MSSMnausheen.pdf`

[55] Aad, Georges et al. "Search for Top Squark Pair Production in Final States with One Isolated Lepton, Jets, and Missing Transverse Momentum in $s = \sqrt{8}$ TeV pp Collisions with the ATLAS Detector". Phys. Rev. D 94, 052009 (2016). `arXiv:1606.03903[hep-ex]`

[56] N.Arkani-Hamed, A.Delgado and G.FGiudice. "The Well-Tempered Neutralino". Nucl.Phys **B741** (2006) 108, `arXiv:hep-ph/0601041[hep-ph]`.

[57] SUSY Feynman Diagram tN. `https://twiki.cern.ch/twiki/bin/viewauth/AtlasProtected/SUSYFeynmanDiagramsstst-ttN1N1`

[58] SUSY Feynman Diagram tCN. `https://twiki.cern.ch/twiki/bin/viewauth/AtlasProtected/SUSYFeynmanDiagramsstst-bbWWN1N`

[59] ATLAS Note. "Search for Top Squarks in Final States with One Isolated Lepton, Jets, and Missing Transverse Momentum in $\sqrt{s}$ =13TeV collisions using 36.1 fb^{-1} of ATLAS data". ATL-COM-PHYS-2016-1623. Draft version 0.6.

[60] F.Cachazo et al. "A Deeper Dive: On-Shell and Off-Shell" Description of the paper given by the Perimeter Institute of Theoretical Physics. Online: `www.perimeterinstitute.ca/news/new-face-feynman-diagrams/deeper-dive-shell-and-shell`

[61] SUSY Feynman Diagrams bWN. `https://twiki.cern.ch/twiki/bin/viewauth/AtlasProtected/SUSYFeynmanDiagramsstst-blvbqqN1N1-3body`

[62] SUSY Feynman Diagrams bffN. `https://twiki.cern.ch/twiki/bin/viewauth/AtlasProtected/SUSYFeynmanDiagramsstst-bffbffN1N1-4body`

[63] CERN Homepage. Online: `https://home.cern/about`

[64] CERN Homepage. Pulling together: Superconducting electromagnets. Online: `https://home.cern/about/engineering/pulling-together-superconducting-electromagnets`

[65] S. Schael et al. "Precision Electroweak Measurements on the Z Resonance". `arXiv:hep-ex/0509008` [hep-ex]. 2016.

[66] Lyndon Evans and Philip Bryant. "LHC Machine". 2008. Online: `http://stacks.iop.org/1748-0221/3/i=08/a=S08001`

[67] O. Bruning et al. "LHC Report". CERN Yellow Reports: Monographs. 2004. Online: `https://cds.cern.ch/record/782076`

[68] CERN Accelerator Complex (operating and approved projets). LHC-PHO-1991-001. Online: `https://cds.cern.ch/record/841493`

[69] CERN. LHC Overview of four main experiment. Online: `https://www.aec.at/aeblog/en/2015/06/19/lhc-mother-of-all-experiments/`

[70] ATLAS webpage. Online: `http://atlas.cern/discover/about`.

[71] CMS webpage. Online: `https://cms.cern/`.

[72] ALICE webpage. Online: `http://aliceinfo.cern.ch/Public/Welcome.html`.

[73] LHCb webpage. Online: `http://lhcb-public.web.cern.ch/lhcb-public/`.

[74] W.Herr and B.Muratori. "Concept of Luminosity". CERN 2006. CERN Document Server. Online: `https://cds.cern.ch/record/941318/files/p361.pdf`

[75] K.A Olive et al. (Particle Data Group). Chin. Phys. C,38, 90001, 2014.

[76] "ATLAS Detector and Physics Performance: Technical Design Report, 1". CERN 1999. Online: `https://cds.cern.ch/record/391176/files/cer-0317330.pdf`

[77] ATLAS Collaboration. "Studies of the Performance of the ATLAS Using Cosmic-Ray Muons".Eur. Phys. J. **C71** (2011). `arXiv:1011.6665`

[78] J. Pequenao. "Event Cross Section in a Computer Generated Image of the ATLAS Detector".CERN-GE-0803022. 2008.

[79] ATLAS Collaboration. "The ATLAS Experiment at the CERN Large Hadron Collider". 2008 JINST 3 S08003.

[80] E.Daw. "Lecture 7. Rapidity and Pseudorapidity" The University of Sheffield. 2012. Online: `http://www.hep.shef.ac.uk/edaw/PHY206/Site/2012_course_files/phy206rlec7.pdf`

[81] Y.Abulati. "Search for Pair-Produced Supersymmetric Top Quark Partners with the ATLAS Experiment". Stockholm University, Department of Physics. 2016.

[82] S.D'Auria."The ATLAS Semiconductor Tracker: Operations and Performance". Tech.Rep.ATL-INDET-PROC-2012-027, CERN, Geneva, 2012. Online: `https://cds.cern.ch/record/1494558`

[83] D.Green. "High p_T Physics at Hadron Colliders". Cambridge University Press. 2005.

[84] F. Pastore. "ATLAS Run-2 status and performance". Tech. Rep. ATL-GEN-PROC-2015-001, CERN, Geneva, Sep, 2015. `https://cds.cern.ch/record/2048973`.

[85] S. M. Shaw and ATLAS Collaboration. "The Run-2 ATLAS Trigger System". Online: `https://cds.cern.ch/record/2127944`

[86] Yu Nakahama. "The ATLAS Trigger System: Ready for Run-2". In: *J. Phys. Conf. Ser.* 664.8 (2015), p. 082037. `doi:10.1088/1742-6596/664/8/082037`.

[87] ATLAS Collaboration. "Search for Top Squark Pair Production in the Final States with One Lepton, Jets and Missing Transverse Momentum Using 36.1 fb^{-1} of $\sqrt{s}$=13TeV pp Collision Data with the ATLAS Detector". Internal Note. ATL-COM-PHYS-2016-1623. Draft version 0.6.

[88] "ATLAS Internal Documentation: Data Preparation Check List for Physical Analysis". Online: `https://twiki.cern.ch/twiki/bin/viewauth/Atlas/DataPreparationCheckListForPhysicsAnalysis`

[89] ATLAS Collaboration. "Search for Top Squark Pair Production in the Final States with One Lepton, Jets and Missing Transverse Momentum Using 36.1 fb^{-1} of $\sqrt{s}$=13TeV pp Collision Data with the ATLAS Detector". ATLAS-CONF-2017-37. Online: `https://cds.cern.ch/record/2266170/files/ATLAS-CONF-2017-037.pdf`

[90] ATLAS Collaboration. "Selection of Jets Produced in 13TeV Proton-Proton Collisions with ATLAS Detector". Tech. Rep. ATLAS-CONF-2015-029. CERN 2015. Online: `https://cds.cern.ch/record/2037702`

[91] C.Anastopoulos et al. "Electron Efficiency Measurements with the ATLAS Detector Using the 2015 LHC Proton-Proton Collision Data". Tech. Rep. ATLAS-COM-CONF-2016-028. CERN. 2016. Online:`https://cds.cern.ch/record/2142831`

[92] ATLAS Collaboration. "Muon Reconstruction Performance of the ATLAS Detector in Proton-Proton Collision Data at $\sqrt{s}$=13 TeV. Eur. Phys. J. C **76**. `arXiv:1603.05598`. CERN-EP-2016-033, (2016) 292. 45 p.

[93] M.H. Seymour. "Monte Carlo Event Generators. Lectures Given at Scottish Universities Summer School in Physics 2012". (SUSSP 69). 2013. `arXiv:1304.6677[hep-ph]`.

[94] D. Schaile. "Advanced Particle Physics". Lecture Notes. 2015. LMU München.

[95] A. Buckley et al. "General-Purpose Event Generators for LHC Physics". CERN-PH-TH-2010-298. 2011. `arXiv:1101.2599v1[hep-ph]`.

[96] S. Alioli, P. Nason, C. Oleari and E. Re. "A General Framework for Implementing NLO Calculations in Shower Monte Carlo Programs: The POWHEG BOX". JHEP **1006** (2010) 043. `arXiv:1002.2581[hep-ph]`.

[97] T. Sjöstrand, S. Mrenna and P. Z. Skands. "PYTHIA 6.4 Physics and Manual". HEP **0605** (2006) 026. `arXiv:hep-ph/0603175`.

[98] M. Czakon, P. Fiedler and A. Mitov. " Total Top-Quark Pair-Production Cross Section at Hadron Colliders Through O(α_s^4)". Phys. Rev. Lett. **110** (2013) 252004. `arXiv:1303.6254[hep-ph]`.

[99] M. Czakon and A. Mitov. "NNLO Corrections to Top Pair Production at Hadron Colliders: The Quark-Gluon Reaction". JHEP **1301** (2013) 080. `arXiv:1210.6832[hep-ph]`.

[100] M. Czakon and A. Mitov. "NNLO Corrections to Top-Pair Production at Hadron Colliders: The All-Fermionic Scattering Channels". JHEP**1212** (2012) 054. `arXiv:1207.0236[hep-ph]`.

[101] P. Bärnreuther, M. Czakon and A. Mitov. "Percent Level Precision Physics at the Tevatron First Genuine NNLO QCD Corrections". Phys. Rev. Lett. **109** (2012) 132001. `arXiv:1204.5201[hep-ph]`.

[102] M. Cacciari, M. Czakon, M. Mangano, A. Mitov and P. Nason. "Top-pair Production at Hadron Colliders with Next-to-Next-to-Leading Logarithmic Soft-Gluon Resummation". Phys. Lett. B **710** (2012) 612. `arXiv:1111.5869[hep-ph]`.

[103] M. Czakon and A. Mitov. "Top++: A Program for the Calculation of the Top-Pair Cross-Section at Hadron Colliders". Comput. Phys. Commun. **185** (2014) 2930. `arXiv:1112.5675[hep-ph]`.

[104] N. Kidonakis. "Next-to-Next-to-Leading-Order Collinear and Soft Gluon Corrections for t-Channel Single Top Quark Production". Phys. Rev. D **83** (2011) 091503. `arXiv:1103.2792[hep-ph]`.

[105] N. Kidonakis. "Two-Loop Soft Anomalous Dimensions for Single Top Quark Associated Production with a W^- or H^-". Phys. Rev. D **82** (2010) 054018. `arXiv:1005.4451[hep-ph]`.

[106] N. Kidonakis. "NNLL Resummation for s-Channel Single Top Quark Production". Phys. Rev. D **81** (2010) 054028. `arXiv:1001.5034[hep-ph]`.

[107] T. Gleisberg, S. Höche, F. Krauss, M. Schönherr, S. Schumann et al. "Event Generation with SHERPA 1.1". JHEP **0902** (2009) 007. `arXiv:0811.4622[hep-ph]`.

[108] S. Catani, L. Cieri, G. Ferrera, D. de Florian and M. Grazzini. "Vector Boson Production at Hadron Colliders: A Fully Exclusive QCD Calculation at NNLO". Phys. Rev. Lett. **103** (2009) 082001. `arXiv:0903.2120[hep-ph]`.

[109] J. Alwall et al. "The Automated Computation of Tree-Level and Next-to-Leading Order Differential Cross Sections and Their Matching to Parton Shower Simulations". JHEP **1407** (2014) 079. `arXiv:1405.0301[hep-ph]`

[110] T. Sjöstrand, S. Mrenna and P. Z. Skands. "A Brief Introduction to PYTHIA 8.1". Comput. Phys. Commun. **178** (2008) 852. `arXiv:0710.3820[hep-ph]`.

[111] C. Borschensky et al. "Squark and Gluino Production Cross Sections in pp Collisions at $\sqrt{s}$= 13, 14, 33 and 100 TeV". Eur. Phys. J.C **74** (2014) 3174. `arXiv:1407.5066[hep-ph]`.

[112] M. Bahr et al. "Herwig++ Physics and Manual". Eur. Phys. J. C **58** (2008) 639. `arXiv:0803.0883[hep-ph]`.

[113] J. Bellm et al. "Herwig 7.0/Herwig++ 3.0 Release Note". Eur. Phys. J. C **76** (2016) 196. arXiv: `1512.01178[hep-ph]`.

[114] S. Schumann, F. Krauss. "A Parton Shower Algorithm Based on Catani-Seymour Dipole Factorisation". JHEP **03** (2008) 038. `arXiv:0709.1027[hep-ph]`.

[115] S. Höche, F. Krauss, M. Schönherr and F. Siegert. "QCD Matrix Elements + Parton Showers: The NLO case". JHEP **04** (2013) 027. `arXiv:1207.5030[hep-ph]`.

[116] R. D. Ball et al. "Parton Distributions with LHC Data". Nucl. Phys. B **867** (2013) 244. `arXiv:1207.1303[hep-ph]`.

[117] S. Frixione, E. Laenen, P. Motylinski, B. R. Webber and C. D. White. "Single-top Hadroproduction in Association with a W Boson". JHEP **0807** (2008) 029. `arXiv: 0805.3067[hep-ph]`.

[118] P. Artoisenet, R. Frederix, O. Mattelaer and R. Rietkerk. "Automatic Spin-Entangled Decays of Heavy Resonances in Monte Carlo Simulations". JHEP **03** (2013) 015. `arXiv:1212.3460[hep-ph]`.

[119] M. Cacciari, G. P. Salam, and G. Soyez. "The Anti-k(t) Jet Clustering Algorithm". JHEP **0804** (2008) 063. `arXiv:0802.1189[hep-ph]`.

[120] A. Schwartzman. "Jet Energy Calibration at the LHC". Int. J. Mod. Phys. **A30** no. 31, (2015) 1546002. `arXiv:1509.05459[hep-ex]`.

[121] ATLAS Collaboration. "Selection of Jets Produced in 13 TeV Proton-Proton Collisions with the ATLAS Detector". ATLAS-CONF-2015-029, 2015. `https://cds.cern.ch/record/2037702`.

[122] ATLAS Collaboration. "Expected Performance of the ATLAS b-tagging Algorithms in Run-2". ATL-PHYS-PUB-2015-022. CERN. 2015. Online: `http://cds.cern.ch/record/2037697`

[123] ATLAS Collaboration. "Reconstruction, Energy Calibration, and Identification of Hadronically Decaying Tau Leptons in the ATLAS Experiment for Run-2 of the LHC". ATL-PHYS-PUB-2015-045, CERN 2015. Online: `https://cds.cern.ch/record/2064383`

[124] ATLAS Collaboration. "Reconstruction, Energy Calibration, and Identification of Hadronically Decaying Tau Leptons in the ATLAS Experiment for Run-2 of the LHC". ATL-PHYS-PUB-2015-045, 2015. Online:`https://atlas.web.cern.ch/Atlas/GROUPS/PHYSICS/PUBNOTES/ATL-PHYS-PUB-2015-045`.

[125] ATLAS Collaboration. "Expected Photon Performance in the ATLAS Experiment". ATL-PHYS-PUB-2011-007. CERN. 2011. Online: `http://cds.cern.ch/record/1345329`

[126] ATLAS Collaboration. "Performance of Missing Transverse Momentum Reconstruction With the ATLAS Detector in the First Proton-Proton Collisions at $\sqrt{s}$=13TeV". ATL-PHYS-PUB-2015-027. 2015. Online: `https://cds.cern.ch/record/2037904`

[127] T. Aaltonen. et al. "Observation of Single Top Quark Production and Measurement of |Vtb| with CDF". Phys.Rev. **D82** (2010) 112005. `arXiv:1004.1181[hep-ex]`.

[128] M. Cacciari, G. P. Salam and G. Soyez. "The Catchment Area of Jets". JHEP **04** (2008) 005. `arXiv:0802.1188[hep-ph]`.

[129] C. G. Lester and D. J. Summers. "Measuring Masses of Semi-Invisibly Decaying Particles Pair Produced at Hadron Colliders". Phys. Lett. B **463** (1999) 99. `arXiv: hep-ph/9906349[hep-ph]` .

[130] M. L. Graesser and J. Shelton. "Hunting Asymmetric Stops". Phys.Rev.Lett. **111** (2013) 121802 `arXiv:1212.4495[hep-ph]`.

[131] Y. Bai et al. "Stop the Top Background of the Stop Search". JHEP **07** (2012) 110, 2891. `arXiv:1203.4813[hep-ph]`.

[132] M. Baak, G.J. Besjes, et.al. "HistFitter Software Framework for Statistical Data Analysis". 2014. `arXiv:1410.1280v1[hep-ex]`

[133] W+jets Feynman diagram. Online:`https://www-d0.fnal.gov/Run2Physics/top/top_public_web_pages/top_feynman_diagrams.html`

[134] R. Schwienhorst et. al. "Top Cross-Sections and Single Top". Int.J.Mod.Phys.Conf.Ser. 31 (2014) 1460277. `arXiv:1403.0513[hep-ex]`.

[135] ATLAS Collaboration. "Jet Energy Measurement and its Systematic Uncertainty in Proton-Proton Collisions at $\sqrt{s}$=7 TeV with the ATLAS Detector". Eur. Phys. J. C **75** (2015) 17. `arXiv:1406.0076[hep-ex]`

[136] ATLAS Collaboration. "Jet Calibration and Systematic Uncertainties for Jets Reconstructed in the ATLAS Detector at $\sqrt{s}$=13 TeV". ATL-PHYS-PUB-2015-015, 2015. Online: `http://cds.cern.ch/record/2037613`.

[137] ATLAS Collaboration. "Performance of Jet Substructure Techniques for Large-R Jets in Proton-Proton Collisions at $\sqrt{s} = 7$ TeV Using the ATLAS Detector". JHEP **1309** (2013) 076. `arXiv:1306.4945[hep-ex]`.

[138] ATLAS Collaboration. "Calibration of b-tagging Using Dileptonic Top Pair Events in a Combinatorial Likelihood Approach with the ATLAS Experiment". ATLAS-CONF-2014-004. 2014. Online: `http://cdsweb.cern.ch/record/1664335`.

[139] ATLAS Collaboration. "Calibration of the Performance of $b-$tagging for c and Light-Flavour Jets in the 2012 ATLAS Data. ATLAS-CONF-2014-046, 2014. Online: `http://cdsweb.cern.ch/record/1741020`.

[140] E. Gross G. Cowan, K. Cranmer and O. Vitells. "Asymptotic Formulae for Likelihood-based Tests of New Physics". Eur. Phys. J. C71:1554, 2011. `arXiv:1007.1727[physics.data-an]`.

[141] R. J. Barlow. "A Guide to the Use of Statistical Methods in the Physical Sciences". WILEY-VCH, 1989.

[142] M. Baaka, G. Besjes, D. Cote, A. Koutsman, J. Lorenz, and D. Short. "HistFitter Software Framework for Statistical Data Analysis". Journal of Physics: Conference Series **664** no. 7, (2015) 072004. Online: `arXiv:1410.1280v1`.

[143] G.Cowan "Statistical Data Analysis". Oxford University Press Inc. New York. 1998.

[144] G.Cowan. "Satistics for Searches at LHC". `arXiv:1307.2487v1[hep-ex]`.

[145] A. L. Read. "Presentation of Search Results: The CL_s Technique". J. Phys. G: Nucl. Part. Phys. **28** (2002) 2693-2704. Online: `http://stacks.iop.org/0954-3899/28/i=10/a=313`.

[146] J. Lorenz. "Search for Strongly Interacting Supersymmetric Particles Decaying to Final States with an Isolated Lepton with the ATLAS Detector at the LHC". PhD thesis, Section 10.4.2. LMU München, 2014.

[147] G.Cowan. "Statistical MEthods for Particle Physics". Royal Holloway, University of London. Lectures in Aachen. February 2014. Lecture 4. Online: `https://www.pp.rhul.ac.uk/~cowan/stat/aachen/cowan_aachen14_4.pdf`.

[148] ROOT Software Framework. Online: `https://root.cern.ch/`.

[149] RooStats::NumberCountingUtils::BinomialExpZ. Online: `https://root.cern.ch/root/html526/RooStats_NumberCountingUtils.html#RooStats_NumberCountingUtils:BinomialExpZ`.